2017-07-01

Determining H_2O Vapor Temperature and Concentration in Particle-Free and Particle-Laden Combustion Flows Using Spectral Line Emission Measurements

John Robert Tobiasson
Brigham Young University

Determining H_2O Vapor Temperature and Concentration in Particle-Free and Particle-Laden Combustion Flows Using Spectral Line Emission Measurements

John Robert Tobiasson

A thesis submitted to the faculty of
Brigham Young University
in partial fulfillment of the requirements for the degree of

Master of Science

Dale R. Tree, Chair
Bradley R. Adams
Brian D. Iverson

Department of Mechanical Engineering

Brigham Young University

ABSTRACT

Determining H_2O Vapor Temperature and Concentration in
Particle-Free and Particle-Laden Combustion Flows
Using Spectral Line Emission Measurements

John Robert Tobiasson
Department of Mechanical Engineering, BYU
Master of Science

There is a growing need for the clean generation of electricity in the world, and increased efficiency is one way to achieve cleaner generation. Increased efficiency may be achieved through an improved understanding of the heat flux of participating media in combustion environments. Real-time in-situ optical measurements of gas temperature and concentrations in combustion environments is needed. Optical methods do not disturb the flow characteristics and are not subject to the temperature limitation of current methods. Simpler, less-costly optical measurements than current methods would increase the ability to apply them in more circumstances. This work explores the ability to simultaneously measure gas temperature and H_2O concentration via integrated spectral intensity ratios in regions where H_2O is the dominant participating gas. This work considered combustion flows with and without fuel and soot particles, and is an extension of work previously performed by Ellis et al. [1].

Five different combustion regimes were used to investigate the robustness of the infrared intensity integral method first presented by Ellis et al. [1]. These included Post-Flame Natural Gas (PFNG), Post-Flame Medium Wood (PFMW), Post-Flame Fine Wood (PFFW), In-Flame Natural Gas (IFNG), and In-Flame Fine Wood (IFFW). Optical spectra were collected for each regime. Methods for processing the spectra to obtain gas temperature, gas concentration, broadband temperature, and broadband emissivity were developed. A one-dimensional spectral intensity model was created to compare measurements and modeled spectra.

It was concluded that excellent agreement (within 2.5%) was achieved between optical and suction pyrometer gas temperatures as long as 1) the optical probe and cold target used were well-aligned 2) the path length was greater than 0.3 m and 3) the intensity from broadband emitters within the path was smaller than the gas intensity. Shorter path lengths between 0.15 – 0.3 m produced reasonable temperatures with 7 % error while path lengths of 0.05 m or less were as much as 15% in error or the signal would not effectively process. Water vapor concentration was less accurate being at best within 20% (relative) of expected values. The accurate determination of concentration requires first an accurate temperature concentration as well low broadband participation. Some optical concentrations were in error as much as 85%. The 1-D model was compared to the measurement and it was found that the model peaks were sharper and shifted 0.167 cm^{-1} compared to the measured data. The reason for the shift can be attributed to the uncertainty of the reference laser frequency used in the FTIR. No conclusion was found for the cause of the sharper peaks in the model. The integrated area of bands used to find temperature and concentration matched well between the modeled and measured spectrum (3%).

Keywords: radiation, spectral, water vapor, temperature, concentration, emission, intensity

ACKNOWLEDGEMENTS

I would first like to acknowledge Air Liquide for funding our work while we collected data.

I would further like to acknowledge several people for their help in this work, without whom I could not have accomplished this task. First of all, my patient wife who has endured many lonely nights while I worked, along with hours of listening to my attempted explanations of my work and struggles; she offered me much support and good advice. Next, Dr. Dale Tree, my graduate committee chair, whose guidance has helped me navigate the many experiences of problem definition, data collection, and communication through writing and group presentations, as well as beginning to make my way through the realm of working in technical engineering. He particularly spent untold hours assisting me in preparing this thesis when he had many other duties to attend to, and his time is greatly appreciated. Dr. Brad Adams was also of great assistance, helping me to develop the one-dimensional radiation model used in this work and understand the complex radiative interactions between gases and solid particles. Through several discussions with him, I was able to practice presenting some of the key concepts in this work, as well as identify parts of the work where my understanding was weak. David Ashworth, my colleague and fellow graduate researcher under the direction of Dr. Tree, made it possible and enjoyable to collect the necessarily large amounts of data for this endeavor and navigate my educational experience at BYU. Nick Hawkins and the student employees of BYU's ME machine shop were indispensable as I modified probes for this work. I am deeply indebted to all of them, and to all others who guided me to them and through this experience.

TABLE OF CONTENTS

LIST OF TABLES

LIST OF FIGURES

NOMENCLATURE

C_{abs}	Absorption cross-section
I	Intensity
L	Path length
s	Position along a path length
T	Temperature
Y	Mole fraction
Δ	Data spacing
ε	Emissivity
κ	Absorption coefficient
$[\,]_{Av}$	Average (arithmetic mean)
$[\,]_{bb}$	Blackbody
$[\,]_{bkg}$	Background
$[\,]_{Broad.}$	Broadband
$[\,]_{ex}$	Exhaust
$[\,]_{g}$	Gas
$[\,]_{H2O}$	Water
$[\,]_{part.}$	Particle
$[\,]_{S.P.}$	Suction Pyrometer
$[\,]_{\lambda}$	Wavelength

1 INTRODUCTION

The worldwide demand for electricity is constantly increasing. Conventional methods of generating electricity require the combustion of fossil fuels, which generates CO_2 and other pollutants. Any increase in the efficiency of the electricity generation process reduces the amount of fuel required, which in turn reduces CO_2 production and emissions. One path for improving efficiency and reducing CO_2 emissions is improving boiler design for oxy-combustion technologies. Understanding the transfer of heat from flames and combustion products to boiler walls is critical for this design process. In particular, the separate contributions from the various gases and particles involved in the combustion process are of interest.

Current methods of determining the radiative heat transfer in combustion flows lack the ability to distinguish the amounts of radiation originating from the various emission sources, such as hot gases and particles. Gases that participate in radiation emit in a specific spectral range. The spectral emission is dependent on gas temperature, pressure, and concentration. Gas temperature is difficult to measure using any current method. Solid particles originating as fuel or forming from the gas phase as soot are primarily broadband radiators. Narrow angle radiometers are currently the instrument of choice for measuring line-of-sight radiation. Narrow angle radiometers provide total heat flux but give no spectrally dependent information and do not provide information on the source of the radiation be it gas or particle phase.

1.1 Objective

The objective of this work is to explore a method for determining the temperature, concentration, and spectral intensity of H_2O in combustion products with and without particles. This work focuses on extending work previously performed by Ellis, et al. [1]. The previous work established a method for determining gas temperature from the spectral emission of water vapor along a line-of-sight and demonstrated that spectral intensity from the gas phase could be obtained and used successfully to calculate a temperature that matched thermocouple measurements. This work explores several methods for extracting or obtaining the spectral water vapor intensity from intensity measurements containing various combinations of particles and background emission.

1.2 Scope

Given the success of using the measured spectral emission of water vapor to determine temperature by Ellis et al. [1], this work seeks to explore ways to improve the measurement of the spectral water vapor both through improved measurement and through algorithms that enable it to be separated from measurements containing overlapping spectral information. As a result, five environments were studied with varying degrees of difficulty related to isolating the H_2O gas phase contribution to intensity. These included intensities measured along a line of sight for: Post-Flame Natural Gas (PFNG), Post-Flame Medium Wood (PFMW), Post-Flame Fine Wood (PFFW), In-Flame Natural Gas (IFNG) and In-Flame Fine Wood (IFFW). In order to extract only the water vapor intensity from measurements containing various combinations of background emission and participating media, the measured data were modeled by one of two simplifications to the radiative transfer equation that enabled an estimate from the measured data.

In order to improve accuracy, an existing water-cooled probe was modified to produce a cold cavity and placed opposite the measurement probe. For each condition, the impact of path length on measurement accuracy was investigated.

Data collection was limited to a four-month period between January and April 2016 with all data analysis to follow due to reactor availability. This limited experimental apparatus primarily to existing equipment and facilities with little time for modification. A one-dimensional model of radiative transfer with specular reflection was developed and utilized but a more sophisticated model such as a discrete ordinates model or Monte Carlo model was beyond the scope of this work. Also, the investigation of measuring and utilizing CO_2 to obtain temperature or using an optical fiber of expanded spectral range was beyond the scope of this work.

2 LITERATURE REVIEW

This chapter provides a review of literature wherein current temperature and water vapor concentration measurement methods used in combustion flows are discussed. Temperature and concentration enable the gas intensity to be determined. First temperature will be discussed followed by concentration.

2.1 Temperature Measurement in Combustion Products

The simplest method of measuring gas temperature is to use a bare-bead thermocouple. This method has been used extensively (see for example [2], [3]). While thermocouples are relatively inexpensive, their accuracy is significantly reduced because of radiative and conductive transfer between the thermocouple and surroundings. Temporal response can also be a factor, as the thermocouple bead must change temperature to match that of the gas flow. In particle-laden flows, deposits on the thermocouples can further complicate measurements.

Suction pyrometers or aspirated thermocouples have been employed to use convection to counteract heat losses and decrease time dependence as in the work of Newman et al. [4] and Z'Graggen et al. [5]. Suction pyrometers can provide more accurate mean temperatures but they require more equipment, are prone to clogging in particle-laden flows, and greatly disturb the combustion flows. Suction pyrometers also produce a spatially averaged temperature because gas from a large surrounding area must be used to produce the convective heat transfer required.

Brohez et al. [6] employed a two-thermocouple method along with a theoretical heat transfer model to obtain an improved temperature measurement using a thermocouple. Krishnan et al. [7] increased convective heat transfer to a thermocouple by spinning a bare-bead thermocouple in a combustion flow. These attempts have seen limited success, as they are more difficult to use with modest improvements in accuracy.

2.2 Optical Temperature Measurements

Numerous optically based methods of measuring temperature have been used which are more similar to this work; the most significant of these will be explored here. These attempts include two-color pyrometry, CARS, tunable diode lasers, and several methods based on the use of Fourier Transform Infrared (FTIR) spectrometers.

2.2.1 Two-color Pyrometry

Two-color pyrometry is a method that involves measuring light intensity at two wavelengths, or colors, and calculating a ratio of the intensities. This ratio is then used with a correlation determined from Planck's curve to determine temperature. In many combustion environments the emission is from soot particles. Zhao et al. [8] used two-color pyrometry to measure temperature in a diesel engine assuming that the gas temperature would be close to that of the soot temperature. More recently, Draper et al [9] used a digital camera to measure particle temperatures in coal combustion flows. These methods are highly attractive as ex-situ measurements, but require solid emission sources such as fuel particles or soot. Further complication arises when one considers that in a typical industrial-scale combustion environment, fuel particle temperature and gas temperature are likely to be different from each other.

2.2.2 Coherent anti-Stokes Raman Spectroscopy (CARS)

Coherent anti-Stokes Raman Spectroscopy is an optical method used to determine gas temperature via lasers that generate a coherent anti-Stokes light beam, which is then analyzed. Three lasers at separate frequencies are used in this technique: a pump laser, a Stokes laser, and a probe laser. These three beams intersect and produce a coherent, anti-stokes beam. Because the resultant light is coherent the magnitude can be larger than intensity from broadband sources and is much easier to measure. This also allows for the use of optical filters to isolate this light from that of other wavelengths. The CARS method provides the ability for high spatial and temporal resolution [10]. Difficulties that arise with this method include a tradeoff between spatial resolution and signal strength, the need for optical access, and signal broadening caused by polarization [10]. Further limitations include expense and expertise.

2.2.3 Tunable Diode Lasers

Tunable diode lasers (TDL) have been used by many researchers to simultaneously measure gas temperature and H_2O concentration [11] [12]. These methods have the benefits of being non-intrusive, yet are capable of taking detailed in-situ measurements. TDLs are lasers that can precisely scan through a band of wavelengths. The technique operates on the principle of gas absorption, as performed by Zhou et al. [12]. For these measurements, the spectral region is first identified where the gas participates strongly, the gas line shape is well modelled, and a given tunable diode laser can operate. The laser is transmitted through the gas with a detector on the opposite side to measure intensity. The laser is then progressively tuned to various frequencies throughout the spectral region of interest, allowing the determination of the gas's line shape for the spectral region. This line shape is governed by the gas species, pressure, temperature, and concentration. A similar set of measurements at a second, nearby spectral region, allows for the

determination of gas temperature. Once the temperature is known, the peak absorption values can be correlated to water vapor concentration [12].

While this method has great potential for being applied to combustion applications [12], great care must be taken in selecting the line pairs to be used for each specific application [12]. This technique also requires expensive, sensitive electronics, and having two surfaces (laser and detector) that must be kept clean to ensure proper operation of the system. This could potentially lead to complications in highly sooting or particle-laden combustion flows.

2.3 FTIR-based Spectral Measurements

Many combustion researchers have focused on using FTIR spectrometers to investigate gas properties in the past several decades, in particular gas temperature and concentration. They share many of the benefits of tunable laser diode methods, with the increased benefit of providing a larger spectrum from a single measurement.

Griffiths et al. performed early absorption measurements of CO [13] and CO_2 [14]. Their work used medium-resolution FTIR spectrometer measurements. Temperatures were determined by using non-linear, least-squares regression fits of peak absorbance values to predicted models of vibration-rotation lines at relatively low temperatures where emission is negligible. A simplified model was used as well, based on how an FTIR using triangular apodization would measure an absorption peak. The assumption of low temperatures of necessity precluded this work from obtaining functional measurements of high-temperature gases.

Solomon et al. [15] performed FTIR spectral analysis where fuel and particle properties were investigated simultaneously using low-resolution emission/transmission FTIR measurements, which were coupled with tomography. Tomography is the practice of taking

measurements of many cross-sections and reconstructing the profile of a flow. Emission and transmission measurements were taken sequentially for each measurement set. The work of Solomon et al. focused on analysis of CO_2, H_2O, ethylene, methane, butane, acetylene, and soot particles, mostly in laminar diffusion flames. Combinations of emission and transmission measurements were used to determine normalized radiance, which corresponded to blackbody radiation. Radiance, or intensity, was normalized based on a definition that had shown to be comparable to Planck blackbody intensity curves. These types of comparisons were used to determine gas temperatures. In order to determine species concentrations, the absorption coefficients were determined from the transmission measurements. The peak heights of absorption coefficients were used to monitor changes in species concentrations.

Similarly to the work performed by Griffiths [14], Bäcktröm et al. [16] performed measurements focusing on the emission of CO_2 to determine temperature. The method used by Bäcktröm et al. focused on comparing the CO_2 emission at 4.3 μm to blackbody emission, as CO_2 gas emission frequently approaches that of a blackbody at this portion of the spectrum. One disadvantage of this technique is that it requires enough emission from CO_2 for the intensity at 4.3 μm to approach a blackbody curve. Additionally, this is only a temperature measurement, and does not provide information regarding gas concentration in that portion of the spectrum.

Perhaps most similarly to the current work outside of the work of Ellis et al. [1], Ren et al. [17] compared measurements taken with an FTIR in a hot gas sample cell containing CO_2, H_2O, and N_2 to gas intensity models using the HITEMP 2010 database. Data collection conditions were meant to mimic a typical combustion environment where H_2O and CO_2 are the principle product gases, but no particles were present. The work of Ren et al. [17] focused on medium- to high-resolution transmission measurements and an inverse model to determine the

gas temperature and concentrations. With the inverse model, differences were minimized between the modeled and transmission measurements in order to determine gas temperature and CO_2 and H_2O concentration [17]. For CO_2 measurements, bands at 2.7 and 4.3 μm were utilized, while for H_2O measurements bands at 1.8 and 2.7 μm were used [17].

Ellis et al. [1] performed work from which the current work stems. The work of Ellis et al. [1] focused on determining combustion gas temperatures in a turbulent, post-flame, particle-free combustion environment using the Burner Flow Reactor (BFR). High-resolution FTIR measurements were taken to provide detailed spectral emission measurements. That information was then integrated over spectral bands where H_2O was the dominant participating gas, which was subsequently used in a correlation based on the work of Pearson et al. [18] with the HITEMP 2010 database to determine gas temperature.

While significant and valuable, past temperature measurements tended to employ techniques that require an absolute intensity measurement. The current work utilizes a ratio of integrated spectral regions that is relatively insensitive to gas concentration or path length. It also only requires collecting data from one direction. Once temperature is obtained, the concentration measurement requires an absolute measurement but is based on an integrated spectral band that does not require a high resolution of the spectral peaks. Although demonstrated with an FTIR, the current approach is technically possible with band pass filters and detectors which have the potential to greatly reduce the cost.

2.4 Current Approach

The current work is similar to that of Ellis et al. [1], in that it employs the work of Pearson et al. [18] in determining gas intensities, together with ratios of integrals of intensity bands where

H_2O is the dominant participating gas, but differs from that of Ellis et al. in several ways. First, a more accurate method of handling radiation from the walls is employed. Background radiation was also reduced physically via a cold cavity target. A method was also developed to measure water vapor concentration based on the magnitude of some integrated intensity bands. In addition, a method to measure gas temperature and water vapor concentration in particle-laden flows is presented.

2.5 H_2O Gas Concentration

Water vapor concentration is not typically measured in combustion gases as it is not a pollutant, is not easily measured, and is not one of the better indicators of the progress of a combustion process. Water vapor is typically a source of noise or contamination for many combustion gas analyzers and is therefore removed from most sampled gases. In addition to the techniques discussed above which include both temperature and gas concentration measurements, there are two other known methods for measuring H_2O concentration.

2.5.1 Extracted Gas Measurements

One of the most common methods for determining H_2O concentration is to estimate it based on equilibrium or complete combustion of fuel carbon. The estimation is made by measuring species containing carbon including CO_2 and CO and then using the hydrogen to carbon ratio estimate the H_2O present. This appears to be the method used by Andersson et al. [19], and is used in this work to provide reference values for some H_2O concentration measurements.

Direct measurement of water vapor concentration can be accomplished by sampling a gas and using spectral absorption analysis with an FTIR. This method has been demonstrated by

several authors, including Speitel [20]. The FTIR analysis of the sample is compared to that of calibration gases of known concentrations. Complications with this method arise when transporting the gas sample to the FTIR for analysis. Gas temperature must be held constant and uniform, and at a temperature that is high enough to prevent any condensation of the water vapor in the tubing that is used to transport the gas from the combustion reactor to the FTIR. This can be very difficult to achieve, and not performing the measurements on the gases while in the reactor means that temperature and other in-situ information is lost, making this method less desirable.

3 BACKGROUND

The work presented in this chapter reviews the previous work of Ellis et. al. [1], after which FTIR theory is discussed. The chapter begins by reviewing the radiative transfer equation and repeating the theory developed by Ellis et al. [1] for measuring gas temperature using radiative emission from typical combustion gas products. The theory used by Ellis et al. [1] to process measurements in the presence of background radiation is then presented. Finally, a brief theoretical review of FTIR spectrometers and how they function is presented.

3.1 The Radiative Transfer Equation and Gas Intensity Contribution

A single radiative participating medium, such as water vapor, produces a radiative intensity as described in the Radiative Transfer Equation (RTE) shown in Equation 3-1.

$$\frac{dI_\lambda}{ds} = \kappa_{\lambda,g} I_{bb,\lambda}(T_g) - \kappa_{\lambda,g} I_\lambda - \sigma_{\lambda,g} I_\lambda + \frac{\sigma_{\lambda,g}}{4\pi} \int_{4\pi} I_\lambda(\hat{s_i})\, \Phi(\hat{s}_i, \hat{s}) d\Omega_i \tag{3-1}$$

Where I_λ is spectral intensity, s is the path length, $\kappa_{\lambda,g}$ the spectral gas absorption coefficient, $I_{bb,\lambda}(T_g)$ is the spectral black body intensity based on Planck's equation at the gas temperature, $\sigma_{\lambda,g}$ is the gas's spectral scattering coefficient, and Φ is the directional scattering phase function. The absorption coefficient $\kappa_{\lambda,g}$ is defined in Equation 3-2.

$$\kappa_{\lambda,g} = C_{abs,\lambda,g} \frac{P_i}{R_u T_g} N_A \tag{3-2}$$

In Equation 3-2, $C_{abs,\lambda,g}$ is the gas's absorption cross-section and was obtained from a database developed by Pearson, et al. [18] which in turn came from the HITEMP 2010 database. The variables P_i, N_A, R_u, and T_g are respectively the gas's partial pressure, Avogadro's number, the universal gas constant, and the gas temperature.

A schematic diagram of a participating media between two walls is shown in Figure 3-1 showing various contributions to the intensity along a line of sight for a participating media as will typically exist in a combustion application. The radiative transfer equation provides the change in intensity while moving along a path, s. The various contributions are illustrated, the first term in the equation is intensity produced by the emission of the media, the second term is the absorption of intensity by the media and the third term is scattering of intensity along the line of sight outward to the surrounding media, and the fourth term is scattering of intensity from all surrounding directions into the path.

The emission reaching the measurement probe depends on the media behavior as well as the boundary condition on both sides of the path. These boundary conditions must be defined in order to provide a solution for intensity at some path length, L. The diagram illustrates that the intensity at the measurement location is dependent not only on the media in the path but media outside the path which can contribute to observed intensity by in-scattering and by reflections off the opposite wall. The walls can contribute to the emission arriving at the probe by emitting energy that is reflected off a wall and by wall emission within the line of sight, and by wall emission scattered into the line of sight. The temperature measurement technique developed by Ellis et al. [1] requires that only the contribution of H_2O along a line of sight be determined in order to obtain temperature and therefore, this quantity $I_{\lambda,g}$ needs to be determined from a

measurement. In the case where walls or additional participating media are also contributing to the measured intensity, the component from the H_2O gas must be identified or extracted from within the total intensity measured. Two specific simplifications to the radiative transfer equation will be developed along with algorithms to extract the gas intensity. These two simplified solutions will be applied to measured conditions to determine their success in producing accurate H_2O temperature and concentration.

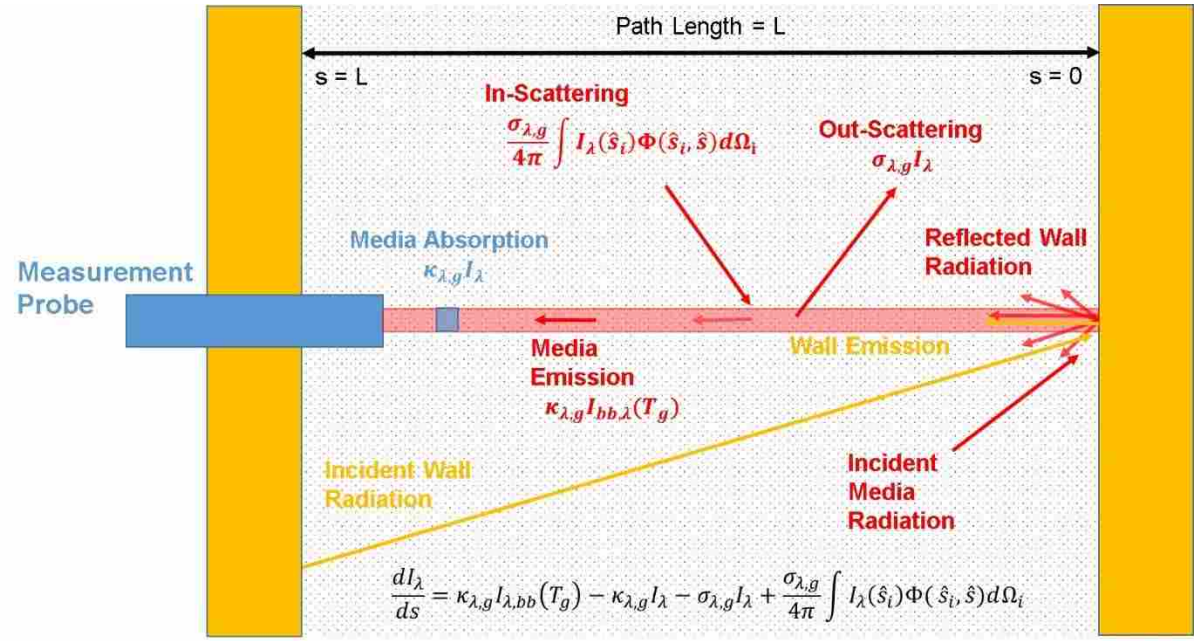

Figure 3-1. A Schematic diagram of contributions to intensity along a line-of-sight for a participating media and surrounding walls.

For both simplifications scattering is assumed negligible. This is common for gas radiation as the participating media [21] but can be problematic for dense particle flows. The RTE simplifies to the result shown in Equation 3-3.

$$\frac{dI_\lambda}{ds} = \kappa_{\lambda,g} I_{bb,\lambda}(T_g) - \kappa_{\lambda,g} I_\lambda \tag{3-3}$$

With the additional assumptions that the gas is uniform in composition and temperature along the path and that both wall boundaries are characterized by a vacuum or a black body at 0 K, the solution shown in Equation 3-4 is the desired spectral gas intensity that is needed for temperature and concentration measurements. In Equation 3-4, $\varepsilon_{\lambda,g}$ is the gas emissivity, which is equivalent to $1 - \exp(-\kappa_{\lambda,g} L)$, a concept which will be used later in this work.

$$I_{\lambda,g} = I_{\lambda,bb}(T_g)\left[1 - exp(-\kappa_{\lambda,g} L)\right] = I_{\lambda,bb}(T_g)\varepsilon_{\lambda,g} \tag{3-4}$$

3.2 Finding Gas Temperature from Spectral Intensity

Ellis, et al. [1], presents a method whereby $\boldsymbol{I_{\lambda,g}}$ can be used to obtain gas temperature by correlating the ratio of integrated modeled [18] spectral bands with temperature and then using the integrated measured spectral band ratio with the correlation to infer temperature. This method is similar to that of two-color pyrometry; however, instead of using Planck's Equation to describe the spectral dependence of the emitting media, in this method a ratio of spectral intensity band integrals as generated by the spectral gas model [18] was found to correlate with temperature. The method is described in more detail below.

First, spectral regions, or bands, were selected where H_2O is a strong emitter-absorber but CO_2 is not. The bands used in this work are shown in Table 3.1, and are located in the near-infrared spectral region. The band widths are on the order of 0.02 - 0.05 μm which is large enough to include approximately 50 – 100 major individual absorption lines.

Table 3-1: Spectral bands where water vapor is the dominate gas.

Band Name	Wavenumber Region (cm^{-1})	Wavelength Region (μm)
A	5185-5310	1.88-1.93
B	5310-5435	1.84-1.88
C	5435-5560	1.80-1.84
D	5560-5615	1.78-1.80
E	5615-5715	1.75-1.78

Second, spectral gas intensity was calculated for the given bands at the resolution of the spectral absorption cross-section database, 0.005 cm^{-1} using Equations 3-2 and 3-4. These were converted to intensity as a function of wavelength and each band of intensity was integrated with respect to wavelength. Ratios were then calculated using these integrated bands, and a plot of integrated spectral band ratio as a function of temperature was created as shown in Figure 3-2. The figure shows three integrated band ratios that are monotonic and changing continuously over the expected temperature range of combustion products. Integrated band ratios involving band D are not shown in Figure 3-2 because they either did not provide monotonic relations between temperature and integrated band ratio or they were found to produce poor temperature predictions when applied to measurements.

A correlation or function was fit to the modeled data that allowed a temperature to be assigned to an integrated band ratio. For each measured band ratio, a temperature can be calculated. If data are taken consistent with the modeling assumptions and without measurement error, all three ratios should produce the same gas temperature.

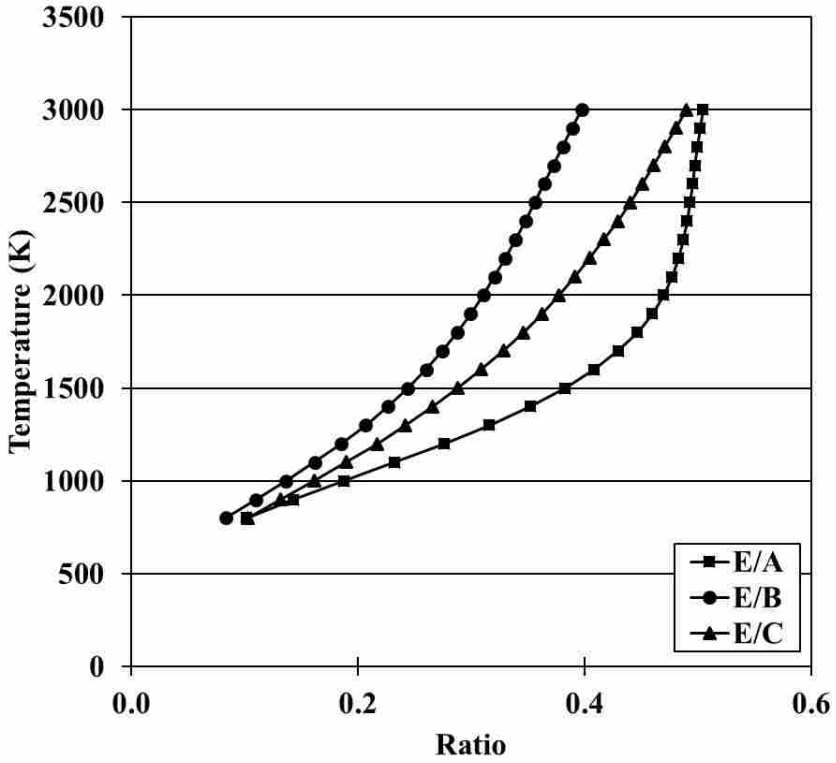

Figure 3-2: Correlations between integrated band ratios and gas temperature. The modeled condition is 10% H_2O in nitrogen over a path length of 0.65m, and a total pressure of 1atm.

Ellis et al. [1] showed that the integrated band ratio was relatively independent of water vapor concentration because both bands experienced a proportional increase in intensity with increasing concentration. A similar argument can also be made for measurement path length.

3.3 Fourier Transform Infrared Spectrometer

In this work, as in the previous work of Ellis et al [1], an FTIR was used to measure the spectral emission of water vapor. An FTIR measures light intensity exiting a Michelson interferometer shown schematically in Figure 3-3. In the FTIR used for this work there are two light sources entering coincidentally: one is the source being measured and the second is a

reference laser beam traveling the same path. The interferometer splits each source into two parts which travel two different path lengths. Approximately half of the emission incident on the beam splitter is directed vertically toward the fixed mirror and is then reflected back through the beam splitter to the detector. The other half of the emission travels through the beam splitter and reflects off the movable mirror and back to the beam splitter and detector. As the mirror moves, the length of the second path changes, producing constructive and destructive interference when the two light beams recombine at the beam splitter and detector.

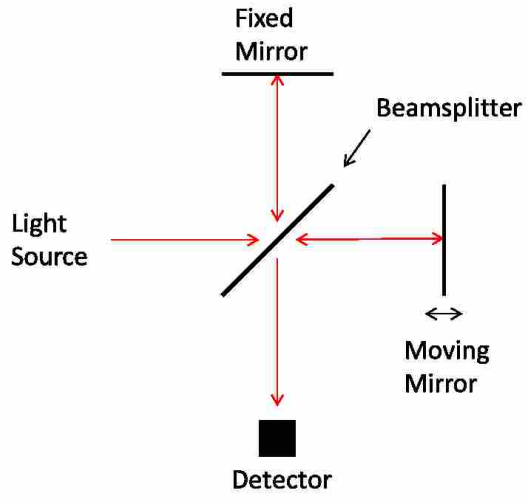

Figure 3-3: Diagram of a Michelson Interferometer used in an FTIR.

An example of a signal that would be obtained from a monochromatic laser is shown in Figure 3-4. For the laser, the intensity is a maximum each time the movable mirror changes the path length by one wavelength of the laser. For example, a 633 nm Helium Neon laser would produce a maximum each time the mirror moved 633 nm. The peak can be used to trigger the FTIR to record a data point, or data can be taken at a fixed frequency and the laser peaks can be

used to determine the distance traveled between recorded data points. The FTIR used in this work shifts the magnitude down so that peaks above and below zero occur and then uses the zero crossing of the monochromatic source to trigger data collection.

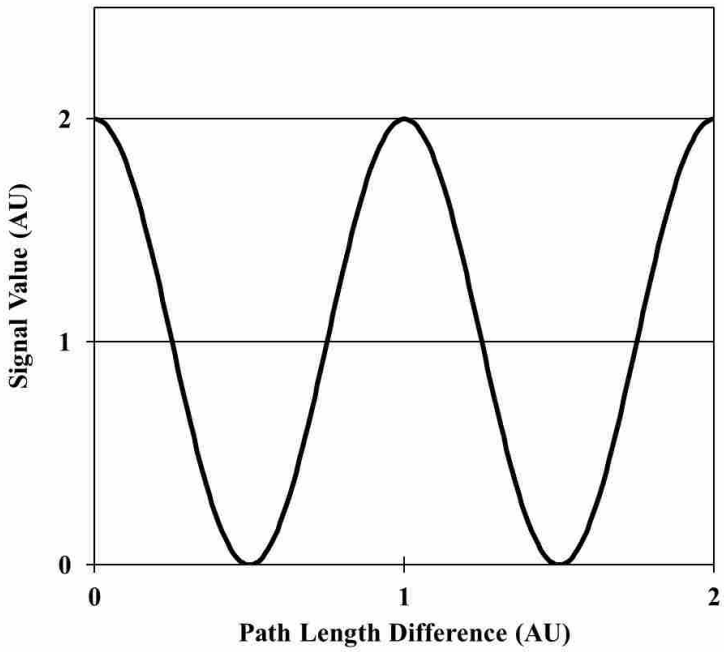

Figure 3-4: Example interferogram for light at one wavelength.

In this work, the source being measured does not consist of a single wavelength and therefore the peaks and valleys of constructive and destructive interference are not easily observed but are nevertheless superimposed on one another in a signal called an interferogram. An example of a portion of an interferogram collected in this work is shown in Figure 3-5. The highest intensity in an interferogram occurs when the movable mirror is in a position to produce an equal path length with the fixed mirror, producing constructive interference at all wavelengths. This is the zero point or center burst. At other positions, the intensity is reduced

due to partly destructive interference. An interferometer's direct measurement consists of all positive values, due to its nature of measuring the brightness of the light as voltages recorded by the detector. It can be seen in Figure 3-5 that the interferogram contains both positive and negative values, as opposed to all positive values, and that the interferogram is relatively flat away from the center burst. In practice, the entire interferogram is shifted equally downward until the average value of the interferogram is zero [22]. This is done because of the Fourier Transform that is applied to the interferogram to obtain a spectrum; Fourier Transforms are sinusoidal by nature, and sinusoids normally oscillate about zero unless they have been shifted vertically [22].

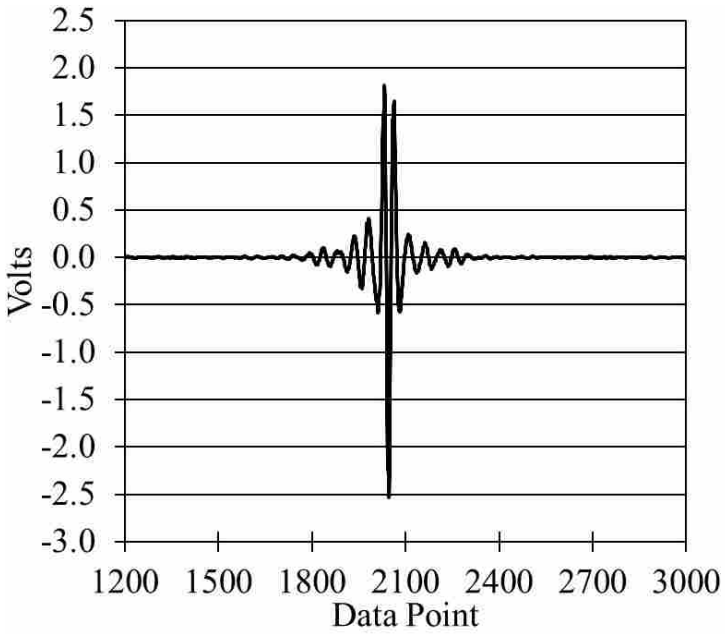

Figure 3-5: Example of an interferogram obtained with an FTIR

Because it is a real, finite instrument, the FTIR can only collect interferogram data over a finite travel of the movable mirror. In this work, the mirror moved a distance of 4 cm, causing an

8 cm maximum difference in the distance traveled for the beam reflecting off of the movable mirror.

Once an interferogram has been collected, an FFT can be performed on the data to produce a frequency spectrum. An example of a portion of such a processed interferogram as collected with the FTIR used in this work is shown in Figure 3-6. As the frequencies involved in producing the interferogram were the frequencies of the source light, when the FFT is performed on the interferogram, the frequencies which it will calculate are those of said light source. The units on the spectral abscissa are cm^{-1}, or wavenumbers. This is because the initial interferogram was collected on the basis of changing path length in units of cm, and the nature of performing an FFT leads to an abscissa with units that are the reciprocal of the original. Because the ordinate has units of Volts, a calibration must be performed on the measurements to convert these spectral values to units of intensity. For this work, the abscissa was converted to units of μm, and the ordinate was converted to $W/m^2/\mu m/sr$ intensity units.

3.3.1 FTIR Resolution

FTIR resolution is not addressed in detail in this section, but the definition of nominal resolution is presented here. Further detail will be presented in Chapter 7 in conjunction with a measured peak broadening discussion. Equation 3-5 [23] shows the definition of nominal resolution as applies to FTIR spectrometry. This definition provides an indication of the FTIR's ability to resolve intensity peaks, being related to the maximum path length difference between the stationary and moving mirrors, presented as ΔL_{max} in the equation.

$$NR = \frac{1}{\Delta L_{max}} \tag{3-5}$$

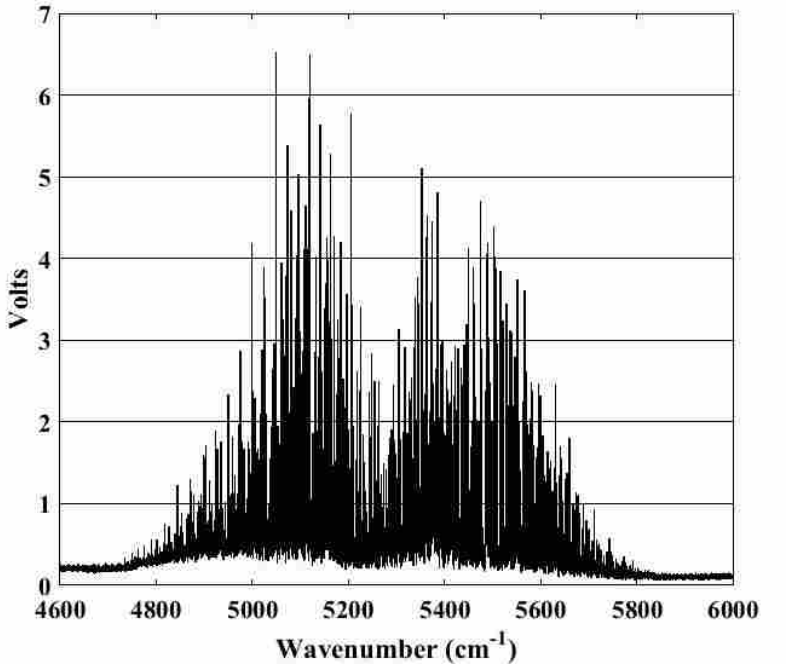

Figure 3-6: Example spectrum calculated by processing an interferogramwhich was measured using an FTIR.

3.3.2 FTIR noise

Signal noise is inherent to the nature of an FTIR spectrometer. Mertz [22] provides a discussion of three kinds of noise encountered in FTIR measurements. They are detector, photon, and modulation noise. That discussion was used as a guide to the discussion presented here.

Electronic detectors themselves exhibit noise for a variety of reasons. For an MCT detector, such as was used in this work, this noise is described by dark current [24]. Dark current is a complex yet well-documented phenomenon wherein random fluctuations of energy in the detector make it appear as though a signal is received, even when no signal-generating photons are present [24]. The amount of noise from dark current is affected in part by the material and fabrication processes [25]. Noise due to dark current is reduced by means of refrigeration, which

reduces these random fluctuations [22] [24]. This noise is largely independent of the signal level [22].

Photon noise arises from the fact that the light being measured travels as photons, which are discrete, quantized amounts of energy, rather than a constant stream. In addition, necessary for photon noise is the ability of an infrared detector to record when even a single photon is incident on the detector [22]. This noise then becomes apparent as different numbers of photons impinge on the detector at different instances in time. This noise should be distributed uniformly over the entire spectrum [22]. Unlike detector noise, photon noise is dependent on the signal level, as by its nature photon noise is related to the amount of light incident on the detector. Photon noise is proportional to the square root of the signal magnitude [22]. If measurements are performed properly, photon noise should be the dominate form of random noise errors [22].

Modulation noise, also known as scintillation noise, is noise that comes from modulation or scintillation of the source itself, and in practice can be drastically reduced if necessary by proper measurement techniques [22]. This noise is directly proportional to the signal magnitude [22]. For a constant source, this modulation can come in the form of fluctuations of participating media between the source and the detector. For instance, in astrological measurements, atmospheric scintillation, arising from atmospheric density fluctuations, can cause scintillation noise, the atmosphere being the participating medium and a star or other celestial body being the source [22]. In the case of this work, participating media that could interfere with the measurement include water vapor that might enter the optical probe cooling tube and cool below the gas temperature, or atmospheric air in the room that might enter the FTIR itself. Any such gases were eliminated from the measurement path by purging the probe and FTIR with argon and nitrogen gases, respectively, as will be discussed in Section 4.1. Thus, no gases were given

the ability to cause modulation after the measurement. Some modulation noise may have been present due to fluctuations of the source, being the hot combustion gases in the Burner Flow Reactor. One might suppose that another source of modulation could be any inconsistency in the velocity of the moving mirror.

A simple method of reducing the random noise encountered when taking FTIR measurements is to collect and average multiple scans. Averaging multiple scans together decreases the noise proportionally to the square root of the number of scans [26].

Aside from these sources of noise, it should be noted that the manufacturer of the FTIR used in this work cites that signal processing electronics can introduce random fluctuations in the signal, or noise, as well [27].

4 EXPERIMENT SETUP

4.1 Reactor and Probe

The experimental setup, shown schematically in Figure 4-1, included an optical probe placed in BYU's Burner Flow Reactor (BFR) to collect data during the combustion of natural gas. The optical probe was water-cooled and collected light via a 12.5 mm calcium fluoride plano-convex lens with a focal length of 20 mm. An optical fiber was placed at the focal length of the lens, such that a collimated beam of infrared light would be directed through the fiber optic cable to the FTIR. The lens is designed to transmit 90% of light between 0.3 and 6.0μm. The fiber optic cable was a pure silica, 400μm diameter, 0.39 NA, SMA-SMA Fiber Patch Cable. The probe was purged with argon to ensure that H_2O would not enter the end of the probe and be cooled, thus interfering with the measurements, as well as to protect the lens from ash deposition. The FTIR was purged with nitrogen to keep the path-length within the device free from H_2O absorption.

The BFR is a 150kW_{th}, down-fired combustion reactor with water-cooled walls. The BFR is a cylindrical shape with an inner diameter of 0.75 m, and is capable of providing swirled air to improve combustion. For the purposes of this work, the BFR was set to its maximum swirl setting and was heated to steady-state conditions for gas temperatures before taking measurements. Data were collected in the post-flame region of the BFR during combustion of 9.3 kg/hr of natural gas with air and a nominal wet exhaust gas O_2 concentration of 3%.

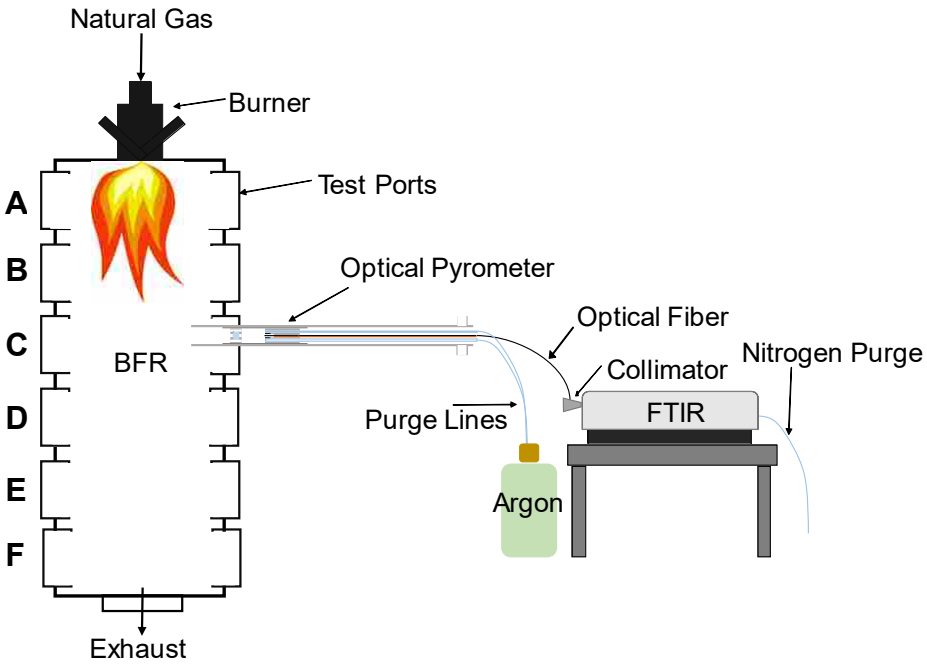

Figure 4-1: Schematic diagram of the Burner Flow Reactor (BFR), optical probe, and FTIR. Figure modified from the work of Ellis et al. [1].

The ports along the sides of the BFR were labeled first by letter, increasing from A at the top to F at the bottom. Each position was further numbered according to the two holes through which measurements were taken. For example, position B1 indicates the top hole of the second-to-top port, and position C2 indicates a hole in the lower half of the third port from the top. The south wall of the reactor was designated the 0 m radial location, and is shown in Figure 4-1 as the side of the BFR where the optical probe was inserted. The north wall of the BFR, opposite to the wall where the optical probe was inserted, was at the 0.75 m radial location.

Suction pyrometer data were taken at the same operating conditions but not at the same time as the optical data. The suction pyrometer data were collected at 5 or 10 cm intervals across the reactor and demonstrated that the temperature profile was uniform across portions of the

reactor, and especially that in the last 10 cm closest to the wall where the temperature dropped due to heat transfer with the colder wall.

Optical data were taken with the optical probe aimed at a water-cooled, cold target in the form of a cold cavity. The optical probe was inserted at the south side of the reactor at varying axial distances from the burner, and the cavity was inserted from the north side of the reactor, always directly opposite to the optical probe. The optical probe and cold cavity were visually aligned for each measurement. The cavity was a hollow cylinder, being 92.5 cm long and 7 cm in diameter. A plate with a 4.5 cm diameter hole was placed on the face of the cold cavity. Due to the fact that the cold cavity was created as a modification of a pre-existing probe, the hole for the cavity was cut with a hand-held cutting torch, which led to a less-than-perfect circle being cut for the opening of the cavity. The cold cavity's theoretical apparent emissivity, ε_a, was calculated based on Equation 4-1, as presented by Modest [21]. In Equation 4-1, ε_m is the emissivity of the material that the cavity is made of, and $\frac{A_0}{A_1}$ is the ratio of the area of the cavity opening to the surface area of the interior of the cavity.

. $$\varepsilon_a = \frac{1}{1 + \left(\frac{1}{\varepsilon_m} - 1\right)\frac{A_0}{A_1}} \tag{4-1}$$

The value of ε_m to be used with Equation 4-1 is not entirely straightforward. The cold target was made of stainless steel, but the inside was coated with layers of ash and soot during combustion measurements. No attempt was made to clean the interior between measurements. Values of ε_m for stainless steel reported by Modest [21] range between 0.13 and 0.42, giving values of ε_a of between 0.95 and 0.99. Ash emissivity varies widely with wavelength and depends heavily on ash particle size and composition [21]. Experimentally, the cold target appeared to exhibit values of ε_a that depended largely on surrounding radiation and how well

the optical probe was focused on the cavity itself. In measurements in the BFR, it is likely that some reflected light from the surface of the plate was within the acceptance angle of the optical probe. That light could have originated from the BFR walls, soot and fuel particles, and the hot gases in other parts of the reactor.

4.2 Probe Calibration

The method of measuring gas temperature and water vapor concentration used in this work requires measurements in terms of absolute spectral intensities. As the FTIR for this work outputs spectra in units of volts, a calibration was necessary to convert the FTIR output to spectral intensity in units of $W/m^2/sr/\mu m$. A schematic of the calibration configuration is shown in Figure 4-2. As shown in the figure, the calibration was performed by directing the optical probe towards the open cavity of a blackbody instrument that was at a known temperature. The probe was then focused and the light path was aligned. To do so, the FTIR's ability to see a near real-time, low-resolution spectrum was used, which allowed for maximizing the signal in various ways. For one, the angles between the probe and blackbody could be adjusted to ensure that the blackbody cavity opening filled the probe's view angle, and was seen straight ahead from the probe. The probe lens and optical fiber could also be repositioned relative to each other to ensure that the cable's opening was placed at the focal point of the lens. Finally, the collimator and its stand were adjusted to maximize the amount of light coming from the optical probe that physically entered the FTIR. The FTIR's ability to make internal adjustments to maximize the signal that it received was also used, in conjunction with the aforementioned methods of aligning and focusing the light path. These adjustments were all iterated on until no further increase in the signal intensity could be observed.

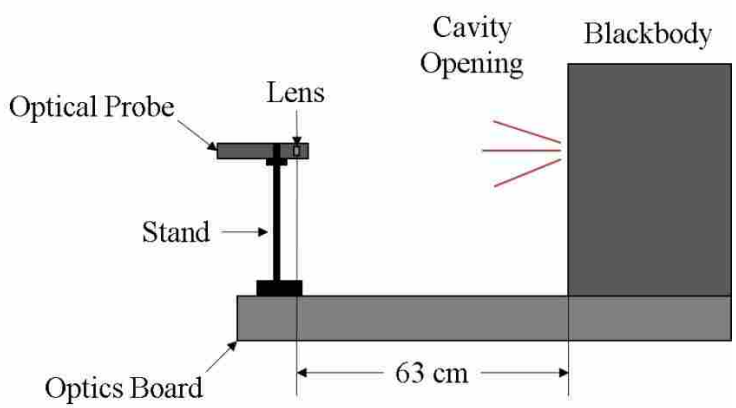

Figure 4-2: Optical probe calibration setup.

Once the focusing and aligning procedures were completed, the calibration itself was performed. In order to use the full applicable range of the blackbody, calibration measurements were taken in front of the blackbody at temperatures from 973.15-1373.15K (700-1100°C) in increments of 50K; here 973.15K is the lowest temperature expected to be encountered based on previous work performed by Ellis, et al [1]. Figure 4-3 shows an example of a raw signal from the FTIR in the spectral region used to obtain water vapor temperature in combustion measurements. Strong absorption lines in the region from approximately 1.8-1.95 μm can be seen which reduce the intensity below the broadband emission of the blackbody. This absorption is the result of cold atmospheric water vapor encountered between the black body and the optical pyrometer.

To remove this unwanted absorption, a spectrum of $C_{abs,H2O}$ was modeled from the work of Pearson, et al. [18] to determine the locations of absorption lines for H_2O at standard atmospheric conditions in Provo, UT on that day. Spectral locations that had absorption cross sections with values higher than a cutoff value of 2×10^{-22} $\frac{\text{cm}^2}{\text{molecule}}$ were selected as strong

participators. The cutoff value of $C_{abs,H2O}$ was selected by starting at a relatively high value and repeatedly lowering it just until a useful portion of the spectrum remained after removing the peaks that were stronger than the cutoff value. If too low of a cutoff value was used, so much of the $C_{abs,H2O}$ spectrum was removed that it was no longer feasible to define a continuous spectrum. If the value were too high, too many of the higher values would remain to consider the strongly participating locations as being eliminated from the measurement.

Next, a visual inspection was made to determine any remaining significant troughs, assumed to be due to carbon dioxide in the air. These relatively few data points where then also removed from each calibration, and linear interpolation was used to fill in between the remaining data points to restore the initial data spacing; linear interpolation was assumed to be sufficient here because the troughs were very narrow. Figure 4-4 shows a comparison of a calibration signal before and after smoothing. The smoothing operation appears to have been relatively successful, but the resolution is too course to provide an accurate assessment. Figure 4-5 depicts a closer view where individual lines can be observed. As can be seen in Figure 4-5, the use of linear interpolation appears to be accurate for the very small spectral separations created by deleting the troughs.

An array of constants, $C_{v,\lambda}$, were obtained for the measured calibration data at each wavelength where data were recorded by the FTIR (every 1/16 of a wavenumber) as shown in Equation 4-2, where $C_{v,\lambda}$, $M_{v,\lambda}$, and $I_{bb,\lambda}$ are the calibration constant, measured intensity, and blackbody intensity values for each measured wavelength.

$$C_{v,\lambda} = \frac{M_{v,\lambda}}{I_{bb,\lambda}(T_{bb})} \tag{4-2}$$

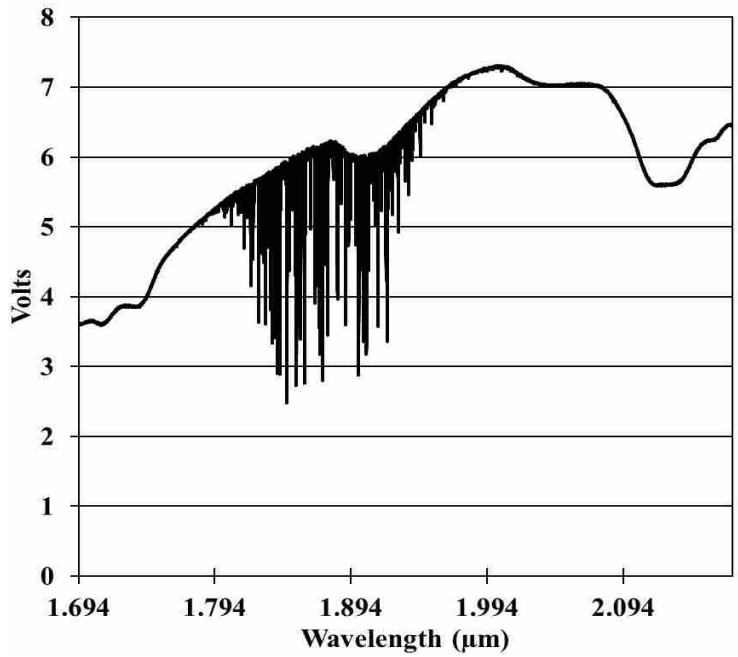

Figure 4-3: Example of an FTIR signal taken during calibration with black body at a temperature of 1273K.

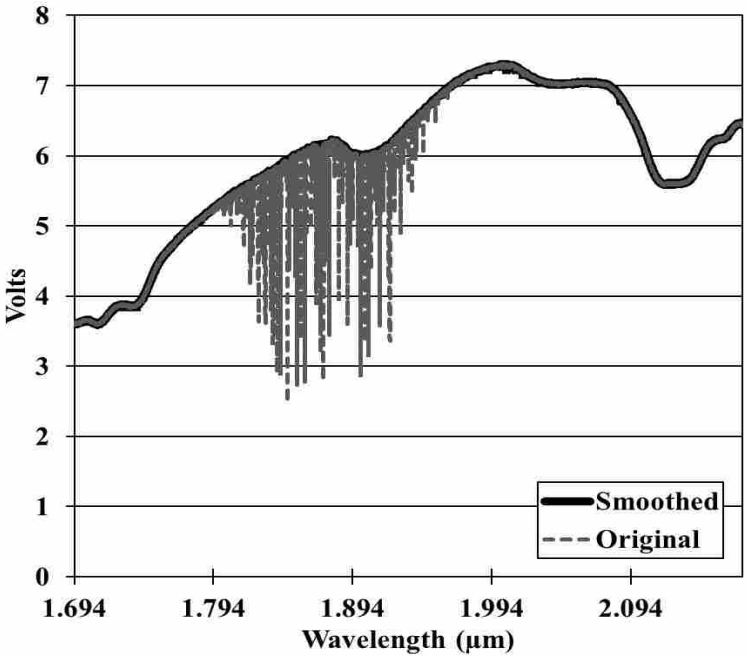

Figure 4-4: Example of a 1273K calibration signal before and after smoothing.

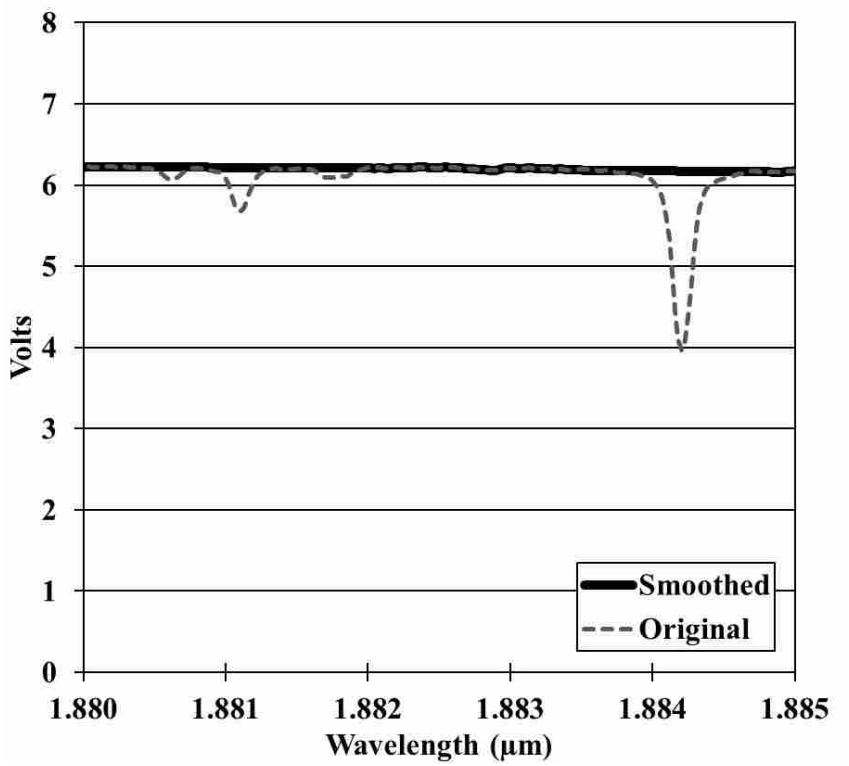

Figure 4-5: Close-up view of calibration measurement shown in Figure 4-4.

Subsequently a curve fit was used at each spectral location to make each $C_{v,\lambda}$ a function of measured voltage at that spectral location, or $C_{v,\lambda} = f(M_{v,\lambda})$. Figure 4-6 shows an example of one such polynomial fit to calibration values. For all values, a third-degree polynomial was fit to the data. The order of the polynomial fit was chosen by fitting representative data sets from each spectral band with polynomial curve fits, as seen in Figure 4-6. Each spectral location that was tested appeared similar in shape to each other, so the uniform value was chosen. As can be seen in the figure, the overall fit was good ($r^2 = 0.9991$) and better at high temperatures which were of greater interest than low temperatures. Once the curve fits of calibration data were generated, they could be used to determine intensity directly from measured voltages as shown in Equation 4-3.

$$I_{v,\lambda} = \frac{M_{v,\lambda}}{C_{v,\lambda}(V)} \tag{4-3}$$

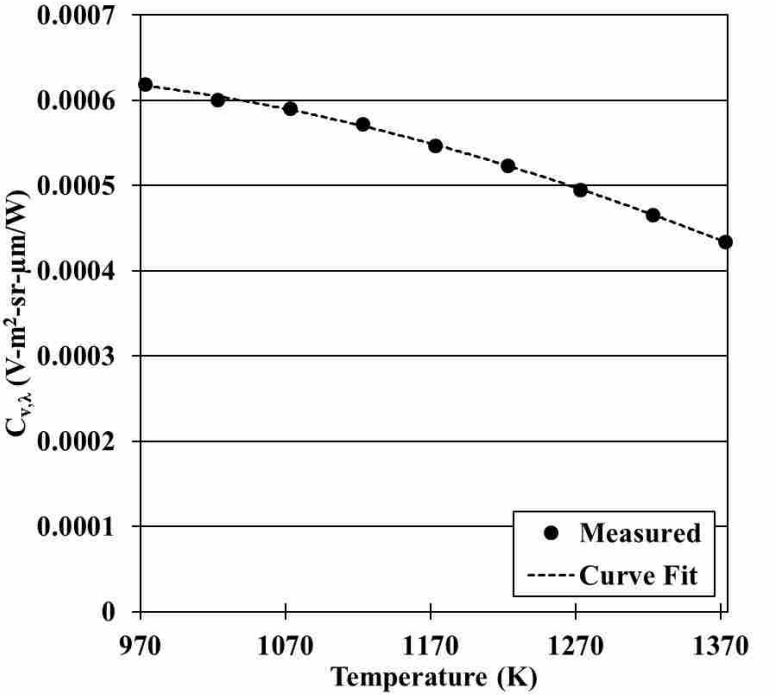

Figure 4-6: $C_{v,\lambda}$ values calculated at 1.866µm for the calibration temperatures.

In order to more fully validate this calibration method, the calibration measurements as volts were processed as in Equation 4-3 and compared to blackbody calculations. In order to investigate the efficacy of this calibration method, the calibration measurements were processed directly from measured values to intensities using the array of calibration functions. This was particularly important for checking the regions where trough data points were removed and replaced with linear interpolation. Figure 4-7 shows the resulting comparison of blackbody intensities and the measured calibration intensities processed using $C_{v,\lambda}$ curve fits. To enhance the readability of the image, only comparisons for 973K and 1373K are shown. In order to

distinguish between the models and the calibrated measurements, only every 700th measured data point was used. As can be seen in Figure 4-7, there is very good agreement between the model and measurement at both bounds of the calibration range, suggesting a functional calibration.

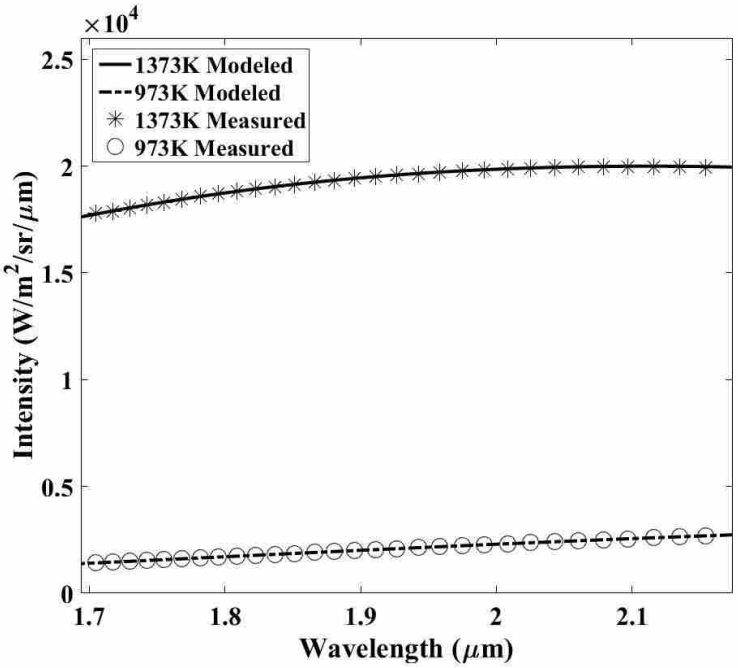

Figure 4-7: Comparison of intensities a) calculated using C_vs and b) modeled blackbody intensities.

4.3 Probe View Angle Determination

Under theoretical conditions, the probe would be perfectly focused and the theoretical view angle would be 0°. This would lead the probe to only see a single column of light the same diameter as that of the lens. The probe was not perfectly focused however, resulting in a view angle that is greater than zero. To calculate the view angle of the probe, the probe was focused and directed at a hot blackbody as was explained in Section 4.2. The distance between the probe and blackbody, or the path length, was varied, and the maximum voltage obtained by the FTIR at

each position was recorded. Figure 4-8 shows the data recorded from these experiments. The path length distance was measured as the distance from the lens to the front of the blackbody, the lens being assumed to be inserted approximately one inch into the probe body. As can be seen in the figure, there is a clear difference in the change in maximum signal with changing path length near a path length of 80 cm. At path lengths shorter than about 80 cm, there is much less change in the maximum signal with an increase in path length; however, at path lengths longer than about 80 cm, there is a sharp decline in the maximum signal. This difference in behavior is believed to be due to the probe's view angle exceeding the area of constant intensity of the blackbody. When the probe was at this point or closer to the blackbody, its entire view was filled by the black body opening, thus the FTIR would only detect the high- temperature blackbody cavity and any change in the maximum signal detected would likely be due to a difference in focus only. At longer path lengths, however, only a portion of the probe's view would be filled by the black body cavity, and that amount would decrease proportionately with increasing distance. As a decreasing portion of the probe's view was filled with the blackbody cavity opening, there would be a proportionate increase in cold surroundings filling the rest of the probe's view. The end result would be an average of the intensity from the cold surroundings and the hot blackbody cavity, leading to a lower maximum signal being reported by the FTIR, which can be seen in Figure 4-8.

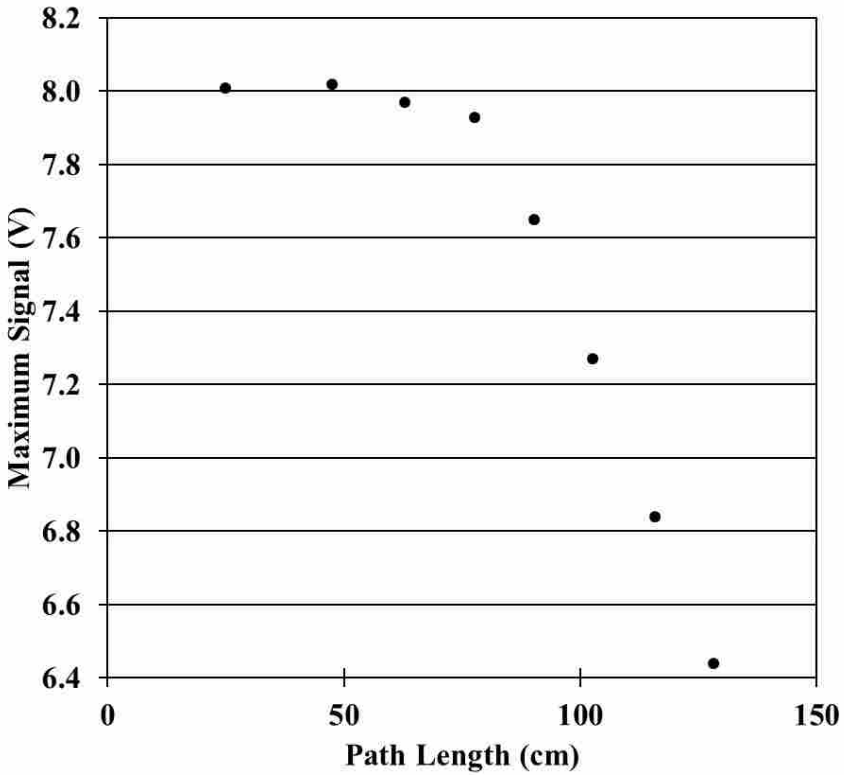

Figure 4-8: Maximum voltage recorded for several distances between a probe and a blackbody at 1100°C.

To find this point of change, and thus enable the determination of the probe's view angle, two polynomials were fit to the data, one for each of the two sections described above. The intersection of these lines was then calculated to be 82.4 cm, and is interpreted as the location where the view area of the probe was equal to the area of the front of the blackbody. The resulting view angle of the probe, based on this point of intersection, was calculated to be 0.61°.

4.4 Experimental Matrix

Data were collected for five different operating conditions on different days under the conditions listed in Table 4.1. All conditions utilized swirled secondary air to produce turbulent mixing of air and fuel. Tested fuels included natural gas (NG), medium wood (MW), and fine

wood (FW). Medium wood refers to woody biomass fuel that was ground to a mean particle size of 500 μm, and fine wood refers to woody biomass fuel that was ground to particle sizes of 224 μm. The last column shows the equivalence ratio calculated from exhaust gas concentration, which fluctuated due to unsteadiness of the fuel flow rate. Each condition has been assigned an acronym based on the location of the measurements and the fuel used. For example, PFNG refers to Condition 1, wherein measurements were taken Post-Flame, or after the visible flame, while burning Natural Gas. IFFW, on the other hand, refers to Condition 5, where measurements were taken In-Flame, or within the visible flame, while burning Fine Wood.

Table 4-1: Data collection conditions

	Condition Name	Relative Position	Reactor Port	Distance from Burner (m)	Fuel	Equiv. Ratio (Exhaust)
Condition 1	PFNG	Post-flame	C2	1.15	Natural Gas	0.83-0.84
Condition 2	PFMW	Post-flame	C2	1.15	Medium Wood	0.82-0.84
Condition 3	PFFW	Post-flame	D2	1.55	Fine Wood	0.75-0.81
Condition 4	IFNG	In-flame	C2	1.15	Natural Gas	0.81-0.87
Condition 5	IFFW	In-flame	B1	0.62	Fine Wood	0.75-0.83

5 THEORETICAL METHODS

In Chapter 3 the method for obtaining temperature from spectral gas intensity, $I_{\lambda,g,}$ along a line of sight was reviewed. This chapter introduces three solutions of the RTE used to extract $I_{\lambda,g}$ from measured intensity. Each of these simplifications involves assumptions that are more or less valid depending on the combustion and measurement conditions. The simplifications and the algorithm used to obtain $I_{\lambda,g}$ will be introduced here with application and result shown in Chapter 6. These methods for determining temperature will be combined with a method for determining H_2O concentration.

5.1 Method 1: Single Media and Hot Gray Wall

The first method for extracting $I_{\lambda,g}$ is presented as an improvement over that used by Ellis et al [1]. It assumes a single participating media, uniform temperature and concentration, negligible scattering, no refection, and gray body wall emission from the opposite wall. The solution to the RTE for this case is shown in Equation 5-1 where $\tau_\lambda = \exp(-\kappa_{\lambda,g}L)$. In the first term on the RHS of Equation 5-1 this represents the attenuation of the wall emission as it propagates through the gas. In the second term on the RHS of the equation it can be used to determine the spectral gas emissivity, $\varepsilon_{\lambda,g} = 1 - \tau_\lambda$.

$$I_{\lambda,meas} = I_{\lambda,bkg}\tau_\lambda + I_{bb,\lambda}(T_g)[1-\tau_\lambda] = I_{\lambda,bkg}\tau_\lambda + I_{\lambda,g} \tag{5-1}$$

$I_{\lambda,bkg}$, being the wall or background emission, is not necessarily small compared to the gas contribution (second term) and the transmittance must be determined in addition to $I_{\lambda,bkg}$ before the first term can be subtracted from the measured intensity to produce $I_{\lambda,g}$. In order to determine the background temperature, two-color band pyrometry is employed. A brief description of two-color pyrometry is presented here, and more details are readily available in the literature (see for example Draper et al. [9].

In two-color pyrometry, the temperature of a solid emitter is determined based on the radiation emitted. Two distinct spectral locations are chosen as in Figure 5-1, represented by dashed lines in the figure. An equation is then created using Planck's curve for a blackbody to give $T_{emitter} = f\left(\frac{I_1}{I_2}\right)$, where I_1 and I_2 are the intensities at those two spectral locations. Because of the unique relationship of the shape of Planck's curve to temperature, where the peak intensity moves to shorter wavelengths as temperature increases, the ratio of $\frac{I_1}{I_2}$ provides a relationship between emitted intensity and the temperature of the emitter. So long as the emitting body is gray between the two spectral locations that are chosen, the emissivity remains unimportant, as it would cancel out of the equation via the ratio of intensities. This method may be used to perform temperature measurements when the appropriate optics are used to collect spectral intensity data for the two chosen spectral locations. This work employs the concept of two-color pyrometry to determine wall temperatures, but instead of using two monochromatic locations as is commonly done, integrals of two spectral bands were used in locations where gas emission was expected to be negligible. These bands were approximately 1.6949-1.7241 μm and 2.1053-2.1739 μm.

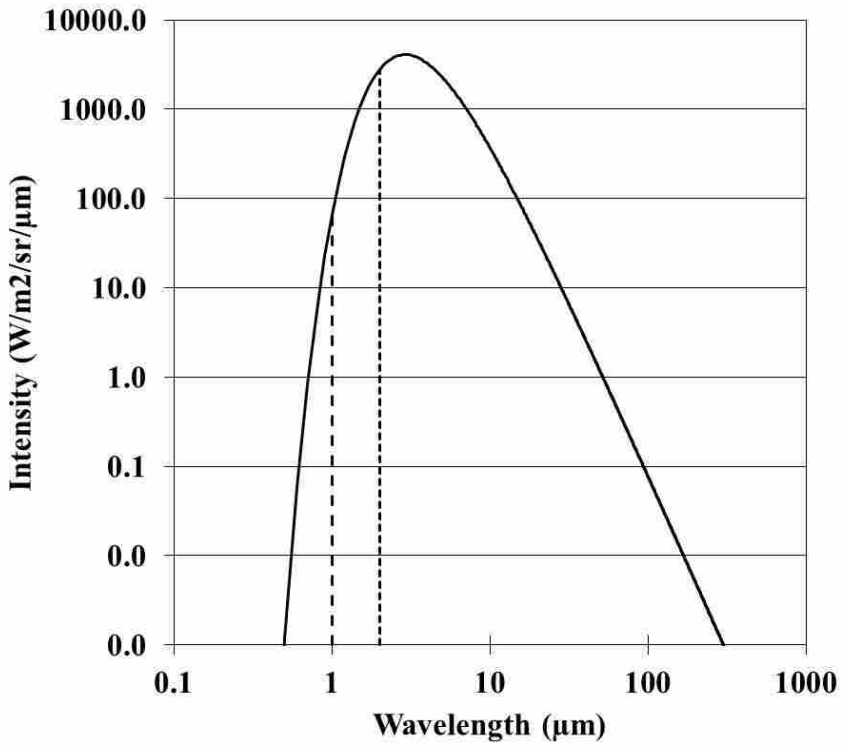

Figure 5-1: Example spectral locations that could be used for two-color pyrometry.

Background intensity is removed and gas temperature and concentration are determined with the following algorithm.

1. Obtain background intensity $I_{\lambda,bkg}$ in spectral regions where $I_{\lambda,g}$ is negligible (1.69 - 1.72µm and 2.11 - 2.17µm).
2. Using Planck's equation and two-color band pyrometry, calculate temperature and emissivity for the background data. This allows for the calculation of $I_{\lambda,bkg}$ in regions where H_2O participates.
3. Guess that τ_λ equals one.
4. Subtract $I_{\lambda,bkg}\tau_\lambda$ from the measured intensity to obtain $I_{\lambda,g}$.

5. Using $I_{\lambda,g}$, find the temperature as outlined in Section 3.2.

6. Solving Equation 5-1 for τ_λ, calculate a new value for τ_λ as shown in (5-2)

$$\tau_{\lambda,new} = 1 - \frac{I_{\lambda,g}}{I_{\lambda,bb}(T_g)} = 1 - \frac{I_{\lambda,meas} - I_{\lambda,bkg}\tau_{\lambda,old}}{I_{\lambda,bb}(T_g)} \tag{5-2}$$

7. Using $I_{\lambda,g}$ find the gas temperature, T_g, as outlined in Section 3.2

8. Iterate through steps 4-7 until T_g does not change. For this work, this was taken to be a percent change of less than 1% between iterations.

9. Guess an H_2O concentration and use Equation 3-2 with the calculated T_g to find $\boldsymbol{\kappa_{\lambda,g}}$. Use Equation 5-1 to obtain the intensity.

10. Integrate this modeled intensity and the measured intensity over bands A-C to obtain a single integrated number for integrated spectral intensity.

11. Compare the integrated values for spectral bands A-C between the model and the measurement. Using linear interpolation/extrapolation, obtain a new concentration.

12. Repeat steps 9-11 until concentration repeats within a fixed tolerance. An absolute percent difference of 0.001 was chosen for this work.

While this was the method used whenever possible for single media measurements, there were cases at very short path lengths were no broadband background emission was detected. These cases produced absolute background temperatures that were negative, which cannot be true. For these measurements, the background removal process was neglected.

5.2 Method 2: Dual Media, No Gray Wall Emission

For a participating media with two components (gas and particles) and negligible scattering, the RTE can be written as shown in Equation 5-3 where $\kappa_{\lambda,g}$ is the absorption coefficient for gas and $\kappa_{\lambda,p}$ is the absorption coefficient for particles. A solution of this equation for a uniform distribution of a two-component medium, or dual media, concentration and temperature and a boundary condition that has gray broadband emission with zero reflection is given by Equation 5-4, where $\kappa_{\lambda,p}$ is the extinction coefficient for the particles. That solution was arrived at using the integrating factor method, with the integrating factor being $\exp\left[\left(\kappa_{\lambda,g}+\kappa_{\lambda,p}\right)s\right]$.

$$\frac{dI_\lambda}{ds} = \kappa_{\lambda,g} I_{bb,\lambda}\left(T_g\right) + \kappa_{\lambda,p} I_{bb,p}\left(T_p\right) - \left(\kappa_{\lambda,g}+\kappa_{\lambda,p}\right) I_\lambda \tag{5-3}$$

$$\begin{aligned} I_{\lambda,meas} = {} & I_{\lambda,bkg}\, exp\left(-\left(\kappa_{\lambda,g}+\kappa_{\lambda,p}\right)L\right) \\ & + \frac{1}{\kappa_{\lambda,g}+\kappa_{\lambda,p}}\left(I_{\lambda,bb}\left(T_g\right)\kappa_{\lambda,g} + I_{\lambda,bb}\left(T_p\right)\kappa_{\lambda,p}\right)\left(1\right. \\ & \left. - exp\left(-\left(\kappa_{\lambda,g}+\kappa_{\lambda,p}\right)L\right)\right) \end{aligned} \tag{5-4}$$

Equation 5-4 shows the difficulty of determining the intensity, $I_{\lambda,g}$, from only the gas phase. With two additional assumptions, the equation can be simplified. The first is that radiation from the wall, $I_{\lambda,bkg}$, is negligible. This is experimentally possible with the presence of a cold cavity. The second assumption is that the total absorption is relatively small. For $\left(\kappa_{\lambda,g}+\kappa_{\lambda,p}\right)L < 0.1$, $1-\exp\left(-\left(\kappa_{\lambda,g}+\kappa_{\lambda,p}\right)L\right) = \left(\kappa_{\lambda,g}+\kappa_{\lambda,p}\right)L$. This approximation allows the separation of the particle and gas absorption coefficients to produce Equation 5-5. The first term on the right hand side is the desired intensity needed to calculate temperature, $I_{\lambda,g}$, and the second

term is the intensity contribution from the particles, $I_{\lambda,p}$. Limitations to this approach are explored in Appendix A.

$$I_{\lambda,meas} = I_{\lambda,bb}(T_g)\left(1 - \exp(-\kappa_{\lambda,g}L)\right) + I_{\lambda,bb}(T_p)\left(1 - \exp(-\kappa_{\lambda,p}L)\right) \quad (5\text{-}5)$$

In spectral regions where gas emissions are negligible, the intensity of the particle contribution can be measured to obtain $I_{\lambda,p}$. Another form of Equation 5-5 is to replace the exponential terms with spectral emissivities as shown in Equation 5-6.

$$I_{\lambda,meas} = I_{\lambda,bb}(T_g)\varepsilon_{\lambda,g} + I_{\lambda,bb}(T_p)\varepsilon_{\lambda,p} \quad (5\text{-}6)$$

The algorithm for determining gas temperature and concentration for the dual media, minor gray wall emission is as follows:

1. Obtain particle broadband in intensity, $I_{\lambda,bb}(T_g)\varepsilon_{\lambda,g}$ from spectral regions where $I_{\lambda,g}$ is negligible (1.69 - 1.72μm and 2.11 - 2.17μm).
2. Using Planck's Equation and two-color band pyrometry as was done for the Single Media and Hot Gray Wall case, calculate an effective temperature and emissivity for the background data. This allows for the calculation of $I_{\lambda,bkg}$ in regions where H_2O participates.
3. Subtract the Planck broadband intensity, $I_{\lambda,bb}(T_g)\varepsilon_{\lambda,g}$, from the measured intensity to obtain $I_{\lambda,g}$.
4. Using $I_{\lambda,g}$, find the temperature as outlined in Section 3.2

Following temperature determination, the less-restrictive solution to the RTE equation presented in Equation 5-7 was used. Assuming the background signal is low because it is a cold cavity, the equation simplifies to the result in Equation 5-7.

$$I_{\lambda,meas} = \frac{1}{\kappa_{\lambda,g} + \kappa_{\lambda,p}} \left(I_{\lambda,bb}(T_g)\kappa_{\lambda,g} + I_{\lambda,bb}(T_p)\kappa_{\lambda,p}\right)\left(1 - \exp\left(-\left(\kappa_{\lambda,g} + \kappa_{\lambda,p}\right)L\right)\right) \tag{5-7}$$

Continuing on with the algorithm:

5. Guess an H_2O concentration and use Equation 3-2 it to find $\boldsymbol{\kappa_{\lambda,g}}$. The gas temperature, particle temperature, and particle emissivity which have already been obtained are used in Equation 5-7 to obtain the intensity.

6. Integrate this modeled intensity and the measured intensity over bands A-C to obtain a single integrated number for each modeled intensity.

7. Compare the integrated values for spectral bands A-C between the model and the measurement. Using linear interpolation/extrapolation, obtain a new concentration.

8. Repeat steps 5-7 until concentration repeats within a fixed tolerance. An absolute percent difference of 0.001 was chosen for this work.

5.3 1-D Numerical Solution to the RTE

In addition to the simplified analytical solutions to the RTE, a numerical solution was produced for the RTE to predict what the spectral intensity would be for each measured set of temperatures, concentration, and emissivity. The numerical model assumes no scattering and one-dimensional intensity but it allows for variable temperature for each cell along the path. The boundary condition is a wall emitting gray body radiation at a specified temperature and emissivity. The wall also reflects incoming intensity from the line-of-sight but not from diffuse

reflection where intensity originates off-axis. The solution is produced by beginning at the detector position, s = 0, and stepping incrementally toward the opposite wall (see Figure 3-1) using Equation 5-8 where *I(s=0)* was modeled as a black, cold wall at 300 K. This was done to model the water-cooled tube in which the sensor was housed. At the cold cavity side, s = L, a reflected intensity is determined according to Equation 5-9, where: $I_\lambda(\mathrm{L}^+)$ is the intensity entering the cold cavity side, ρ_λ is the reflectivity of the cavity, $I_{bb,\lambda}(T_{bkg})$ is the temperature of the cavity, $\epsilon_{\lambda.bkg}$ is the spectral emissivity of the cavity, and $I_\lambda(\mathrm{L}^-)$ is the intensity leaving the cavity side in the direction of the measurement probe (see Figure 3-1). For particle-laden flows this cavity was assumed to be emit negligible radiation and to not reflect in order to correspond to the assumption used in this work that there was no reflection from the wall opposite the probe. The model can however treat this wall as gray.

$$\begin{aligned} \mathrm{I}_\lambda(\mathrm{s}+\Delta\mathrm{s}) &= \mathrm{I}_\lambda(s)\exp\left(-\left(\kappa_{\lambda,\mathrm{g}}+\kappa_{\lambda,\mathrm{p}}\right)\Delta s\right) \\ &+ \frac{1}{\kappa_{\lambda,\mathrm{g}}+\kappa_{\lambda,\mathrm{p}}}\left(\mathrm{I}_{\lambda,\mathrm{bb}}(\mathrm{T_g},s)\kappa_{\lambda,\mathrm{g}}+\mathrm{I}_{\lambda,\mathrm{bb}}(\mathrm{T_p},s)\kappa_{\lambda,\mathrm{p}}\right)\left(1\right. \\ &\left.- \exp\left(-\left(\kappa_{\lambda,\mathrm{g}}+\kappa_{\lambda,\mathrm{p}}\right)\Delta s\right)\right) \end{aligned} \tag{5-8}$$

$$I_\lambda(\mathrm{L}^-) = I_\lambda(\mathrm{L}^+)\rho_\lambda + I_{bb,\lambda}(T_{bkg})\epsilon_{\lambda.bkg} \tag{5-9}$$

The intensity entering the measurement probe is then determined by taking $\boldsymbol{I_\lambda}(\mathrm{L}^-)$ as the initial intensity and taking incremental steps, Δs, back to the probe location according to Equation 5-8. Although capable of spatially independent temperature, the model was only run for this work with uniform temperature and concentration. The intensity was calculated for every discrete wavelength in the measured spectral region to create a spectrum of modeled intensities.

5.4 Theoretical Methods Summary

In summary, there are three methods used to obtain gas temperature and concentration. The three methods are summarized in Table 5-1 identifying each with an abbreviated name and the major assumptions associated with each method.

Table 5-1: Summary of three methods used to determine temperature from measured intensity data.

Method Name	Assumptions	Solution to RTE
Single Media, Gray Wall Emission	Negligible Scattering Single Participating component Uniform Temperature and Concentration Zero reflectivity at both walls Significant Gray Wall Emission	$I_{\lambda,meas} = I_{\lambda,bkg}\tau_\lambda + I_{bb,\lambda}(T_g)(1-\tau_\lambda)$
Dual Media, No Gray Wall Emission	Negligible Scattering Two Participating components Uniform Temperature and Concentration for each component Zero reflectivity at both walls Small but measurable gray wall emission	$I_{\lambda,meas} = I_{\lambda,bb}(T_g)(1 - \exp(-\kappa_{\lambda,g}L)) + I_{\lambda,bb}(T_p)(1 - \exp(-\kappa_{\lambda,p}L))$
1-D numerical Solution	Negligible Scattering Two participating media Spatially varying temperature and concentration for gas and particles 1-D reflected intensity Gray wall emission	$\mathrm{I}_\lambda(s+\Delta s) = \mathrm{I}_\lambda(s)\exp\left(-\left(\kappa_{\lambda,\mathrm{g}}+\kappa_{\lambda,\mathrm{p}}\right)\Delta s\right) + \frac{1}{\kappa_{\lambda,\mathrm{g}}+\kappa_{\lambda,\mathrm{p}}}\left(\mathrm{I}_{\lambda,\mathrm{bb}}(\mathrm{T_g},s)\kappa_{\lambda,\mathrm{g}} + \mathrm{I}_{\lambda,\mathrm{bb}}(\mathrm{T_p},s)\kappa_{\lambda,\mathrm{p}}\right)\left(1 - \exp\left(-\left(\kappa_{\lambda,\mathrm{g}}+\kappa_{\lambda,\mathrm{p}}\right)\Delta s\right)\right)$

5.5 Calculating Reference H_2O Concentrations

Reference water vapor concentrations (Y_{H2O}) were calculated for each optical measurement based on oxygen concentration measurements (Y_{O2}) from the BFR's exhaust. This method is described here.

In order to determine Y_{H2O} from Y_{O2} measurements in the exhaust, a conservation of mass approach was used. Exhaust Y_{O2} measurements were read and recorded once per optical measurement. For the few cases where this was neglected, computer-recorded Y_{O2} data were used to determine the exhaust O_2 concentration for a given measurement based on time stamps of the exhaust data and the optical measurements.

The process used to calculate Y_{H2O} reference values was as follows. Equation 5-10 represents the reaction of fuel with air assuming complete combustion products.

$$\begin{aligned}&(C_xH_yN_zO_vS_w + u\ H_2O_{fuel}) + a(O_2 + 3.76N_2)\\&\rightarrow b\ CO_2 + (c+u)\ H_2O + d\ O_2 + e\ N_2 + f\ SO_2\end{aligned} \tag{5-10}$$

x, y, z, v, w, and *u* were determined from ultimate analyses for the woods used. For natural gas, methane was assumed, where $x = 1$, $y = 4$, and $z = w = v = u = 0$. These six known values were used with an elemental balance and Equation 5-11 to determine the six unknowns (a through f). Equation 5-12 was then used to determine the mole fraction of H_2O.

$$Y_{O2} = \frac{d}{b + c + d + e + f} \tag{5-11}$$

$$Y_{H2O} = \frac{c + u}{b + c + u + d + e + f} \tag{5-12}$$

6 RESULTS AND DISCUSSION

This section contains results for each of the environments from which optical measurements were obtained: Post-Flame Natural Gas (PFNG), Post-Flame Medium Wood (PFMW), Post-Flame Fine Wood (PFFW), In-Flame Natural Gas (IFNG) and In-Flame Fine Wood (IFFW). For each environment, intensities were collected over various path lengths from which four parameters were determined: 1) gas temperature, 2) water vapor concentration, 3) broadband temperature and 4) broadband emissivity. The chapter contains a section for each environment and assesses the ability of the theoretical methods described in Chapter 5 to produce accurate results. Additionally, the measured integrated intensity for each condition is compared with a line-of-sight model based on the four parameters.

6.1 Post-Flame Natural Gas (PFNG)

The PFNG (Post-Flame Natural Gas) measurements represent the simplest type of data, taken in the region after a natural gas flame, and this condition was a valuable beginning point for this work. PFNG conditions provided relatively simple radiation conditions due to the lack of solid fuel and soot particles.

Suction pyrometer temperatures measured at several radial locations across the BFR at an axial distance of 1.15 m from the burner exit are shown in Figure 6-1. The measurement locations were confined to the half of the BFR where the optical probe was inserted, as shown previously in Figure 4-1. All suction pyrometer measurements for this condition were taken at

the same axial location on the same day but immediately after the optical measurements. Several measurements were taken at each location and then averaged to provide the average temperatures as listed in the figure. The variation of an averaged temperature was less than 5 K during the period measured but larger variations may have occurred between the time of suction pyrometer and optical measurements.

The temperature profile is seen to be relatively flat with lower temperatures near the reactor wall and only a slightly lower temperature near the center. This suggests complete combustion and uniform mixing of products with heat transfer producing slightly cooler regions near the reactor wall.

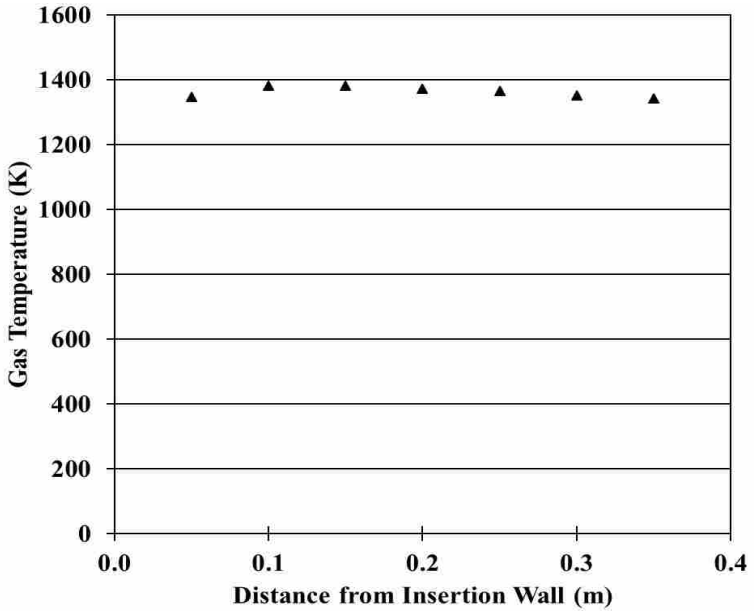

Figure 6-1: Radial gas temperature profile in the BFR for PFNG measurements using a suction pyrometer.

To avoid the cooler regions the optical probe and cold cavity were inserted at least 0.08 m from the BFR wall for all measurements. To calculate temperatures for regions where optical data were taken and suction pyrometer data were not, or those measurements including the half of the BFR opposite to the optical probe insertion point, radial symmetry was assumed in conjunction with uniform mixing.

The results for all PFNG conditions are presented in Table 6-1. The first two columns contain the distance the optical probe (receiving optics) and cold target were inserted from the reactor wall where the optical probe was inserted. The third and fourth columns contain the distance between the optical probe and target, or the path length, and the distance from the probe wall to the center of the optical path. All distances have an uncertainty of $\pm$0.02 m. The spatially averaged temperature of the suction pyrometer measurements for the path length defined in the first four columns is listed in column 5. The calculated optical temperature is given in column 6. An estimated H_2O concentration (reference H_2O, based on exhaust measurements) is given in column 7. The calculated optical H_2O concentration is shown in column 8. Columns 9 and 10 contain the temperature and emissivity calculated from the optical measurement for the broadband radiation. The final column is a measure of the integrated gas intensity divided by the integrated broadband intensity (I_g/I_{bkg}) over the spectral bands A-E.

Although a cold cavity was used, broadband radiation was apparent to some degree in most of the optical measurements. This emission could have been reflected from surrounding walls (most likely) or from an emitting wall within the view of the probe. Therefore, it was important to characterize and remove the influence of broadband emission in the spectral gas intensity. Optical temperature, H_2O concentration and broadband emissivity were calculated according to the method described in Section 5.1 (Single Media, Significant Grey Wall Emission).

For path lengths of 0.08 m and less, the broadband intensity was too low to obtain a temperature or emissivity. At this path length the probe acceptance area must have been completely within the cold target with emissions too low to be seen with the FTIR. I_g/I_{bkg} in the final column of Table 6-1 gives a measure of the integrated gas intensity divided by the integrated broadband intensity. This is used to determine the strength of the water vapor emission relative to broadband radiation. At path lengths at or below 0.08 m, the broadband intensity approaches zero and all measurable emission comes from the water vapor; for these measurements the ratio becomes very large and is not reported.

6.1.1 Optical and Suction Pyrometer Temperature

Figure 6-2 compares selected optical gas temperature measurements with the reference suction pyrometer measurements as a function of path length. The data shown are the first measurement for each path length taken and as they appear in Table 6-1. As can be seen there is excellent agreement (-2.5 % to -0.8 %) between the two temperatures for all path lengths over 0.23 m. Between 0.13 and 0.23 m agreement is generally not as good; on average the optically measured gas temperatures were 5.4% less than the suction pyrometer, the temperature difference at 0.08 cm being an exception.

Assuming the suction pyrometer to be the correct temperature, Figure 6-3 shows the temperature error as a function of path length. With the exception of the data at 0.08 m, the error is increasing with decreasing path length. The data at 0.08 cm and below had too little broadband emission to calculate a broadband intensity and temperature and were therefore processed differently than the rest of the data. The reason for the behavior observed in this figure is discussed in in the following section.

Table 6-1: PFNG data collection positions and results.

Probe Insertion (m)	Target Insertion (m)	Path Length (m)	Measurement Center (m)	$T_{Av., S.P}$ (K)	$T_{optical}$ (K)	$Y_{H2O,exhaust}$	$Y_{H2O,Optical}$	T_{bkg} (K)	ε_{bkg}	I_g/I_{bkg}
0.085	0.665	0.580	0.375	1365.2	1354.5	0.161	0.172	1171.9	0.0417	3.2
0.085	0.665	0.580	0.375	1365.2	1354.1	0.162	0.171	1175.5	0.0407	3.2
0.085	0.565	0.480	0.325	1362.1	1339.5	0.162	0.165	1113.7	0.0325	4.5
0.085	0.565	0.480	0.325	1362.1	1337.9	0.161	0.167	1096.9	0.0354	4.6
0.085	0.465	0.380	0.275	1360.6	1332.4	0.160	0.154	927.1	0.0402	11.0
0.085	0.465	0.380	0.275	1360.6	1338.6	0.162	0.151	898.6	0.0476	12.3
0.135	0.465	0.330	0.300	1357.7	1344.7	0.161	0.135	852.6	0.0559	13.6
0.135	0.465	0.330	0.300	1357.7	1331.1	0.161	0.145	859.3	0.0520	13.9
0.185	0.465	0.280	0.325	1353.8	1319.4	0.161	0.147	819.5	0.0489	19.0
0.185	0.465	0.280	0.325	1353.8	1325.0	0.162	0.151	804.8	0.0600	19.4
0.235	0.465	0.230	0.350	1350.1	1263.7	0.162	0.167	919.0	0.0134	18.1
0.235	0.465	0.230	0.350	1350.1	1307.8	0.162	0.139	824.8	0.0310	20.9
0.285	0.465	0.180	0.375	1346.6	1277.9	0.161	0.146	965.4	0.0046	25.6
0.285	0.465	0.180	0.375	1346.6	1267.2	0.162	0.144	970.4	0.0044	24.1
0.335	0.465	0.130	0.400	1345.0	1269.9	0.162	0.130	966.9	0.0038	19.4
0.335	0.465	0.130	0.400	1345.0	1264.1	0.162	0.145	1352.0	0.0003	26.1
0.385	0.465	0.080	0.425	1346.6	1338.5	0.162	0.112	N/A	N/A	N/A
0.385	0.465	0.080	0.425	1346.6	1355.4	0.162	0.104	N/A	N/A	N/A
0.385	0.465	0.080	0.425	1346.6	1338.2	0.162	0.116	N/A	N/A	N/A
0.435	0.465	0.030	0.450	1351.4	1238.0	0.162	0.100	N/A	N/A	N/A
0.435	0.465	0.030	0.450	1351.4	1216.2	0.160	0.106	N/A	N/A	N/A
0.435	0.465	0.030	0.450	1351.4	1206.7	0.161	0.151	N/A	N/A	N/A

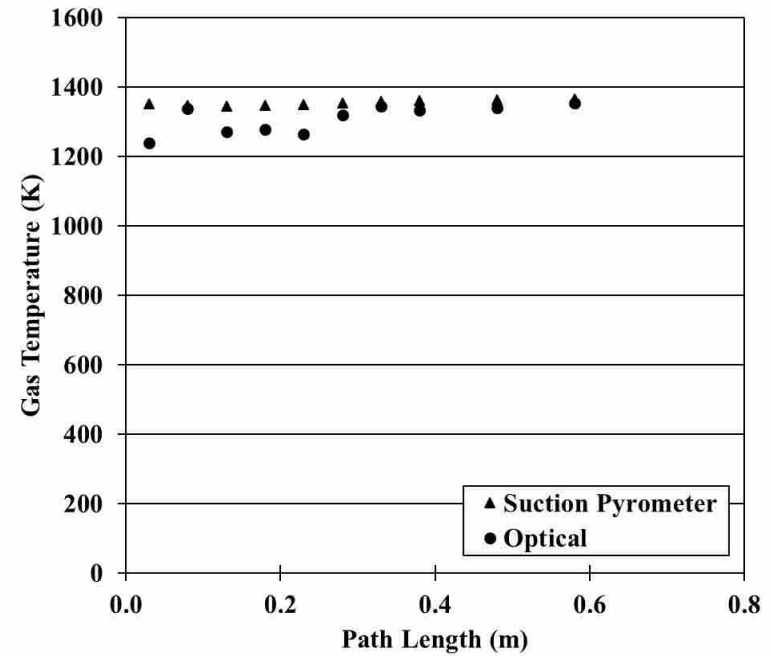

Figure 6-2: Optical and Suction Pyrometer temperatures as a function of path length for PFNG conditions.

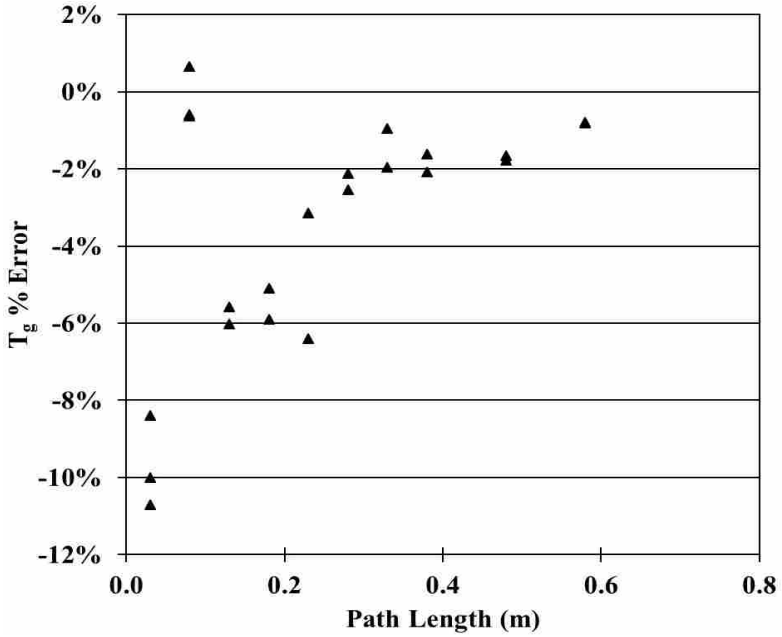

Figure 6-3: Error in optical measurement as a function of path length assuming average suction pyrometer is the correct temperature.

6.1.2 Relative Strengths of Gas and Broadband Intensity

In order to understand the impact of path length on temperature accuracy, a plot of two spectral intensity measurements is shown in Figure 6-4 for path lengths of (a) 0.58 m and (b) 0.08 m. In Figure 6-4 (a) the spectral lines resulting from H_2O emission are readily apparent with some peaks reaching intensities of 12,000 W/m^2/µm/sr. The intensity from broadband radiation (between 1.69 and 1.72 µm and between 2.11 and 2.17 µm) is small but non-zero, on the order of 200 W/m^2/µm/sr. In Figure 6-4 (b), the shorter path length greatly reduced the spectral water intensity with peaks only as high as 300 W/m^2/µm/sr, while the broadband radiation is now averaging close to zero with peak to peak fluctuations of approximately 100 W/m^2/µm/sr. As path length decreases, spectral gas intensity decreases, broadband intensity decreases and peak-to-peak noise remains constant.

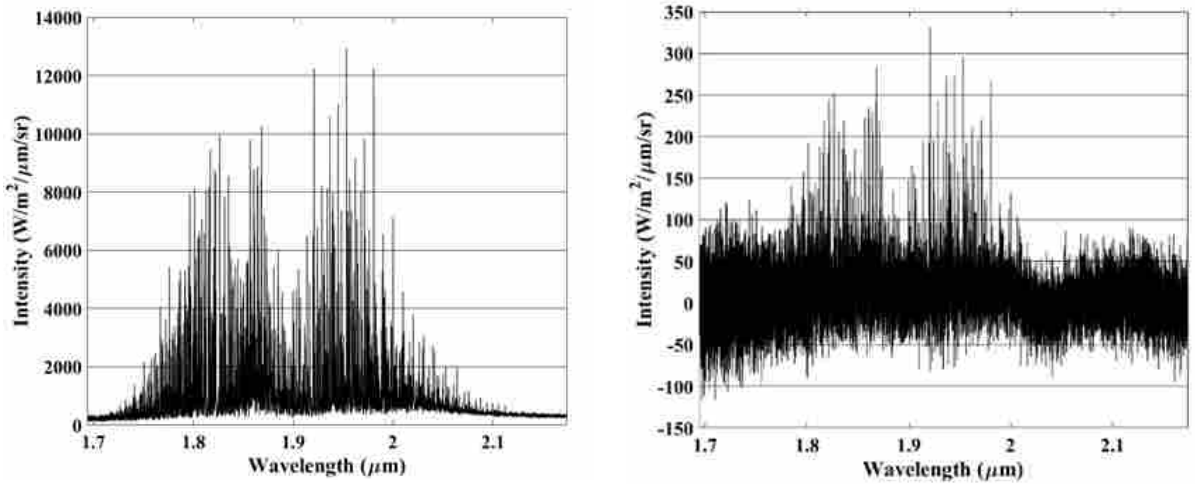

(a) (b)

Figure 6-4: Two spectral intensity measurements for path length of (a) 0.58 m and (b) 0.08 m.

The broadband temperature and emissivity calculated from regions where gas emission is not significant was used to estimate the contribution of broadband emissions in regions A – E where gas emissions are significant. The ratio of integrated spectral gas intensity to integrated broadband intensity over the spectral range A to E is shown in Figure 6-5. The figure shows that as the path length decreases, the ratio of gas intensity to broadband intensity increases and that broadband intensity is a smaller relative source of error at short path lengths than at long path lengths. The error therefore appears to be caused by a decreasing signal that is no longer large enough to distinguish from noise.

The temperature error is consistent with a constant offset in intensity created by FTIR noise in both integrated bands. A constant offset of intensity added to each band would produce a low temperature by decreasing the ratio of integrated intensities. The offset would produce a larger error at low intensities (short path lengths) which matches the data shown.

At the two shortest path lengths, the broadband intensity was so small that the algorithm could not calculate a broadband temperature and emissivity. For these data, it was then assumed that there was no contribution from broadband emission in bands A – E, or in other words, broadband emission was zero in A – E. At 0.08 m this appears to have produced an increase in the temperature which offset the decrease in temperature caused by noise. The match in optical and suction pyrometer temperature at that path length is therefore simply fortuitous.

The level of FTIR noise can be reduced by increasing the number of scans taken in a measurement and by slowing the optical velocity of the moving mirror in the FTIR, as discussed in Section 3.3. However, increasing the number of scans above 16 seemed to have little additional benefit on noise while lengthening the duration of the measurement considerably.

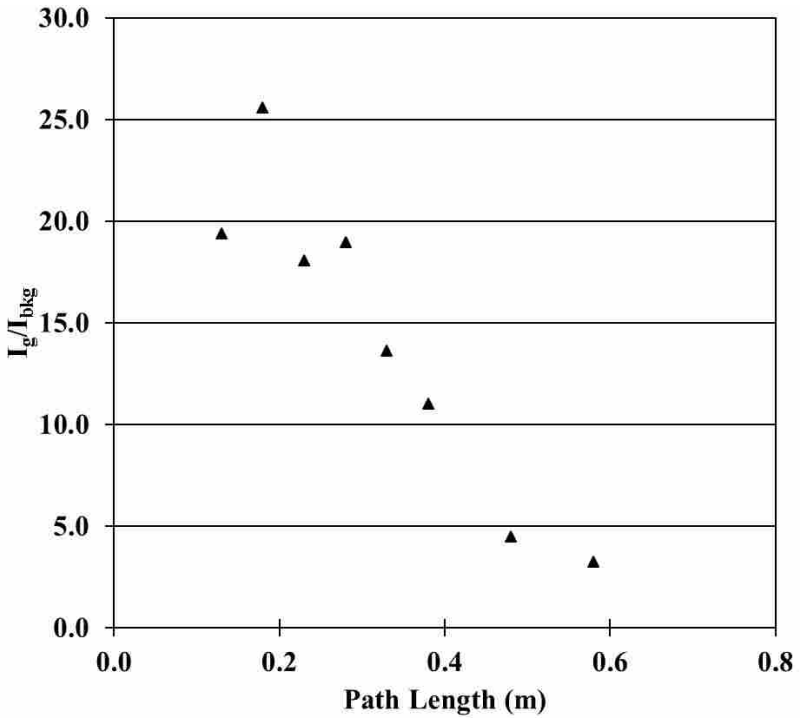

Figure 6-5: Plot of I_g/I_{bkg} versus path length for the selected measurements presented above.

The optical measurement is seen to produce 2% error or less in temperature when the path length is 0.30 m or greater, indicating that the preferred approach is to use longer path lengths, even though they have relatively more broadband radiation from the wall than shorter path lengths. The wall emission can be corrected for in the data processing, at least up to the amounts of broadband emission seen in this work, and there is more gas emission to be used in processing temepratures. The path length required is dependent upon gas temperature and concentration in addition to FTIR noise. Figure 6-6 shows that a path length of 0.30 m corresponded to an integrated intensity of approximately 80 W/m^2/sr for the integrated intensity over bands A-E.

6.1.3 Optical Concentration Measurements

Figure 6-7 shows the percent error for H_2O concentration as a function of path length for all PFNG condition measurements, plotted against path length. The percent error is calculated as the difference between optical measurements and the reference concentrations at the time of the measurement. The reference concentrations are based on exhaust O_2 measurements and an elemental balance as described in Section 5.5, and are believed to be accurate representations of Y_{H2O} for PFNG measurements. Unlike the temperature measurements, concentration measurements do not appear to be improved at longer path lengths. Concentration measurements exhibit a general trend from being slightly higher than expected (up to 6.1% above the reference) at long path lengths to being largely lower than expected (down to -38.1% below the reference) at shorter path lengths. It is believed that this is due to the fact that the concentration measurements are magnitude-based, as opposed to ratio-based. The ratios used in the temperature measurements can effectively cancel out some level of signal error, but with concentration measurements any signal error is represented fully in the measured concentration values. The decreasing signal with decreasing path length is expected to increase the importance of any signal error, due to noise or any other source, making this magnitude-basis for the concentration measurements increasingly inaccurate. The fact that the concentration measurements are dependent on the temperature measurements is also expected to decrease the accuracy of the concentration measurements.

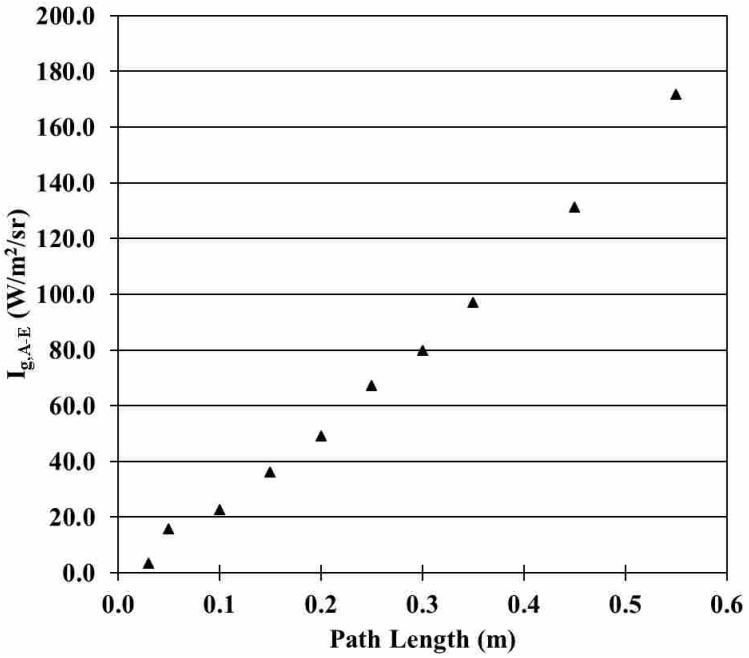

Figure 6-6: Signal, as $I_{g,A-E}$, versus path length

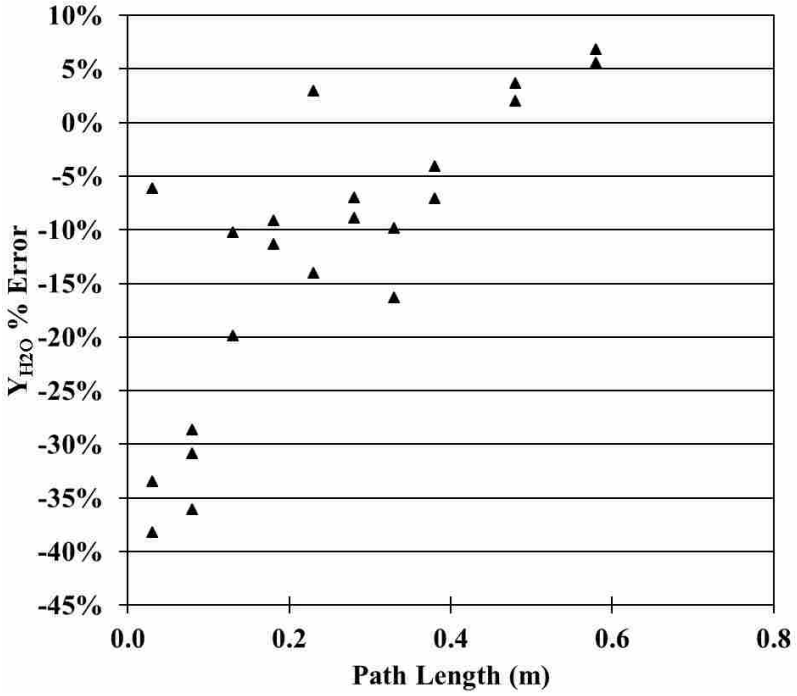

Figure 6-7: Selected Y_{H2O} comparisons for PFNG measurements.

6.1.4 Broadband Intensity and Emissivity

Table 6-1 shows the temperatures and emissivities for broadband intensities measured in regions where gas intensity is negligible. The highest broadband temperatures are approximately equal to the expected wall temperatures, which are typically 100 – 200 K below the gas temperature. The emissivities are all relatively low with the highest being 0.06 and lowest approximately 0.003.

Broadband temperature as a function of path length is shown in Figure 6-8. The temperatures are typically highest at the longest path length. The temperature being lower than the gas temperatures and the low emissivities suggest the broadband radiation is a combination of reflected wall intensity and low temperature emission from the cold cavity probe. The cold cavity opening is 4.5 cm and the view area of the probe at 58 cm based on the view angle measured in Section 4.3 is 2.5 cm at the front and 4.5 cm at the back of the cavity. Assuming perfect alignment the probe will see into the back of the cavity but will likely see some combination of the back surface of the cavity, cavity walls and the plate on the cavity surface. It is therefore concluded that the broadband temperature is a combination of the wall and cavity temperature with the wall temperature being more closely represented at the long path lengths and the cavity temperature, which was not measurable at the short path lengths. A small misalignment of the probe can create a view angle that is in-between these two extremes.

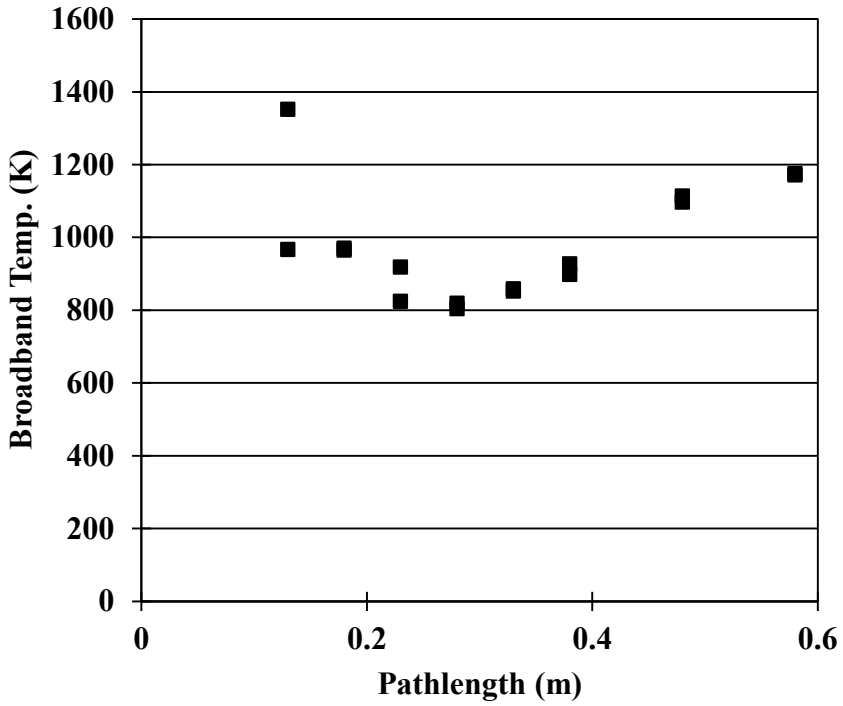

Figure 6-8. Broadband temperature as a function of path length.

6.1.5 Integrated Spectral Intensity

In order to further investigate the efficacy of these optical measurements to measure total intensity, the measured spectral intensity has been compared to a modeled spectral intensity using the optically measured temperature and concentration. The model assumptions are described in Section 5.3. A comparison between the measured and modeled intensity for Test #1 with a path length of 0.58 m is shown in Figure 6-9. The model has been broadened as discussed in Chapter 7. In the figure, it can be seen that the measurement and the model have good visual agreement.

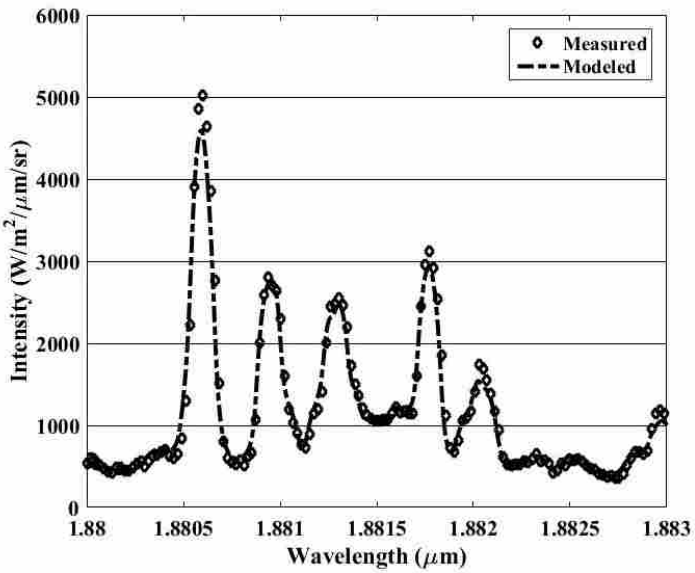

Figure 6-9: Comparison of a typical measurement (Test #1) to a corresponding broadened model, calculated using the optically-measured gas and wall properties.

Table 6-2 shows the percent differences between integrated broadened modeled and measured values of $I_{\lambda,g}$ for bands A, B, C, and E as determined by Equation (6-1. The method used to determine the concentration forces the integrated band intensity of bands A through C of the model and measurement to be equal. The difference between the measured and modeled band integrals then provides information on the consistency that the final temperature and concentration produces over all the bands. It could be expected that the difference in integrated intensity (Equation 6-1) between bands at a given operating condition should be sometimes positive and sometimes negative but on average should be near zero. The results shown in Table 6-2 reflect this, including for band E, which is not included in concentration determination. This suggests that the concentration and temperature determination methods are spectrally consistent. It is important to note that band A is higher in magnitude than bands B, C, and E. This suggests that further work is needed before applying this model to the full spectrum. It is possible that the

background emission is not entirely gray, thus emitting more in some spectral locations than others. This may explain the difference between band A and the rest of the bands.

$$\% \text{ Difference} = \frac{\left(I_{band,meas.} - I_{band,model}\right)}{I_{band,model}} \tag{6-1}$$

Table 6-2: Percent differences between modeled and measured integrated bands.

	Band			
Test #	**A**	**B**	**C**	**E**
1	-2.0%	0.7%	0.4%	-0.4%
2	-1.8%	0.6%	0.3%	-0.4%
3	-2.0%	0.6%	0.5%	-0.3%
4	-2.0%	0.6%	0.5%	-0.3%
5	-2.1%	0.4%	0.6%	-0.2%
6	-2.1%	0.5%	0.6%	-0.2%
7	-2.2%	0.4%	0.7%	0.1%
8	-2.1%	0.4%	0.7%	-0.1%
9	-1.8%	0.3%	0.5%	-0.1%
10	-1.4%	0.1%	0.5%	-0.2%
11	-1.5%	0.0%	0.7%	-0.1%
12	-1.3%	0.1%	0.4%	0.1%
13	-0.2%	-0.5%	0.3%	0.3%
14	0.0%	-0.1%	-0.4%	0.4%
15	-0.6%	-0.1%	0.0%	0.5%
16	0.5%	-0.7%	-0.2%	0.4%
17	3.8%	-2.1%	-0.8%	0.8%
18	4.4%	-1.5%	-2.0%	0.9%
19	3.0%	-1.6%	-0.8%	0.8%
20	7.1%	2.9%	-9.3%	0.3%
21	6.2%	1.4%	-7.0%	0.4%
22	8.1%	-0.9%	-5.6%	0.3%

6.2 Post-Flame Medium Wood (PFMW)

Post-flame medium wood (PFMW) measurements represent another level of radiative complexity not observed in PFNG measurements. For these measurements hot combustion product gases and hot combusting fuel particles were present in the line of sight. PFMW measurements were taken in the same vertical location of the BFR as those of PFNG (1.15 m from the burner).

Suction pyrometer temperature measurements were also taken at the same axial location and were all taken between the second and third optical measurements presented in Table 6-3. Results of suction pyrometer measurements are shown in Figure 6-10. Measurements are referenced from the wall of optical probe insertion up to 0.6 m at 0.1 m intervals. The data match visual observations that the flame was not centered in the reactor but was offset slightly toward the south side of the reactor where the optical probe was inserted. This is typical for solid fuel flames with the current burner. Solid fuel is difficult to distribute uniformly and tends to exit one side of the burner preferentially causing a slight asymmetry. Unlike the natural gas flame, the combustion process is not complete. While volatiles release and combustion may be nearly complete, solid char particles are still present and continue burning at the measurement location. For the purposes of calculating suction pyrometer temperatures along a path length, a linear variation in temperature between points was assumed and the temperature at the far wall (0.75 m) was assumed equal to the temperature at farthest data point (0.60 m). Approximatly three suction pyrometer measurements were taken at each location and then averaged to provide the temperatures as listed in the figure. The temperature varation of the three data points was on the order of 10 K.

Results for all PFMW conditions are presented in tabular format in Table 6-3. The data are presented in the same order as described in Section 6.1, with the exclusion of the column showing I_g/I_{bkg}, and exchanging ε_{BG} for ε_{Part} to indicate that the broadband emission was from particles rather than a background wall. The process used to determine H_2O temperature and concentration and particle temperature and emissivity is method 2 for particles, with no background as described in Section 5.3.

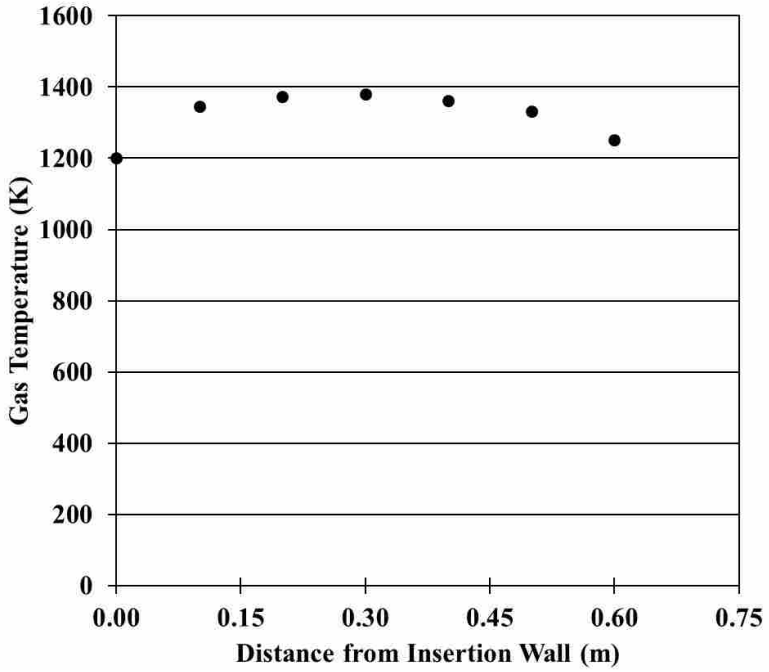

Figure 6-10: Radial gas temperature profile in the BFR for PFMW measurements using a suction pyrometer.

6.2.1 Optical and Suction Pyrometer Temperature

Optical and suction pyrometer temperature data are presented in Figure 6-11 as a function of path length where a single temperature pair was selected for each path length measured. When

more than one data pair were taken for a given path length, the first pair in Table 6-3 was taken. The data show excellent agreement between the suction pyrometer and optical measurement at longer path lengths with increasing differences as path length decreases.

Figure 6-12 shows the error in the optical measurement as a function of path length assuming the suction pyrometer temperatures are correct. Although there was only one measurement obtained for each path length above 0.3, all of the data above this path length are within 1% of the thermocouple data but the scatter in the data appears to increase as the path length decreases. This is consistent with the results for temperature obtained in the PFNG experiments. Although accuracy is decreased with decreasing path length, the optical measurements are typically within 5% at path lengths as short as 0.15 m.

6.2.2 Optical Concentration Measurements

Figure 6-13 shows optically measured and reference H_2O concentrations as a function of the measurement path center. Where more than one path center was encountered, the first one in the data as presented in Table 6-3 was used. The reference concentrations are typically between 10 and 11% H_2O. Optically measured values are both higher and lower than the reference values and all but one are within 4% on an absolute basis or within 46% on a relative basis of the reference values.

Table 6-3: PFMW data collection positions and measurement results.

Test #	Probe Position (m)	Target Position (m)	Path Length (m)	Meas. Center (m)	$T_{Avg, S.P.}$ (K)	$T_{Optical}$ (K)	$Y_{H2O,Opt.}$	$Y_{H2O,Exh.}$	$T_{Part.}$ (K)	$\varepsilon_{Part.}$
1	0.10	0.60	0.50	0.35	1344.8	1357.9	0.129	0.105	1343.8	0.029
2	0.20	0.60	0.40	0.40	1342.9	1346.8	0.129	0.105	1418.1	0.019
3	0.10	0.45	0.35	0.28	1364.8	1371.2	0.114	0.103	1313.8	0.016
4	0.20	0.45	0.25	0.33	1368.6	1331.2	0.119	0.103	1372.8	0.011
5	0.20	0.45	0.25	0.33	1368.6	1336.2	0.118	0.104	1166.3	0.014
6	0.30	0.45	0.15	0.38	1365.0	1290.8	0.101	0.105	1427.1	0.006
7	0.30	0.55	0.25	0.43	1347.1	1336.7	0.099	0.105	1351.7	0.008
8	0.40	0.55	0.15	0.48	1333.0	1319.1	0.111	0.105	925.2	0.021
9	0.40	0.55	0.15	0.48	1333.0	1309.4	0.117	0.103	1425.1	0.006
10	0.40	0.65	0.25	0.53	1306.0	1310.2	0.119	0.103	1479.3	0.014
11	0.50	0.65	0.15	0.58	1281.7	1300.4	0.151	0.103	978.4	0.018

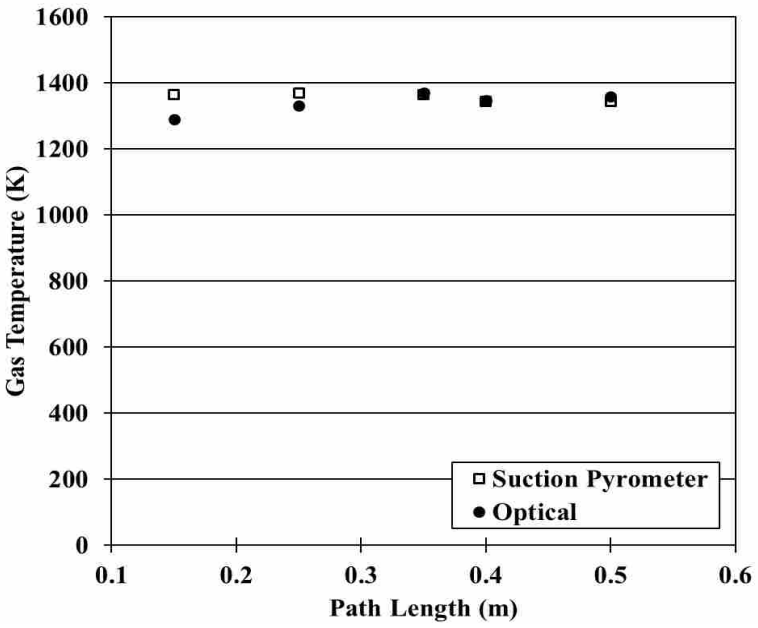

Figure 6-11: Comparison between several PFMW optically measured temperatures and suction pyrometer measurements, plotted by path length.

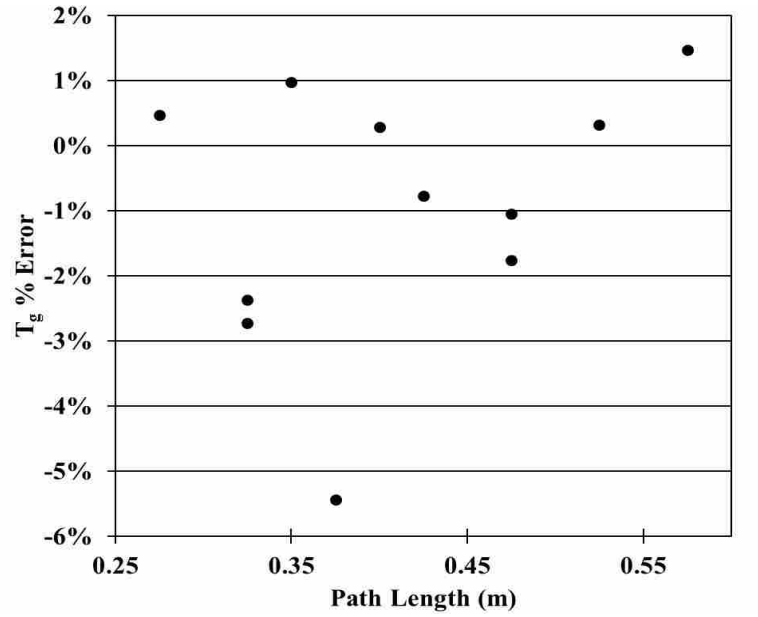

Figure 6-12: Comparison between several PFMW optically measured temperatures and suction pyrometer measurements, plotted by the measurements' center position.

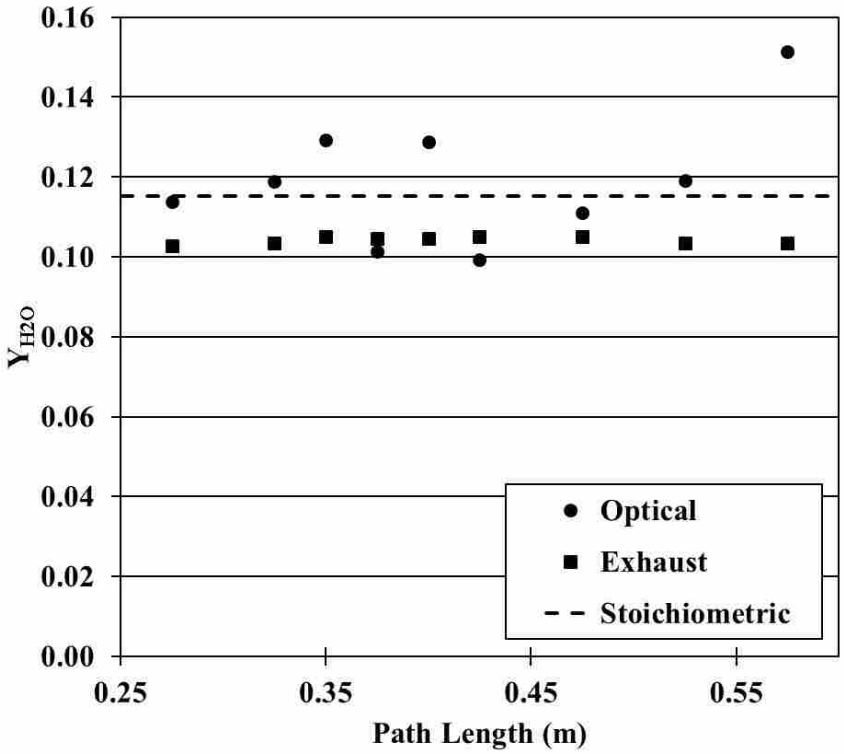

Figure 6-13: Several optical measurements of Y_{H2O} at various path lengths across the BFR, plotted with reference values based on exhaust O_2 measurements and the maximum, stoichiometric Y_{H2O}.

Also included in the figure is the stoichiometric value of Y_{H2O}, which by necessity serves as a maximum value of Y_{H2O}. At leaner conditions, the excess oxygen dilutes the mixture, causing a smaller value of Y_{H2O}. Under more fuel rich conditions, the higher levels of CO, H_2, and OH will dilute the H_2O concentration. When some carbon is still in the fuel particles, before it has burned out, the mixture will act like a lean mixture and the excess oxygen will again reduce the values of Y_{H2O}. Because the stoichiometric Y_{H2O} is a maximum, any values measured that are higher than this value are of particular concern, being higher than they possibly could be. The inaccuracy of the temperature measurement and the signal itself are thought to contribute to the inaccuracy seen here, as was discussed in Section 6.1.3. It is also possible that there was

some reflection, or back scattering, of gas intensity caused by the fuel particles, increasing the magnitude of the measured gas participation.

Adding to the inaccuracy seen in PFMW Y_{H2O} measurements are the complexity of the radiation when both gases and particles are involved, and any inaccuracy introduced by the assumptions used in processing this data: constant, uniform gas and particle distribution and properties. This inaccuracy may also indicate that CO_2 participation can be more important than previously expected in this spectral region. The presence of CO_2 would increase the total emitted intensity. Neglecting the presence of CO_2 and attempting to explain the full radiation with water vapor emission would lead to a higher apparent concentration of H_2O.

6.2.3 Broadband Intensity and Emissivity

The optical probe collects broadband emission as well as the spectral gas emission. For PFMW measurements, this broadband emission is a mixture of background reflection off of the face of the cold target and particle emission. The method for processing the data assumes particle emission is dominant over background emission.

The data in Table 6-3 show 9 of the 11 data points have broadband emissivities of 0.02 or lower and 6 of 11 have broadband temperatures above the optical H2O temperature. This suggests that the broadband radiation is dominated by particles and that the particles are at temperatures similar to the gas temperature. This is in contrast to PFNG results where the broadband temperatures were primarily below gas temperatures. These data suggest that the algorithm used to produce gas temperature that assumed particles in the path with no background radiation is appropriate for this data set.

There are two broadband temperatures (Tests 8 and 11) in PFMW data that are considerably lower than the gas temperatures (952 and 978 K). They also have similar emissivities to those of PFNG background measurements. Both of these low temperatures were obtained at the shortest path length of 0.15 m. It is likely that for these measurements during the measurement period there were very few particles in the path leading to a lower temperature. There does not appear to be any correlation between these measurements with lower calculated broadband temperatures and differences in accuracy for gas temperature and water concentration.

6.2.4 Integrated Spectral Intensity

In the interest of investigating the efficacy of these measurements related to total radiative heat transfer, a comparison is presented between a measurement and broadened modeled intensity data. The broadening method is presented and discussed in Chapter 7.4. A portion of the spectrum for the first PFMW measurement (Test #1) presented in Table 6-3 is used for this comparison, which is presented in Figure 6-14 as the measured data. The model was produced as described in Section 5.3. Each peak in the model has a corresponding peak in the measured data and the peaks have similar magnitudes and shapes.

In order to more closely examine how well the measurement and the model correspond to each other, the percent differences between measured and modeled spectral intensity band integrals are presented in Table 6-4 for all PFMW measurements. It can be seen that integrated areas for measured bands A and B are typically lower than the modeled integrated area and the measured bands C and E are typically higher than the modeled area. Although differences are small, they indicate that the measured and modeled areas in bands further from the A-C might

not be in as good agreement. Additional work is needed to assess agreement of the measurement and modeled areas over the entire spectrum.

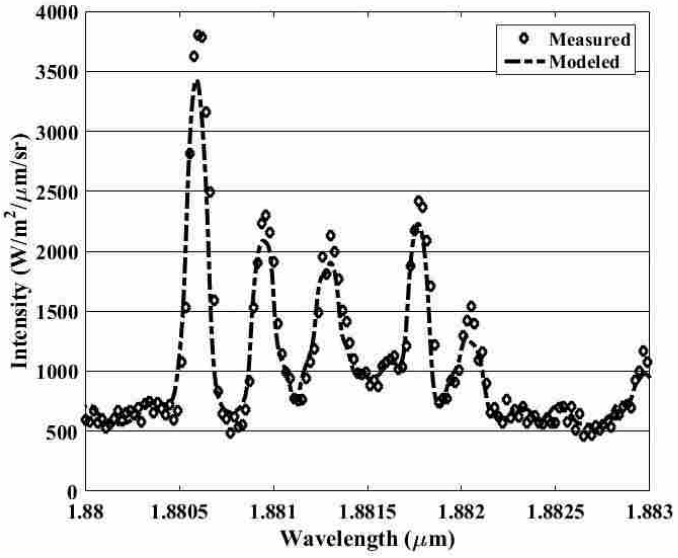

Figure 6-14: Comparison of a portion of the measured and modeled spectrum for Test #1, PFMW.

Table 6-4: Percent differences between modeled and measured integrated bands.

	Band			
Test #	A	B	C	E
1	-1.3%	-0.2%	1.2%	1.0%
2	-1.8%	0.1%	1.2%	1.2%
3	-2.5%	0.5%	1.3%	1.2%
4	-2.4%	0.3%	1.4%	1.1%
5	-2.7%	0.2%	1.7%	1.6%
6	-2.2%	0.1%	1.5%	1.2%
7	-2.3%	0.0%	1.5%	1.7%
8	-1.2%	-0.3%	1.1%	0.8%
9	-2.2%	0.1%	1.4%	1.4%
10	-1.3%	-1.1%	1.8%	2.2%
11	-1.5%	-0.2%	1.1%	0.8%

6.3 Post-Flame Fine Wood (PFFW)

PFFW measurements are very similar in nature to PFMW measurements, the primary difference being the axial data collection location being 1.55 m from the burner exit instead of 1.15 m in order to ensure that no visible flame was present in the line of sight. Measurements were taken at several radial locations across the BFR. PFFW measurements were taken in a region where hot combustion gases and hot particles were both present in the line of sight.

The radial temperature profile for PFFW is presented in Figure 6-15. These data were measured with a suction pyrometer and were taken at 1.55 m axially below the burner (same axial distance as the optical measurements) immediately after taking the optical measurements. The suction pyrometer was inserted at radial locations ranging from 0.1 to 0.6 m in 0.1 m increments. The profile is flat across the measurement region, with minimum and maximum values of 1261.5 and 1294.3 K, respectively. This profile was assumed to behave as previous measurements, with lower temperatures near the walls, so optical measurements were taken with the optical probe and cold target both inserted at least 0.1 m from the south and north walls, respectively. Approximatly three suction pyrometer measurements were taken at each location and then averaged to provide the temperatures as listed in the figure. Temperature fluctuations for each location were less than 10 K.

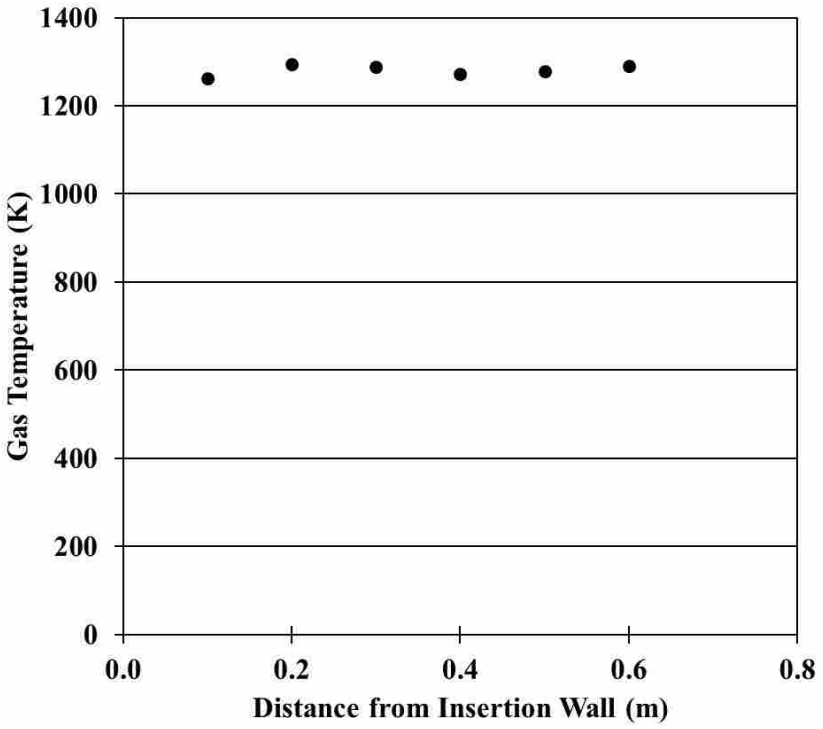

Figure 6-15: Radial gas temperature profile in the BFR for PFFW measurements using a suction pyrometer.

Results for all PFMW conditions are presented in tabular format in Table 6-3. The type of data in each column is the same as described for Table 6-3 as described in Section 6.2. Gas temperature and concentration and broadband temperature and emissivity were determined using algorithm 2 as described in Section 5.3 for particles, with no background wall emission being assumed to be present. It should be noted that one measurement with a path length of 0.05 m was excluded from the PFFW data set presented in the table because the signal to noise ratio appeared too small for the algorithm to produce a reasonable gas temperature.

Table 6-5: PFFW data collection positions and results.

Test #	Probe Position (m)	Target Position (m)	Path Length (m)	Meas. Center (m)	$T_{Av, S.P.}$ (K)	$T_{optical}$ (K)	$Y_{H2O,Opt.}$	$Y_{H2O,ex}$	$T_{Broad.}$ (K)	$\varepsilon_{Part.}$
1	0.10	0.65	0.55	0.38	1280.9	1239.2	0.179	0.108	1137.3	0.17
2	0.10	0.65	0.55	0.38	1280.9	1221.7	0.202	0.108	1144.9	0.17
3	0.10	0.65	0.55	0.38	1280.9	1232.7	0.209	0.108	1146.9	0.18
4	0.10	0.65	0.55	0.38	1280.9	1242.8	0.199	0.107	1148.6	0.18
5	0.10	0.55	0.45	0.33	1280.9	1251.8	0.163	0.108	1141.9	0.06
6	0.10	0.55	0.45	0.33	1280.9	1247.6	0.140	0.103	1122.8	0.06
7	0.10	0.45	0.35	0.28	1279.0	1205.1	0.147	0.102	1086.8	0.16
8	0.10	0.45	0.35	0.28	1279.0	1181.4	0.177	0.102	1099.6	0.17
9	0.10	0.45	0.35	0.28	1279.0	1205.4	0.174	0.103	1106.8	0.21
10	0.20	0.45	0.25	0.33	1284.8	1247.1	0.127	0.102	984.6	0.02
11	0.20	0.45	0.25	0.33	1284.8	1236.5	0.166	0.103	1061.9	0.02
12	0.20	0.45	0.25	0.33	1284.8	1237.8	0.138	0.104	1032.3	0.02
13	0.30	0.45	0.15	0.38	1280.1	1256.7	0.122	0.103	912.3	0.02
14	0.30	0.45	0.15	0.38	1280.1	1218.2	0.150	0.105	896.4	0.03
15	0.30	0.45	0.15	0.38	1280.1	1249.1	0.137	0.106	927.4	0.02
16	0.40	0.45	0.05	0.43	1271.7	1381.9	0.113	0.103	N/A	N/A
17	0.40	0.45	0.05	0.43	1271.7	1467.2	0.088	0.105	N/A	N/A
18	0.40	0.55	0.15	0.48	1280.5	1280.5	0.122	0.108	907.2	0.02
19	0.40	0.55	0.15	0.48	1280.5	1288.5	0.119	0.103	895.2	0.03
20	0.40	0.55	0.15	0.48	1280.5	1240.9	0.137	0.105	1030.8	0.01
21	0.40	0.65	0.25	0.53	1280.5	1243.0	0.137	0.105	1100.0	0.01
22	0.40	0.65	0.25	0.53	1280.5	1252.2	0.109	0.102	963.0	0.02
23	0.40	0.65	0.25	0.53	1280.5	1270.8	0.120	0.104	985.3	0.02
24	0.10	0.65	0.55	0.38	1280.9	1255.8	0.143	0.105	1184.4	0.02

Table 6-5: PFFW data collection positions and results, continued.

Test #	Probe Position (m)	Target Position (m)	Path Length (m)	Meas. Center (m)	$T_{Av, S.P.}$ (K)	$T_{optical}$ (K)	$Y_{H2O,Opt.}$	$Y_{H2O,ex}$	$T_{Broad.}$ (K)	$\varepsilon_{Part.}$
25	0.10	0.65	0.55	0.38	1280.9	1262.8	0.150	0.109	1187.5	0.03
26	0.10	0.65	0.55	0.38	1280.9	1241.3	0.125	0.099	1180.1	0.02

6.3.1 Optical and Suction Pyrometer Temperature

Optical and suction pyrometer temperature are presented in Figure 6-16 as a function of path length. Because the suction pyrometer data did not change with path length, the optical data can be more readily compared. Excellent agreement (less than 4% error) is seen at all path lengths except at 0.05 and 0.35 m. The poor agreement at 0.05 m is consistent with all of the data and is explained by a weak signal. A plot of temperature error as a function of path length is shown in Figure 6-17 where the data at 0.05 m have been omitted because the error is so much larger it obscures the remaining data. The data have been split into two categories, one where the broadband emissivity is 0.06 and lower labeled “well aligned” and another where the broadband emissivity is greater than 0.06 labeled “not well aligned”. The well-aligned data exhibit the same behavior observed with all post-flame measurements, as the path length shortens the error becomes larger and more scattered. Path lengths 0.3 m and greater produce temperatures within 2% of the suction pyrometer temperature. The method used to process these data to obtain temperature assumes no wall emission, which is the case when looking into the cold cavity. High broadband emissivity is evidence of reflection from walls, which is not properly accounted for using the broadband particle algorithm. The temperatures obtained when broadband emissivities are high is reasonable but in lower negative error than the well-aligned temperatures.

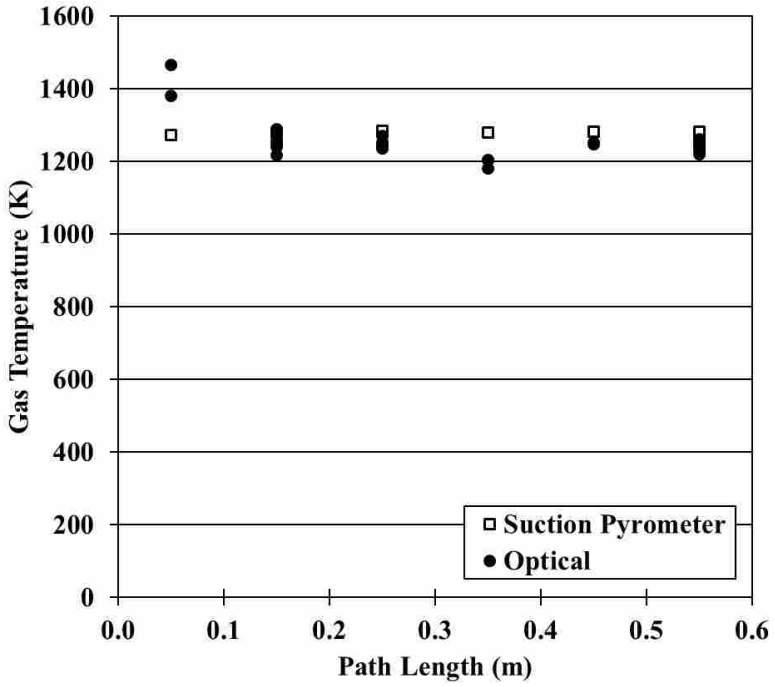

Figure 6-16: Selected temperature comparisons for PFFW measurements, plotted by path length.

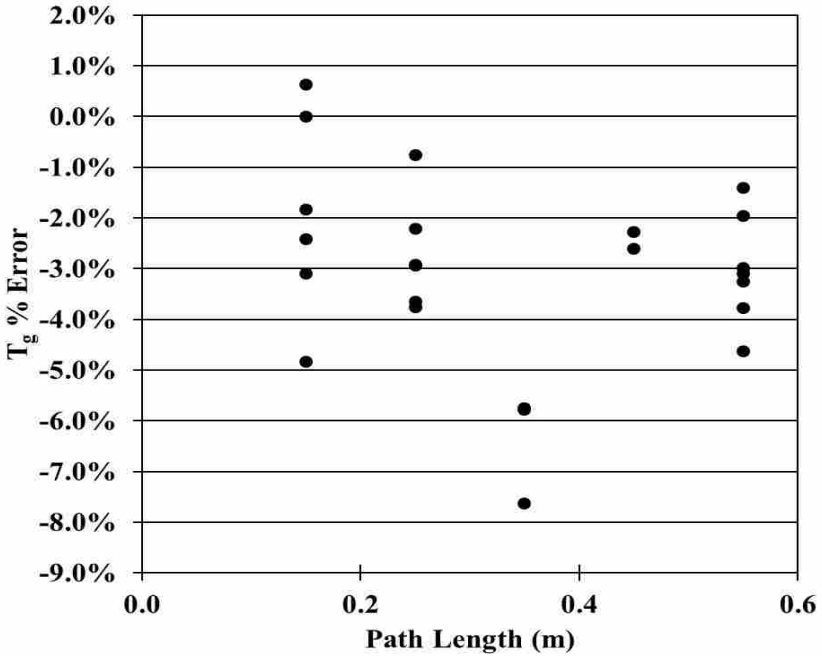

Figure 6-17: Temperature error as a function of path length for PFFW.

6.3.2 Optical Concentration Measurements

A comparison of the optically measured and reference H_2O concentration as a function of path length is shown in Figure 6-18, along with a dashed line for the stoichiometric value of Y_{H2O} for the wood fuel used, being the maximum possible value of Y_{H2O} as discussed in Section 6.2.2. The exhaust reference concentrations are relatively constant enabling a comparison even when multiple data points exist at a given path length. The data have been separated into two groups, those where the probe was in good alignment with the cold cavity (broadband emissivity 0.06 and lower) and those were alignment was not as good (broadband emissivity greater than 0.06).

All of the poorly aligned data are well above the maximum possible (stoichiometric) value for Y_{H2O}. This could be because of the reflection that was enabled by not having proper alignment with the cold cavity target. The reflection increases the signal magnitude, thus giving the appearance of higher Y_{H2O}.

The rest of the Y_{H2O} values tend to be scattered around the stoichiometric concentration, with the exception of the shortest path length (0.05 m). Given that the temperature measurements were highly inaccurate at the shortest path length, their apparently good agreement with the reference value is considered to be accidental. For the remaining measurements, it is thought that they are affected by the same problems as discussed in Section 6.2.2, namely inaccuracy in the temperature measurements, errors in the signal which are introduced via noise, and potential effects of CO_2.

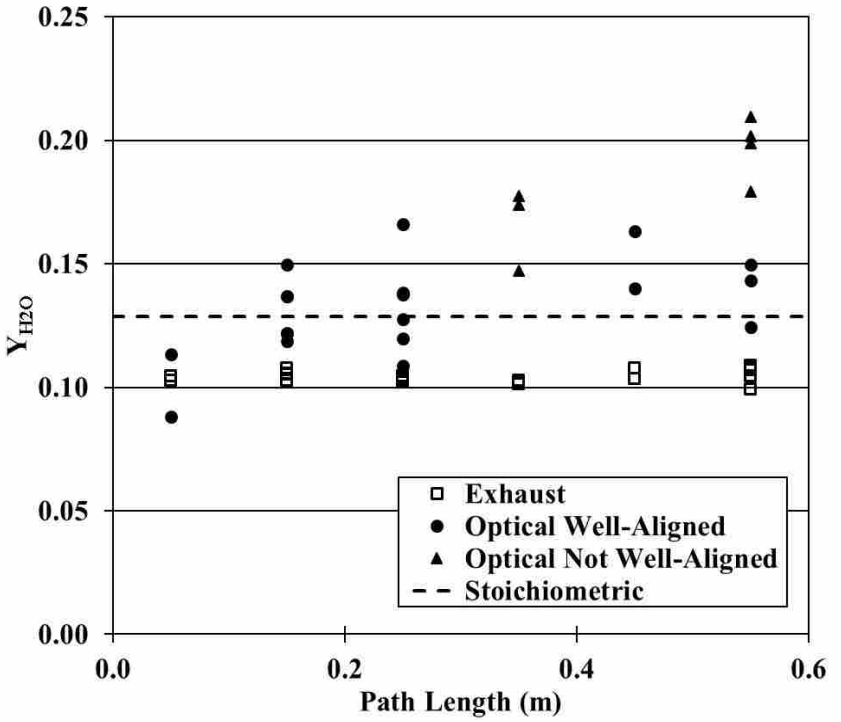

Figure 6-18: Optical and reference H_2O conentration as a function of path length.

6.3.3 Broadband Temperature and Emissivity

The broadband emissivity as a function of path length is shown in Figure 6-19. If the emissivity is originating from particles, the emissivity should increase with an increasing number of particles in the path and generally the emissivity should increase with increasing path length. Because this is not observed, there appears to be some other factor that is more dominant.

At the longest path length (0.55 m), assuming constant operating conditions, all emissivities should be the same but they are not. The two groupings at 0.55 m correlate with the time periods when data were taken and the probe and target were realigned in between the two groups. Similarly, the emissivity increased dramatically when the probe was moved to change the path length from 0.45 m (Tests 5-6) to 0.35 m (Tests 7-9) when it should have decreased.

Both of these high emissivity groupings suggest the high emissivity is caused by poor alignment and reflection off the cold cavity not from particles in the path.

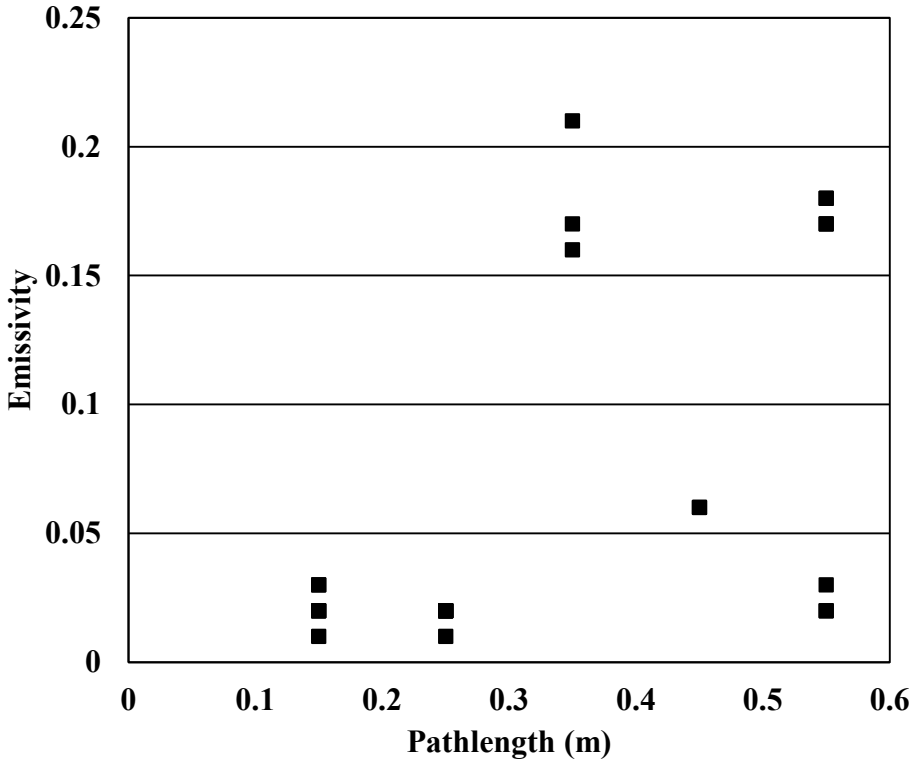

Figure 6-19: Broadband emmisivity as a function of path length for PFFW.

The broadband temperatures as a function of path length are shown in Figure 6-20. When the probe is well aligned and the intensity is measurable, the broadband temperature should represent the particle temperature. At the longest path length the broadband temperature is 1180 K. This is similar to the gas temperature. As the path length decreases, the well-aligned data produced so little signal that the temperature measurements become unreliable and seem unrealistically low. For cases where the probe was not well aligned and emissivity is high, the

broadband temperature is 1137 and 1086 K, below the gas temperature but reasonable for wall temperature.

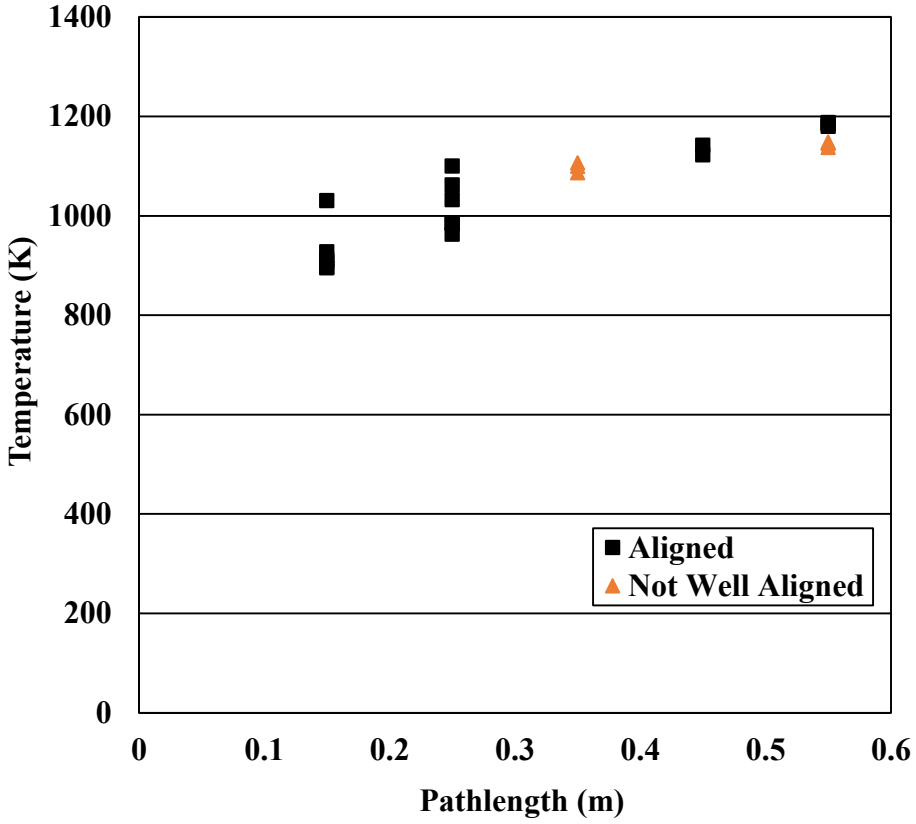

Figure 6-20: Broadband temperature as a function of path length for PFFW.

6.3.4 Integrated Spectral Intensity

In the interest of investigating the efficacy of these measurements related to total radiative heat transfer, a comparison is presented between measured and broadened modeled intensity data. The broadening method is presented and discussed in Chapter 7. A portion of the spectrum for the measurement Test #5 presented in Table 6-5 is used for this comparison which

is presented in Figure 6-21 as the measured data. The model was produced as described in Section 5.4. This is one of the tests where the probe was not in good alignment, which can be seen by the relatively large baseline intensity of almost 500 $W/m^2/\mu m/sr$. The model is in relatively good agreement. There is a modeled peak for every measured peak. The large measured peaks are typically higher than the modeled peaks while the total areas appear to be similar. When broadband intensity is large as in this case, it is more difficult to match the peaks because the area in single peaks is small compared to a constant intensity across all wavelengths.

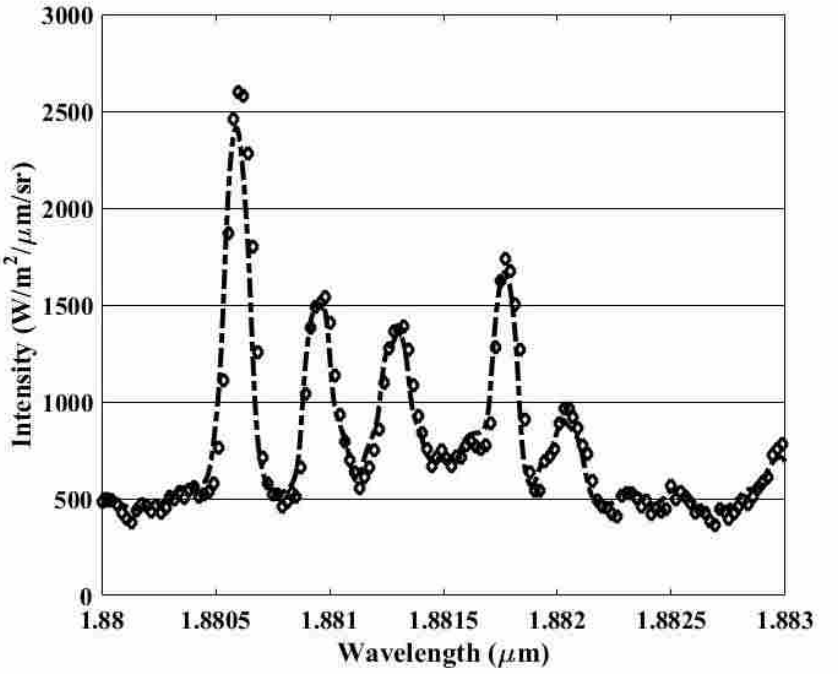

Figure 6-21: Comparison of a PFFW measurement and model for PFFW Test #5.

In order to more closely examine how well the measured and modeled intensity correspond to each other, the percent differences between measured and modeled spectral intensity band integrals are presented in Table 6-6 for all PFFW measurements. Measured

integrated areas for band A are consistently larger than the model integrated areas while bands B, C, and E have lower integrated intensities. Exceptions to this are Tests 16 and 17 where the signal was too small to produce a broadband temperature and gas temperatures were also inaccurate. Bands C and E are in the closest agreement over all tests, which is consistent with the observation that these two bands typically produce the best temperatures but they are also the two bands closest to each other in the spectrum. Although differences between band integrals is small, additional data are required to investigate differences over a broader range of the spectrum.

Table 6-6: Percent differences between modeled and measured integrated bands.

	Band			
Test #	A	B	C	E
1	-1.8%	0.7%	0.7%	0.2%
2	-1.7%	0.6%	0.7%	0.1%
3	-1.9%	0.7%	0.7%	0.1%
4	-1.8%	0.7%	0.7%	0.1%
5	-2.9%	0.9%	1.2%	0.7%
6	-2.3%	0.7%	0.9%	0.7%
7	-1.6%	0.5%	0.7%	0.3%
8	-2.0%	0.7%	1.0%	0.3%
9	-1.7%	0.5%	0.9%	0.3%
10	-2.4%	0.5%	0.9%	1.2%
11	-3.1%	0.6%	1.3%	1.0%
12	-2.3%	0.3%	1.0%	1.1%
13	-1.3%	-0.1%	0.8%	1.1%
14	-1.6%	-0.2%	1.0%	0.9%
15	-0.6%	-0.3%	0.4%	0.7%
16	7.5%	-4.3%	-1.0%	-0.1%
17	9.1%	-4.3%	-2.0%	-1.0%
18	-1.6%	-0.3%	1.2%	1.5%

Table 6-6: Percent differences between modeled and measured integrated bands, continued.

	Band			
Test #	A	B	C	E
19	-1.9%	-0.2%	1.3%	1.7%
20	-1.6%	-0.5%	1.4%	1.4%
21	-2.9%	1.2%	0.5%	0.8%
22	-2.8%	0.4%	1.3%	1.9%
23	-2.2%	0.4%	0.9%	1.4%
24	-2.5%	0.8%	0.8%	1.0%
25	-2.4%	0.8%	0.7%	0.8%
26	-2.1%	0.4%	0.8%	1.3%

6.4 In-Flame Measurements (IFNG and IFFW)

IFNG and IFFW measurements were taken with the visible flame in the line of sight of the measurements. This was accomplished for IFNG measurements by reducing the swirl of the BFR's burner, which lengthened out the flame until it was in the line of sight (1.15 m axially from the burner exit). For IFFW, the measurements were taken higher in the reactor (0.62 m from the burner exit), were the visible flame was always present at the BFR burner's maximum swirl. For IFNG measurements, hot gases and soot were emitting in the region viewed. IFFW measurements were the most complex measurements, because they included a combination of fuel particles, soot, and hot gases. Temperature and concentration gradients expected near a visible flame added to the complexity of both IFNG and IFFW. Many similarities were found between IFNG and IFFW measurements and results so both are discussed here.

Figure 6-22 shows the temperature profile of IFNG conditions as measured with a suction pyrometer taken at the same location axially as the optical measurements (1.15 m).

Measurements were taken every 0.05 m, from 0.05 m to 0.5 m from the south wall, then one more was taken at 0.6 m with data at 0.55 m being accidentally neglected. Most of the measurement region appears to have a flat temperature profile, with the flame slightly favoring the south wall and leading to lower temperatures closer to the north wall. As with other measurements, the optical probe and cold target were inserted at least 0.1 m from the south and north walls respectively to avoid the regions of steepest temperature gradients near the walls. The suction pyrometer measurements were averaged to obtaine temperature over a given pathelength. All IFNG suction pyrometer measurements were taken after the optical measurements. Approximatly three suction pyrometer measurements were taken at each location and then averaged to provide the temperatures as listed in the figure with temperature variation on the order of 20 K.

Figure 6-23 depicts the radial gas temperature profile for IFFW conditions. These measurements were taken via suction pyrometer at several radial locations (0.1 m to 0.6 m at 0.1 m increments), at a distance of 0.62 m from the burner exit. Approximately three measurements were taken at each radial location, except at 0.6 m where several were taken, then averaged together to determine the results presented in the figure. The measurements at each location were all within 30 K of each other, with the exception of 0.6m, where the fluctuations were on the order of 100 K. As can be seen in the figure, the profile was flat across most of the reactor, until the 0.6 m location where a large spike (76.6 K) was seen. This is assumed to be due to the flame strongly favoring the north side of the reactor in this case, and at this axial location. The optical probe and cold target were again kept at least 0.1 m from each wall to avoid colder regions near the walls. These measurements were averaged over each optical measurement region to obtain reference gas temperatures for IFFW measurements.

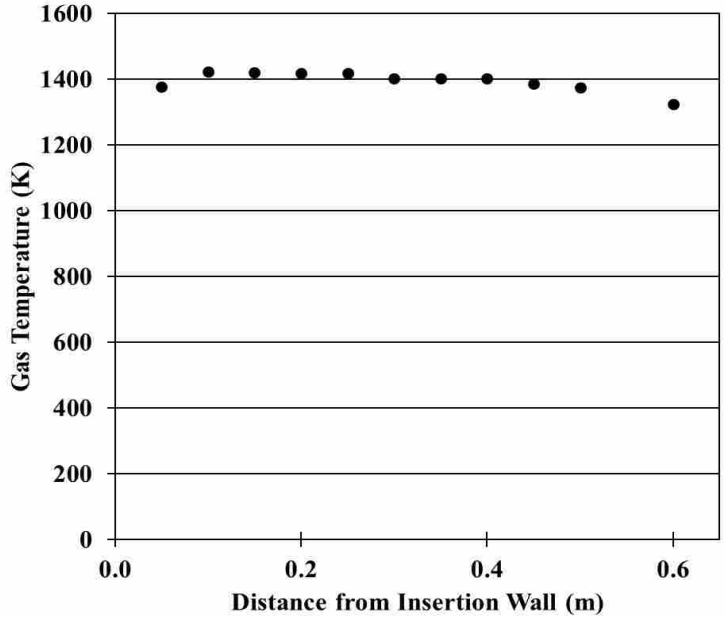

Figure 6-22: Radial gas temperature profile in the BFR for IFNG measurements using a suction pyrometer.

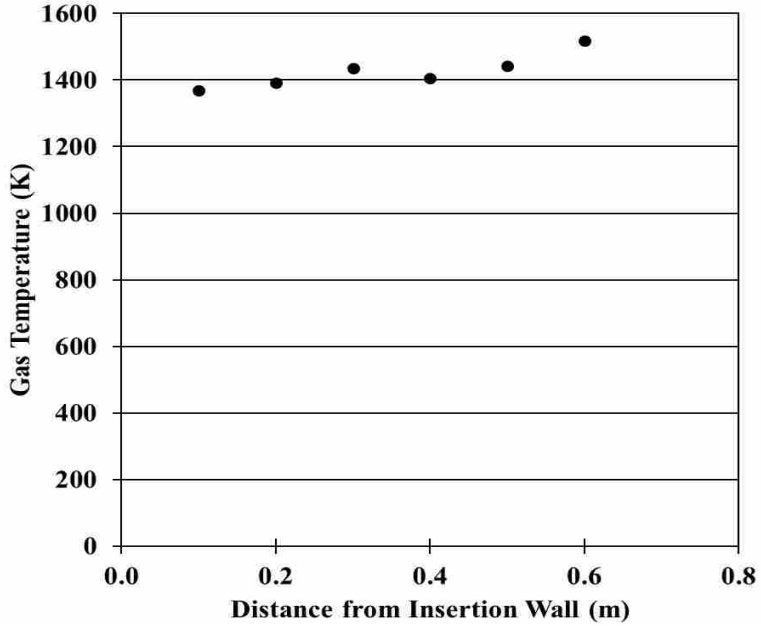

Figure 6-23: Radial gas temperature profile in the BFR for IFFW measurements using a suction pyrometer.

Table 6-7 and Table 6-8 respectively present the full measured data sets for IFNG and IFFW measurements. Data are presented in the same order and as described in Section 6.2, now with ε_{part} being used to indicate fuel and/or soot particles, rather than simply fuel particles.

6.4.1 Optical and Suction Pyrometer Temperature

A comparison of optical and suction pyrometer temperatures as a function of the center position of the optical path length is shown in Figure 6-24. The optical data are seen to be more scattered but on average as shown in Figure 6-25 are very close to the suction pyrometer temperatures. The scatter in the optical data is likely a result of both the uncertainty of the method and fluctuations in the flame. The temperature variation is approximately ±150 K (-13 to 4.6%) compared to the suction pyrometer which varied on the order of 20 K. In spite of intensity from radiating soot, the gas temperature was still successfully extracted from the spectral intensity.

Since the suction pyrometer temperature is not a strong function of position, the optical and suction pyrometer measurements can be compared as a function of path length as shown in Figure 6-26. The figure shows gas temperatures at path lengths between 0.15 and 0.45 m are in good agreement (within 7%) with the suction pyrometer. Data with high broadband emissivities for the measured path length have been identified from the rest of the data and tend to produce lower temperatures. These data are thought to be poorly aligned. The longer path lengths produced higher gas temperatures than the suction pyrometer.

Table 6-7: IFNG data collection positions and results.

Test #	Probe Position (m)	Target Position (m)	Path Length (m)	Meas. Center (m)	$T_{Av, S.P.}$ (K)	$T_{optical}$ (K)	$Y_{H2O,Opt.}$	$Y_{H2O,ex}$	$T_{Broad.}$ (K)	$\varepsilon_{Part.}$
1	0.10	0.65	0.55	0.38	1392.8	1381.7	0.153	0.163	1467.3	0.023
2	0.10	0.55	0.45	0.33	1399.6	1401.0	0.131	0.164	1773.1	0.015
3	0.10	0.45	0.35	0.28	1408.9	1420.2	0.147	0.159	1730.7	0.014
4	0.20	0.45	0.25	0.33	1404.5	1469.2	0.129	0.164	1820.3	0.011
5	0.30	0.45	0.15	0.38	1397.7	1454.1	0.159	0.163	1756.3	0.007
6	0.30	0.45	0.15	0.38	1397.7	1385.7	0.138	0.162	1688.2	0.004
7	0.30	0.45	0.15	0.38	1397.7	1316.0	0.140	0.160	1683.8	0.003
8	0.30	0.55	0.25	0.43	1385.9	1401.8	0.152	0.162	1659.9	0.015
9	0.35	0.55	0.20	0.45	1382.8	1384.2	0.146	0.161	1598.6	0.009
16	0.40	0.55	0.15	0.48	1377.9	1402.6	0.139	0.157	1644.8	0.011
17	0.40	0.55	0.15	0.48	1377.9	1316.3	0.142	0.160	1582.9	0.006
18	0.40	0.65	0.25	0.53	1367.2	1331.9	0.151	0.162	1596.4	0.012
19	0.40	0.65	0.25	0.53	1367.2	1387.3	0.147	0.167	1629.8	0.012
20	0.45	0.65	0.20	0.55	1358.7	1307.0	0.152	0.167	1502.2	0.005
21	0.50	0.65	0.15	0.58	1349.6	1267.0	0.123	0.164	1460.2	0.005
22	0.50	0.65	0.15	0.58	1349.6	1335.7	0.139	0.172	1570.7	0.010

Table 6-8: IFFW data collection positions and results.

Test #	Probe Position (m)	Target Position (m)	Path Length (m)	Meas. Center (m)	$T_{Av.\ S.P.}$ (K)	$T_{optical}$ (K)	$Y_{H2O,Opt.}$	$Y_{H2O,ex}$	$T_{Broad.}$ (K)	$\varepsilon_{Part.}$
1	0.10	0.65	0.55	0.38	1427.2	1575.1	0.091	0.105	1701.9	0.17043
2	0.10	0.65	0.55	0.38	1427.2	1589.7	0.079	0.104	1630.0	0.18778
3	0.10	0.65	0.55	0.38	1427.2	1571.7	0.091	0.101	1601.5	0.18084
4	0.10	0.55	0.45	0.33	1427.2	1485.2	0.110	0.103	1528.6	0.19157
5	0.10	0.45	0.35	0.28	1400.5	1318.1	0.205	0.105	1300.1	0.39785
6	0.10	0.45	0.35	0.28	1400.5	1318.0	0.209	0.108	1284.2	0.43876
7	0.10	0.45	0.35	0.28	1400.5	1254.6	0.317	0.105	1153.3	0.6853
8	0.10	0.55	0.45	0.33	1427.2	1343.3	0.190	0.103	1385.4	0.25661
9	0.10	0.55	0.45	0.33	1427.2	1430.9	0.131	0.107	1428.9	0.23426
10	0.10	0.55	0.45	0.33	1427.2	1446.7	0.128	0.105	1465.1	0.20276
11	0.10	0.45	0.35	0.28	1400.5	1380.1	0.136	0.103	1545.9	0.08061
12	0.10	0.45	0.35	0.28	1400.5	1406.6	0.116	0.100	1544.2	0.07753
13	0.10	0.45	0.35	0.28	1400.5	1411.5	0.137	0.104	1587.7	0.10044
14	0.20	0.45	0.25	0.33	1411.0	1318.6	0.122	0.101	1460.6	0.08126
15	0.20	0.45	0.25	0.33	1411.0	1437.1	0.131	0.101	1596.4	0.05308
16	0.20	0.45	0.25	0.33	1411.0	1397.2	0.128	0.101	1530.7	0.05307
17	0.30	0.45	0.15	0.38	1420.7	1358.5	0.114	0.102	1459.9	0.04341
18	0.30	0.45	0.15	0.38	1420.7	1350.6	0.127	0.103	1462.3	0.03584
19	0.30	0.45	0.15	0.38	1420.7	1315.6	0.101	0.105	1371.9	0.14951
20	0.40	0.45	0.05	0.43	1405.8	1213.3	0.151	0.100	1170.4	0.05653
21	0.40	0.45	0.05	0.43	1405.8	1244.2	0.243	0.103	1385.7	0.05431
22	0.40	0.45	0.05	0.43	1405.8	1165.5	0.252	0.104	1363.1	0.04271

Table 6-8: IFFW data collection positions and results, continued.

Test #	Probe Position (m)	Target Position (m)	Path Length (m)	Meas. Center (m)	$T_{Av.\ S.P.}$ (K)	$T_{optical}$ (K)	$Y_{H2O,Opt.}$	$Y_{H2O,ex}$	$T_{Broad.}$ (K)	$\varepsilon_{Part.}$
23	0.10	0.65	0.55	0.38	1427.2	1523.6	0.086	0.105	1526.0	0.17967
24	0.10	0.65	0.55	0.38	1427.2	1504.5	0.103	0.105	1543.4	0.17668
25	0.10	0.65	0.55	0.38	1427.2	1553.3	0.088	0.093	1513.7	0.19867

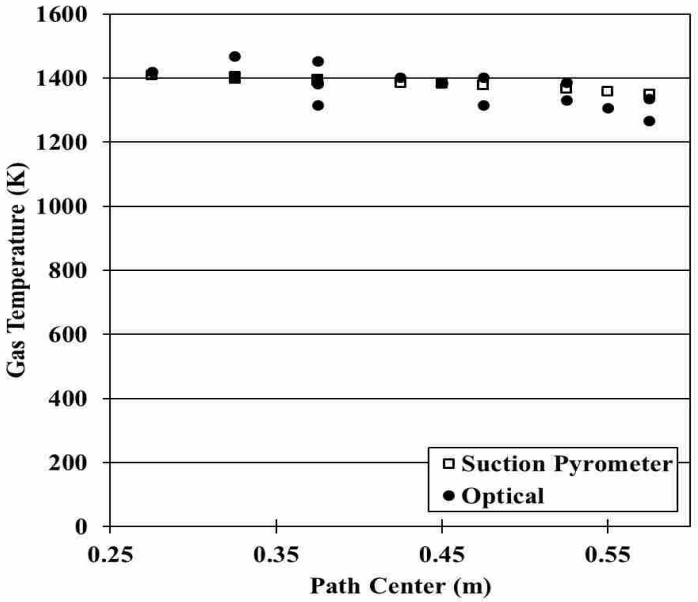

Figure 6-24: Optical and Suction pyrometer temperatures as a funciton of path length centerline for IFNG.

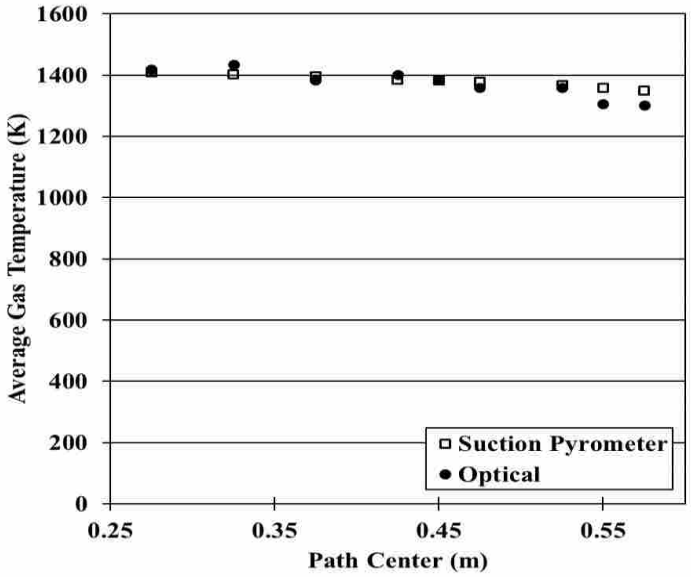

Figure 6-25: Avearage optical H_2O temperature as a function of path length center position for IFFW.

A comparison of broadband and gas temperature is shown in Figure 6-27. The average optical gas temperature and all of the broadband temperatures are shown. For tests where the probe was well aligned, the broadband temperature is higher than the gas temperature suggesting that the broadband temperature represents particles that are at a higher temperature than the gas. When the probe is poorly aligned, the broadband temperature is lower than the gas temperature suggesting that the broadband temperature is influenced by intensity from walls reflecting off the cold target. Particles, especially fuel particles, were likely reflecting, or back-scattering, gas emission into the probe's line of sight as well, leading to similar effects as wall reflection.

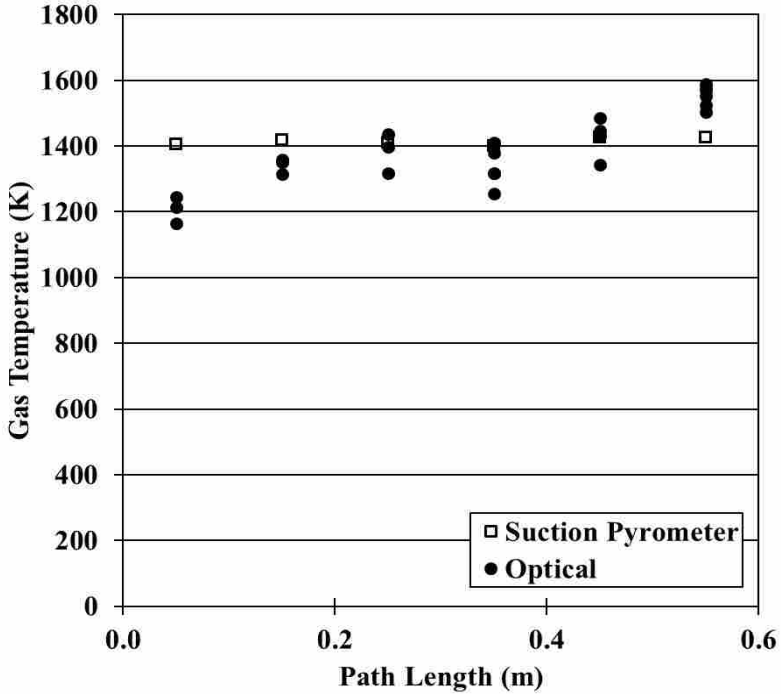

Figure 6-26: IFFW gas temperature comparisons between suction pyrometer and optical measurements.

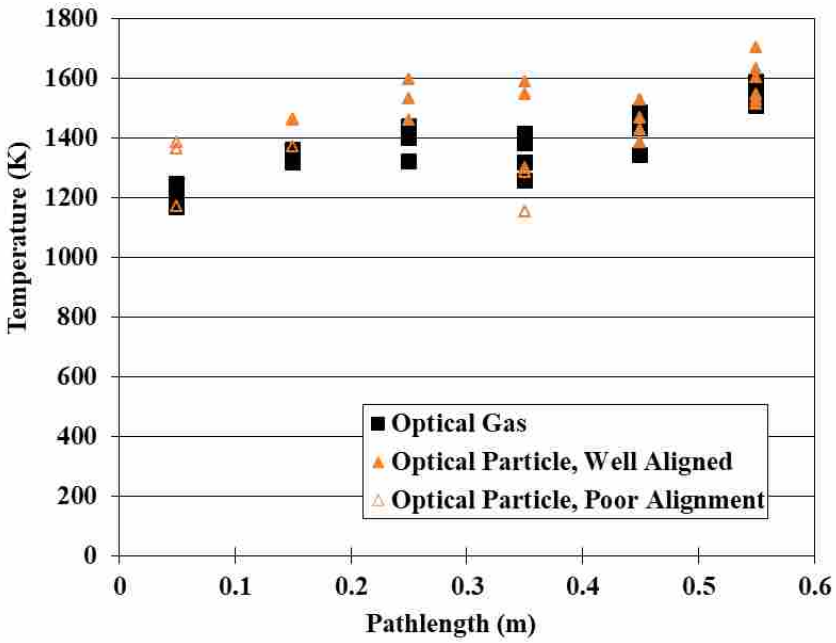

Figure 6-27: Comparison of optical gas and particle temperatures of IFFW.

6.4.2 Optical Concentration Measurements

IFNG optical concentrations for H_2O are compared to reference H_2O concentrations calculated from exhaust O_2 values in Figure 6-28. The reference values of Y_{H2O} were calculated as outlined in Section 5.5 when using exhaust measurements of Y_{O2}. The optical measurements were obtained in the flame zone before combustion was complete and some of the fuel hydrogen was not yet converted to H_2O. The optical concentration should therefore be lower than the reference value which is calculated based on complete combustion. As with post-flame measurements, the concentration measurements are highly scattered. The scatter is likely a result of uncertainty in the measurement as well as fluctuations in the actual concentration.

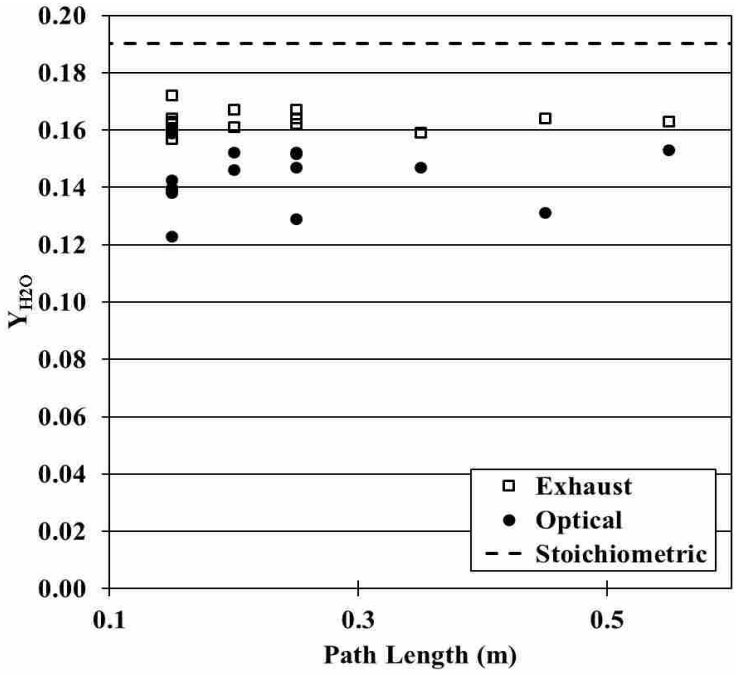

Figure 6-28: Optical and reference H2O concentration as a function of path length for IFNG.

Figure 6-29 compares optical and reference H_2O concentration as a function of path length for IFFW. In this case, the optically measured values are higher than the reference values. The majority of the poorly aligned data are well above the stoichiometric maximum, and the majority of the well-aligned data are below the stoichiometric value.

At this point, no conclusion can be drawn regarding the spatial resolution of optical Y_{H2O} measurements, as reliable reference data are not available.

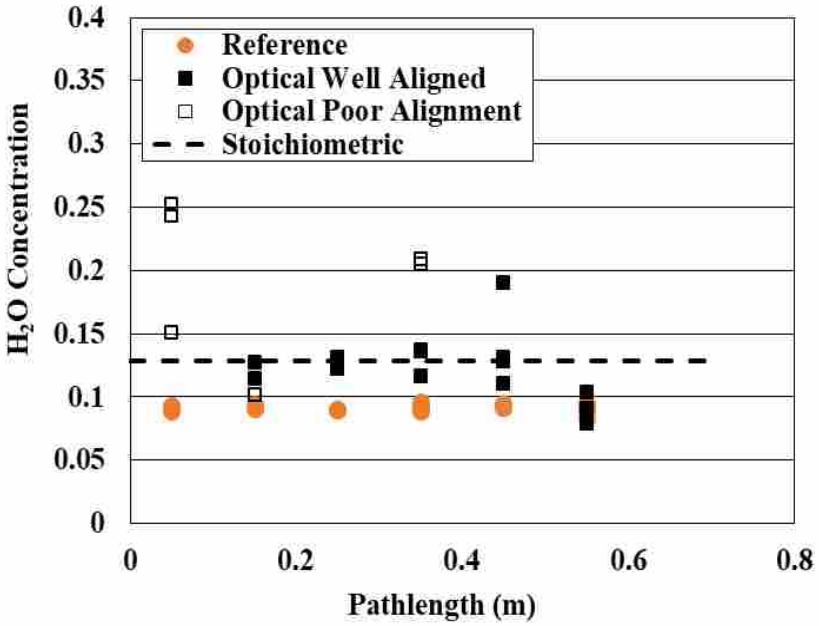

Figure 6-29: IFFW YH2O comparisons between optical measurements and reference values based on exhaust YO_2 measurements.

6.4.3 Broadband Intensity and Emissivity

The optical probe collects broadband emission as well as the spectral gas emission. For IFNG measurements, this broadband emission is a mixture of background reflection off the face of the cold target and particle emission from soot particles. For IFFW measurements, broadband emission consists of fuel and soot particle emission. The broadband emission is visually well fit by a Planck gray body as demonstrated in Figure 6-30 (IFNG Test # 2) and Figure 6-31 (IFFW Test # 7). It can be seen in the figures that the soot and fuel particles appear to behave as a gray body in the spectral region used in this work.

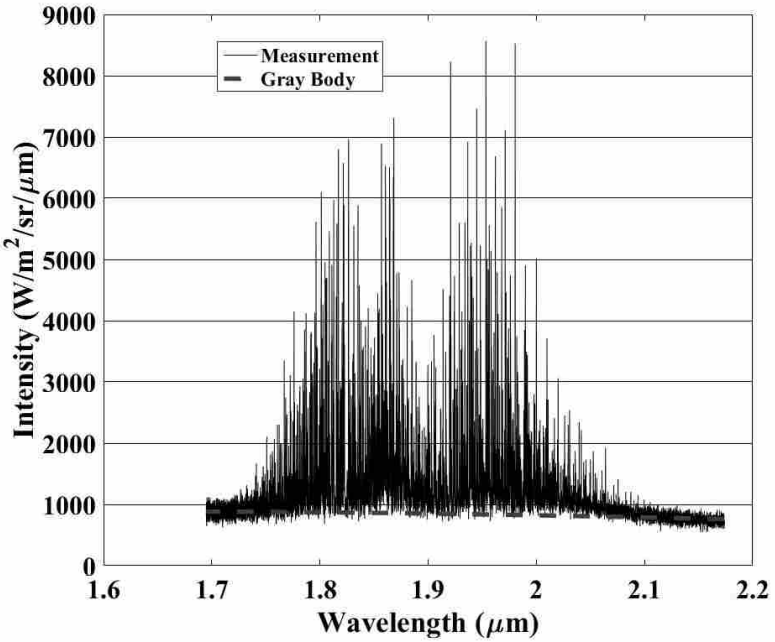

Figure 6-30: Comparison of a typical IFNG measurement and true gray-body radiation (Test #3).

The broadband temperatures measured in in-flame conditions ranged between 1400 and 1800 K for IFNG and from 1150 to 1700 K for IFFW. The upper temperatures for both data sets are much higher than any previous background temperature investigated in this work. This is to be expected from very hot soot in particular, as the soot forms at the flame itself. The lowest background temperatures tend to be at the shortest path lengths, suggesting that these measurements have fewer particles in the measurement volume, which is more likely when looking at a shorter path length than a longer one. The longer path lengths have more volume in the line of sight, making it more likely that more particles will pass through them; the opposite is true of the shortest path lengths.

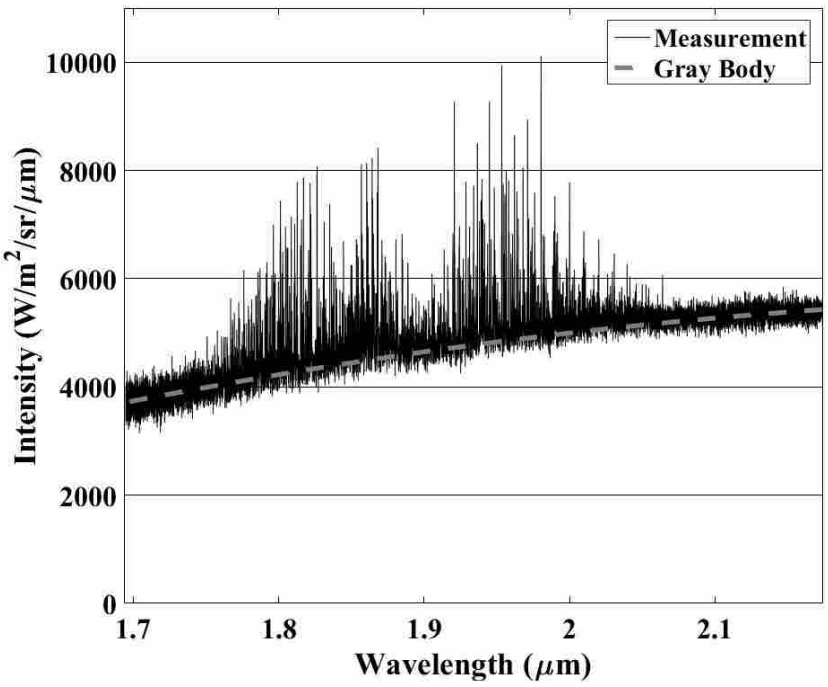

Figure 6-31: Comparison of a typical IFFW measurement and true gray-body radiation (Test #7).

6.4.4 Integrated Spectral Intensity

In the interest of investigating the efficacy of these spectral measurements (IFNG and IFFW) related to measuring or enabling the calculation of total radiative heat transfer, a comparison is presented between a measurement and broadened modeled intensity data. A small portion of the spectrum for the measured and modeled data for Test # 3 IFFW is presented in Figure 6-14. A similar comparison for IFFW (Test # 11) is presented as Figure 6-33. The modeled data were produced using the model as described in Section 5.3 with values for $C_{abs,\lambda}$ from the work of Pearson et al. [18], with the optically measured gas temperature and concentrations, and the optically measured particle temperature and emissivity. A non-reflecting, non-emitting boundary condition was imposed with all broadband emission assumed to come

from particles in the measurement volume. The modeled and measured values are in good visual agreement, although that of IFFW does have measured peaks that appear to be higher than the modeled peaks. The model does appear to provide an accurate representation of what is being measured.

In order to quantitatively asses the agreement between the measured and modeled intensity, a comparison between the integrated modeled and measured intensities is provided in Table 6-9 and Table 6-10. As can be seen in the tables, the agreement between integrated bands is excellent. This would be expected in at least one band, as the method of determining the concentration effectively forces a concentration match between the measured and model integrals. However, this can only be enforced for a single integrated band and therefore a match at other bands is an indication of overall good agreement.

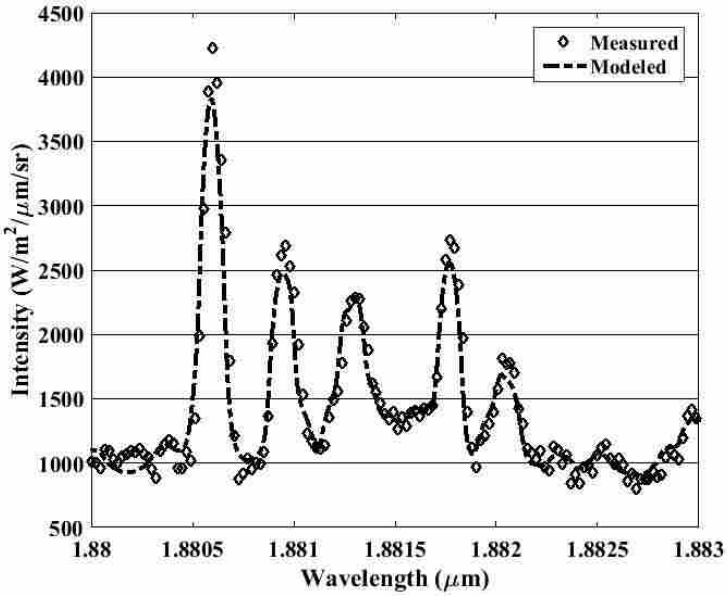

Figure 6-32: Broadened model compared to the measurement IFNG Test #3.

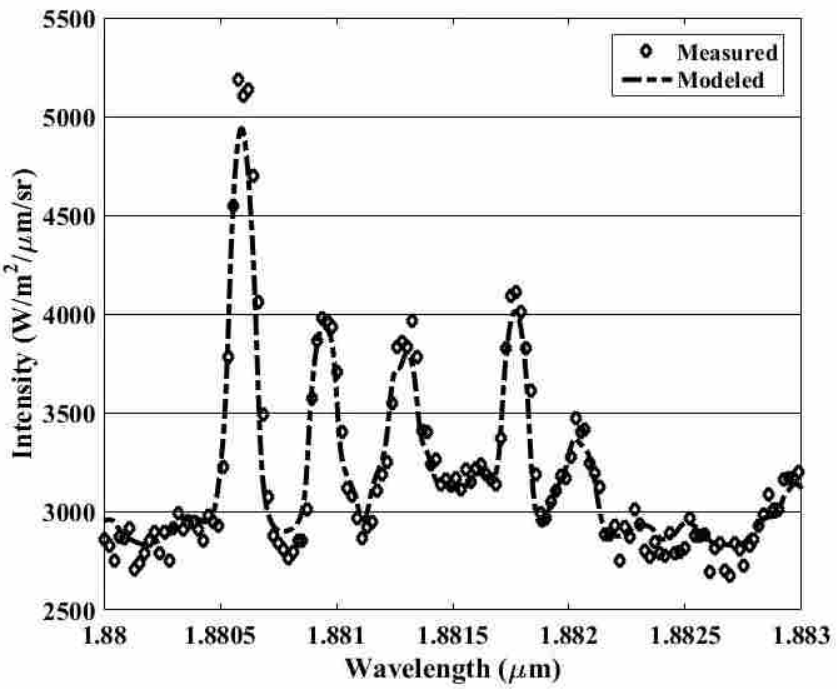

Figure 6-33: Broadened model calculated using optical measurement values and compared to the corresponding optical measurement (IFFW Test #11).

Table 6-9: IFNG comparisons of integrated intensities between optical measurements and modeled intensities for bands of interest.

	Band			
Test #	**A**	**B**	**C**	**E**
1	-1.8%	0.6%	0.6%	0.6%
2	-0.9%	0.0%	0.5%	0.5%
3	-1.1%	0.0%	0.6%	0.4%
4	-0.8%	0.1%	0.3%	0.3%
5	-1.1%	0.0%	0.6%	0.4%
6	-1.2%	0.1%	0.6%	0.5%
7	-1.8%	0.4%	0.7%	0.6%
8	-0.6%	0.0%	0.2%	0.2%
9	-0.7%	-0.1%	0.4%	0.3%
10	-0.7%	0.0%	0.3%	0.3%

Table 6-9: IFNG comparisons of integrated intensities between optical measurements and modeled intensities for bands of interest, continued.

	Band			
Test #	A	B	C	E
11	-1.7%	0.3%	0.8%	0.5%
12	-0.3%	-0.3%	0.3%	0.2%
13	-3.2%	1.7%	0.1%	0.4%
14	-1.7%	0.1%	1.0%	0.4%
15	-1.4%	0.4%	0.5%	0.3%
16	-0.7%	-0.1%	0.4%	0.3%
17	-0.7%	0.1%	0.2%	0.2%
18	-1.1%	0.1%	0.5%	0.4%
19	-1.3%	0.3%	0.5%	0.3%
20	-1.0%	0.2%	0.4%	0.3%
21	-2.4%	0.7%	0.9%	0.6%
22	-1.4%	0.5%	0.3%	0.3%
23	-0.9%	0.1%	0.4%	0.3%

Table 6-10: IFFW comparisons of integrated intensities between optical measurements and modeled intensities for bands of interest.

	Band			
Test #	A	B	C	E
1	-0.8%	0.0%	0.5%	0.3%
2	-0.8%	0.0%	0.5%	0.3%
3	-0.9%	0.1%	0.5%	0.3%
4	-1.0%	0.1%	0.6%	0.3%
5	-1.0%	0.2%	0.6%	0.2%
6	-0.9%	0.2%	0.5%	0.1%
7	-0.9%	0.2%	0.4%	0.0%
8	-1.1%	0.3%	0.6%	0.2%
9	-1.0%	0.2%	0.6%	0.3%
10	-1.1%	0.2%	0.6%	0.3%

Table 6-10: IFFW comparisons of integrated intensities between optical measurements and modeled intensities for bands of interest, continued.

	Band			
Test #	**A**	**B**	**C**	**E**
11	-1.0%	0.1%	0.6%	0.3%
12	-0.8%	0.1%	0.5%	0.2%
13	-0.8%	0.0%	0.5%	0.2%
14	-0.7%	0.0%	0.4%	0.2%
15	-0.9%	0.0%	0.6%	0.3%
16	-0.9%	0.0%	0.5%	0.3%
17	-0.7%	-0.1%	0.4%	0.2%
18	-0.8%	0.0%	0.6%	0.3%
19	0.1%	-0.2%	-0.3%	-0.1%
20	-0.5%	0.3%	-0.1%	0.0%
21	-0.4%	-0.2%	0.3%	0.1%
22	-0.6%	-0.1%	0.5%	0.1%
23	-0.8%	0.0%	0.5%	0.3%
24	-0.8%	0.1%	0.4%	0.3%
25	-0.7%	0.1%	0.4%	0.3%

7 INVESTIGATING DIFFERENCES BETWEEN MEASUREMENTS AND THE MODEL

While many aspects of the measurements taken with the FTIR agree with the one-dimensional model described in Section 5.3, there are some notable differences. An example of modeled and measured intensities is shown in Figure 7-1 for the PFNG Test # 1 (see Table 6-1). As can be seen in the figure, there is an intensity peak in the measured data for every major emission peak in the modeled intensity data. The relative magnitudes between large and small peaks are also similar in the intensity measurements. However, measured intensity peaks are shifted horizontally from modeled peaks by 0.167 cm^{-1}, a shift that is consistent across the measured spectrum. Furthermore, the measured peaks are shorter and broader than modeled peaks, a condition referred to in this work as peak broadening. This comparison is typical of all measured and modeled spectra collected for all operating conditions collected in the BFR.

This chapter will proceed by first explaining the horizontal shift and then proceed with a discussion on the potential causes of broadening. Seven sources of potential peak broadening were investigated: 1) an inadequate number of available data points to resolve the peaks; 2) apodization; 3) pressure-induced broadening; 4) fluctuations of gas temperature and H_2O concentration; 5) performing a Fourier transform on a finite interferogram; 6) chromatic dispersion in the optical fiber; and 7) optical dispersion within the FTIR.. These sources of peak broadening are divided into two groups: 1) unlikely sources of peak broadening, which were disproven in this work from being likely sources, and 2) likely sources of broadening, which

could be neither proven nor disproven. It will be demonstrated in this chapter that the peak broadening differences can be replicated using a convolution of the modeled data. It is important to note that while all emission data collected showed peak broadening, absorption of cold water emission did not show broadening.

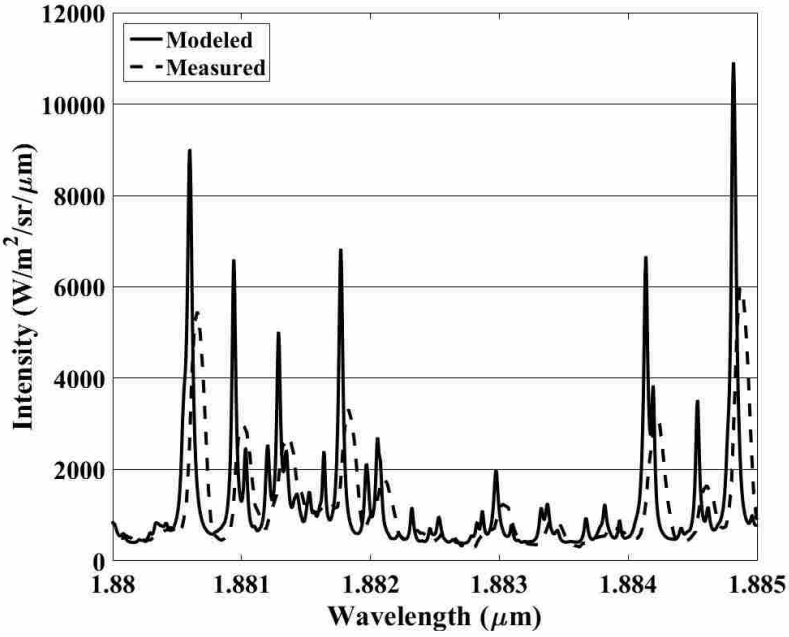

Figure 7-1: Comparison of a portion of modeled and measured intensity spectra for PFNG Test #1.

7.1 Horizontal Shift

The shift appears to be consistent at 0.167 cm^{-1} for all peaks across the measured spectrum. Direct comparisons of the model and measurements shown in Chapter 6 have already applied the shift to cause the peaks to match. In processing temperature and concentration data using integrals the shift did not produce significant differences when accounted for or ignored, so it was neglected.

The reason for the horizontal shift is relatively easily explained by FTIR uncertainty. The FTIR utilizes a laser at a known frequency to determine when to collect interferogram data points, as discussed in Section 3.3. The interferogram is then Fourier transformed, using a Fast Fourier Transform (FFT) algorithm. The data spacing on the output of an FFT is defined in Equation 7-1 [28], where F_s is the sampling frequency, and N is the total number of data points output by the FFT.

$$\Delta = \frac{F_S}{N} \tag{7-1}$$

The FTIR software utilizes a Δ based on a published laser wavenumber with five digits of accuracy. The actual Δ is slightly different because of rounding of the actually laser frequency. This difference leads to an error in the wavenumbers reported by the FTIR. Based on this theory, the error between the stated wavenumbers and the true wavenumbers is not constant for all wavenumbers but grows with the wavenumbers. Given the relatively small range of wavenumbers used in bands A - E (530 cm^{-1}), the shift appears constant over that range. A very small uncertainty in laser peak location can cause the observed difference of 0.167 cm^{-1}. For example, the 0.167 cm^{-1} shift could be the result of a difference of 0.00669 nm uncertainty in the wavelength of a 633 nm laser. The uncertainty regarding the laser wavenumber was confirmed by the FTIR manufacturer [3], as well as the observed horizontal shift being associated with an uncertainty in the laser wavelength. As a result the measured data were shifted by a constant value to match the peaks of the modeled and measured data in the wavenumber domain before being translated to the wavelength domain.

7.2 Unlikely Sources of Peak Broadening

Several possible reasons for the peak broadening were considered but were subsequently removed from consideration as a major cause of the broadening observed in the data presented. These sources are reviewed here as a means of documenting why these sources are no longer under consideration.

7.2.1 Inadequate Number of Available Data Points

The FTIR spectral resolution was investigated to determine if the FTIR measurement contained enough data points to adequately resolve the peaks. Figure 7-2 shows data points represented by dots and a line representing the model results. As can be seen in the figure, there are several measured points that fall well below the modeled peak and should be able to provide a more accurate representation. This is particularly noticeable with the data point at the center of the peak which is only 2/3 of the total peak height.

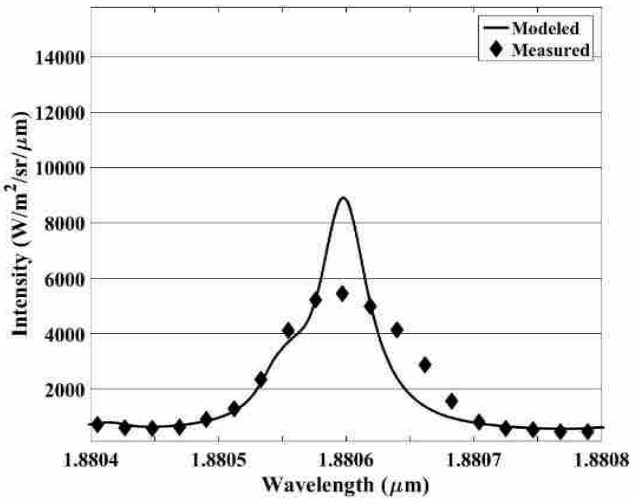

Figure 7-2: Point-by-point comparison of a horizontally-shifted measurement and model.

7.2.2 Apodization

One of the challenges with creating a Fourier transform of a measured signal occurs at the boundary of the interferogram or distance domain. The moving mirror can only traverse a finite path, for instance from an initial point $-L_{max}$ to a final point L_{max}. This can be understood as multiplying an infinite interferogram by one where data were collected ($-L_{max}$ to L_{max}), and by zero outside of that domain. Such a unit step function is shown in Figure 7-3, and because of its shape is known as a boxcar apodization function.

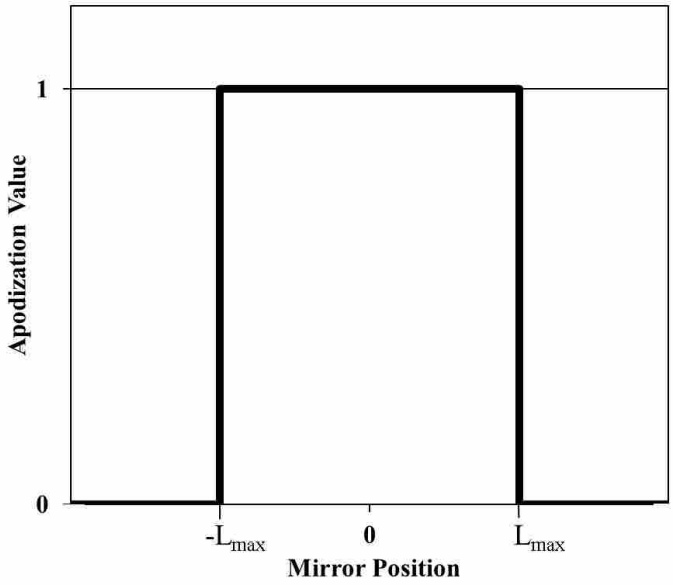

Figure 7-3: Boxcar apodization function.

The left and right boundaries of the unit step function shown in Figure 7-3 are a source of error. This is because a Fourier transform cannot closely follow a line with such steep transitions as seen in a unit step function. This will result in what appears to be a spectrum with more noise. To correct this issue, interferograms are multiplied by other apodization functions which do not have such severe transitions. One common apodization function is the Happ-Genzel function,

presented in Figure 7-4. The use of an apodization function can cause peak broadening, however. For this work, the Happ-Genzel was initially used. Figure 7-5 shows a comparison of spectra that were processed using each apodization function. The only difference that can be noted between the two spectra is that the boxcar led to slightly higher peaks than the Happ-Genzel. After this study, all interferograms used in this work were reprocessed using the boxcar function. However, the change did little to reduce the broadening of the measured data relative to the model.

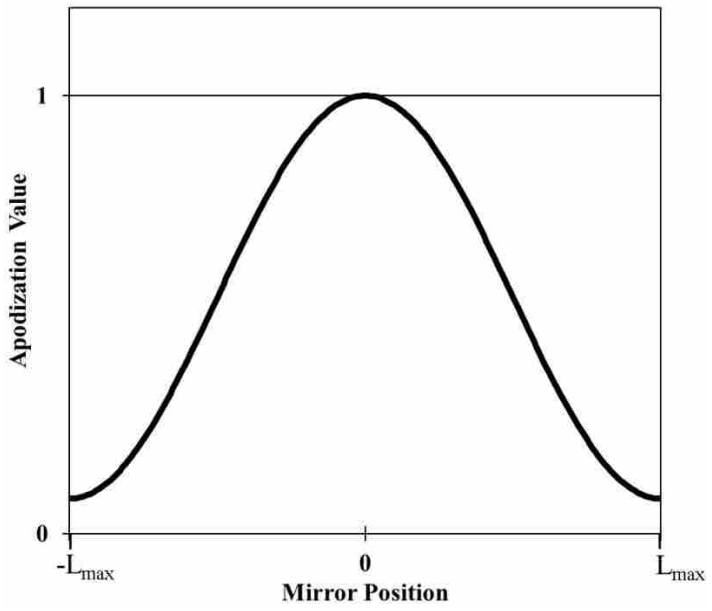

Figure 7-4: Happ-Genzel apodization function.

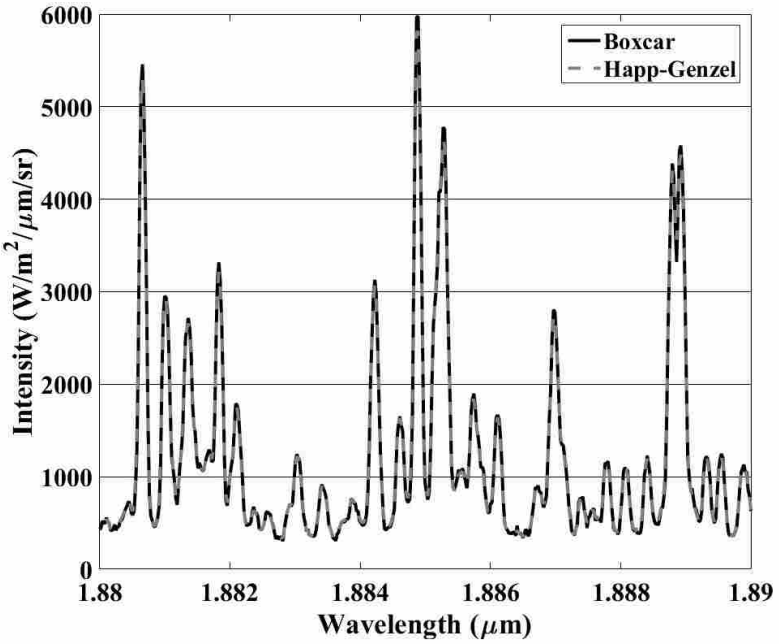

Figure 7-5: Comparison of data processed using the Boxcar and Happ-Genzel apodization functions.

7.2.3 Pressure Broadening

It is well established that increases in pressure cause spectral broadening by increasing collisional broadening, as discussed by Modest. [21]. Figure 7-6 shows a comparison of a measurement with three intensity models calculated at the measured gas temperature but with varying water vapor partial pressures. This increasing partial pressure could be caused by either an increase in total pressure or an increase in Y_{H2O}. Table 7-1 shows integrated values for bands A-E for each intensity spectrum. The intensity modeled for P_{H2O} of 0.14 atm is the expected partial pressure of the experimental data and produces narrow, high peaks, as discussed previously. The second partial pressure, P_{H2O} = 0.34 atm, was selected as a pressure that produced shorter peaks with approximately the same peak intensity magnitudes as measured experimentally. While this produced shorter peaks that were just lower than measured values in

magnitude, the baseline intensity between peaks was increased, producing a larger total area under the intensity curve, as seen in Table 7-1. It should also be noted that this partial pressure is well outside of the expected range of values, requiring an increase in either total pressure or Y_{H2O} of 2.4 times the expected values. With an even higher partial pressure of H_2O, (P_{H2O} = 0.68 atm) the peak values were reduced further but the integrated values were still increased due to higher intensities at off-peak locations. Increased collision broadening, induced in this case by increasing partial pressure, cannot adequately explain the difference in peak shape between the modeled and measured data.

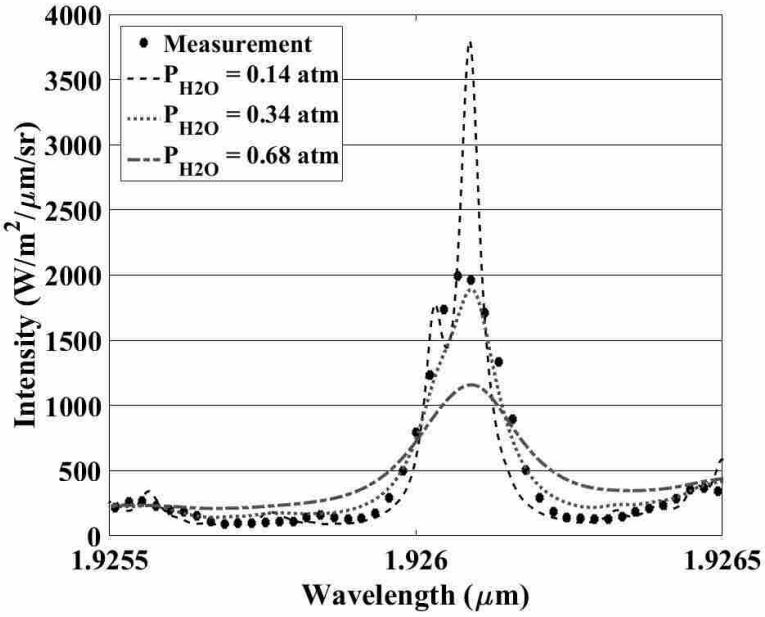

Figure 7-6: Comparison of a measurement and models calculated at the optically-measured gas temperature and varying partial pressures of water vapor.

Table 7-1: Intensity integrals for pressure broadening comparison.

	I_{A-E} (W/m^2/sr)
Measurement	105.8
P_{H2O} = 0.14 atm	109.9
P_{H2O} = 0.34 atm	113.6
P_{H2O} = 0.68 atm	115.2

7.2.4 Temperature and Concentration Fluctuations During Measurements

Gas temperature and concentration can be expected to fluctuate in a turbulent combustion environment such as the BFR used in this work. This fluctuation was a potential candidate for causing peak broadening, as the varying gas properties could cause a distribution of intensities that would appear as peak broadening. In order to investigate this the 1-D model described in Section 5.3 was used to determine the spectral intensity for 64 temperatures and 64 H_2O concentrations which were averaged to obtain a representative model intensity. The temperature and concentrations were selected using a normal distribution function and random number generator with results shown in Figure 7-7 and Figure 7-8.

The results of this investigation are shown in Figure 7-9 where there is virtually no difference between a spectrum with fixed properties and the average of many spectra with varying temperatures and concentrations.

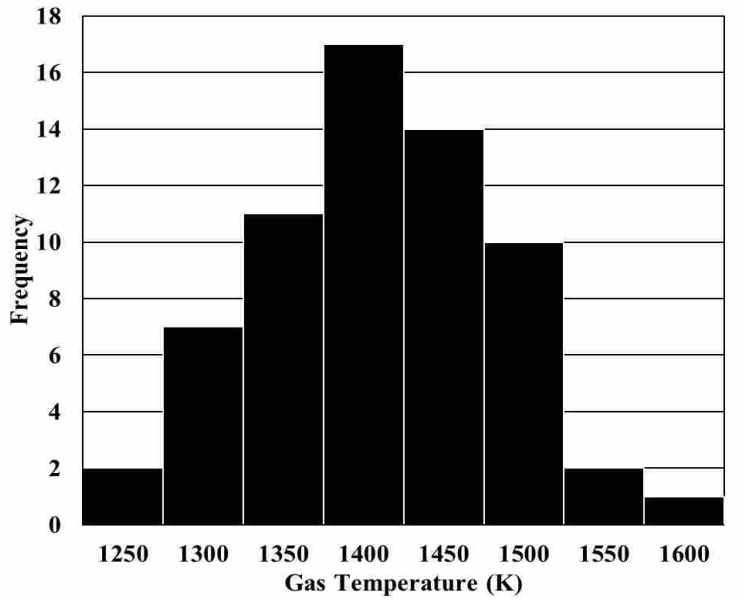

Figure 7-7: Histogram of gas temperatures used to investigate fluctuating conditions during a measurement.

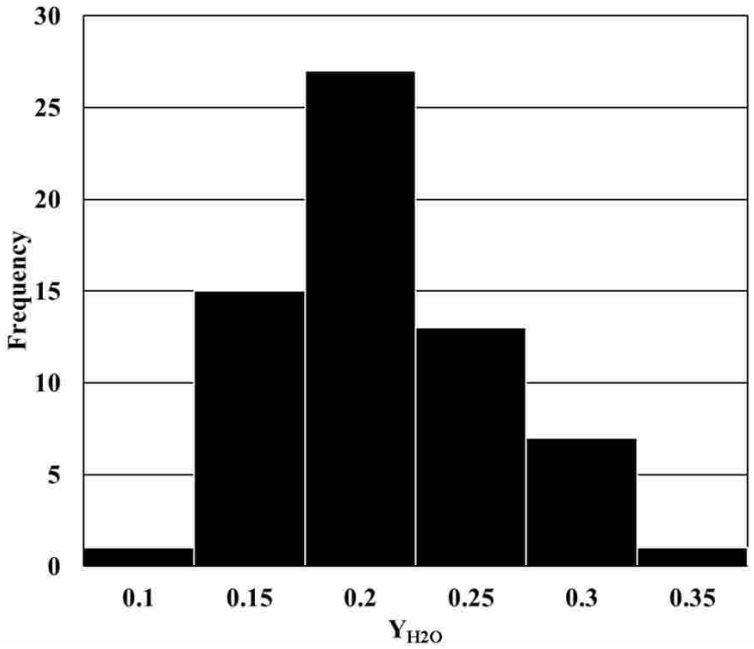

Figure 7-8: Histogram of H_2O concentrations used to investigate fluctuating conditions during a measurement.

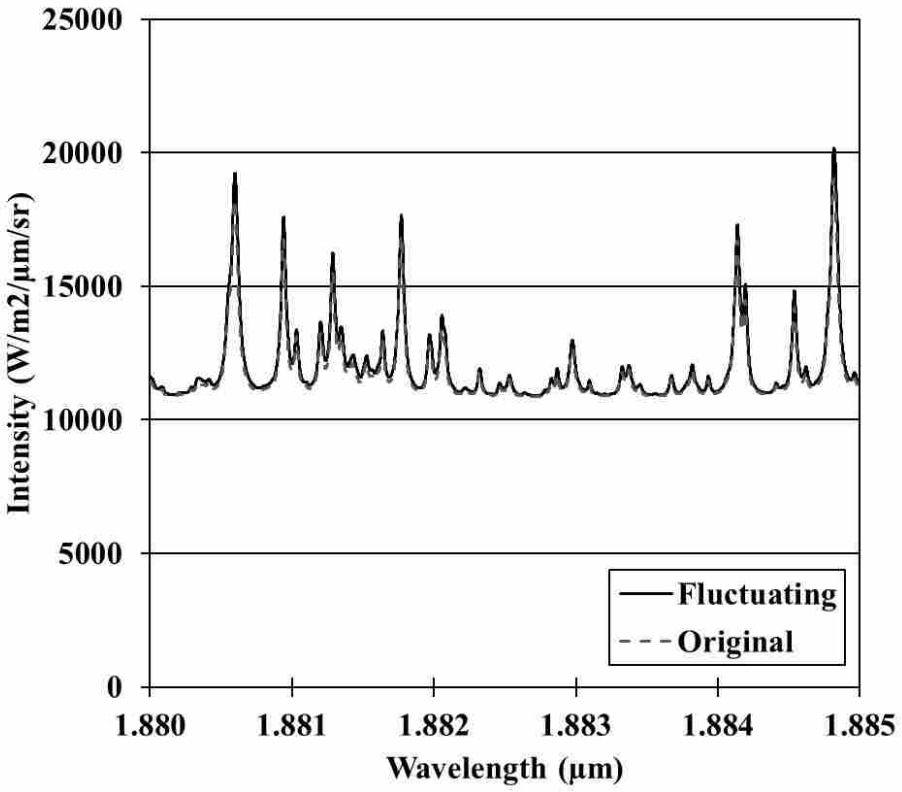

Figure 7-9: Comparison of modeled intensities for 1) a fixed T_g and Y_{H2O} and 2) averaged spectra with T_g and Y_{H2O} that fluctuated for each model.

7.2.5 FT of a Finite Interferogram

Performing a Fourier transform (FT) on a finite interferogram is known to cause peak broadening [23]. Griffiths and de Haseth [23] make a detailed presentation of this concept, which will be discussed here briefly.

As presented in Section 3.3, the basic theory used in obtaining a full spectrum from an FTIR measurement (interferogram) is that one may take the FT of an interferogram and obtain an intensity spectrum. However, in order for the FT to work without error, an infinite interferogram or an interferogram with bounds being from negative infinity to positive infinity is needed. This

would require the mirror to move an infinite length. As the FTIR is a finite instrument, the interferograms it collects are also finite, being the length of the maximum path difference. When one performs an FT on such a finite data set, it is as though the boxcar function (Section 7.2.2), were applied to an infinite data set. When an FT is performed on two functions that have been multiplied together, it gives the convolution of the FT of each function, as shown in Equation 7-2, where *I* and *B* are the interferogram and boxcar function. The FTIR therefore does not produce the true FT of an infinite function but rather the convolution of the FT of the true function and the FT of the boxcar function.

$$FT(I\ B) = FT(I) * FT(B) \tag{7-2}$$

The FT of a boxcar function is of the form *sin x / x*. It's convolution with a monochromatic source is displayed in Equation 7-3 [23]. This simple solution would fully describe a monochromatic source and an interferogram taken between +/- L_{max}. Figure 7-10 shows a typical depiction of this function, centered about 5450 cm^{-1}.

$$FT(B) = 2L_{max}\frac{\sin(2\pi(\nu - \nu_0)L_{max})}{2\pi(\nu - \nu_0)L_{max}} \tag{7-3}$$

In Equation 7-3, ν is the wavenumber, ν_0 is the reference wavenumber that the function is centered about, or the monochromatic source in this example, and L_{max} is the maximum path difference between the light paths involving the moving and stationary mirrors. The first zero crossing of Equation 7-3 is at $\pm\frac{1}{2L_{max}}$. Thus, with increasing L_{max} or travel of the moving mirror, the broadening is reduced. It can be imagined that when convolving a full spectrum with the FT of the boxcar function, the spectrum would undergo peak broadening, and this broadening would also decrease with increasing the length of travel of the moving mirror.

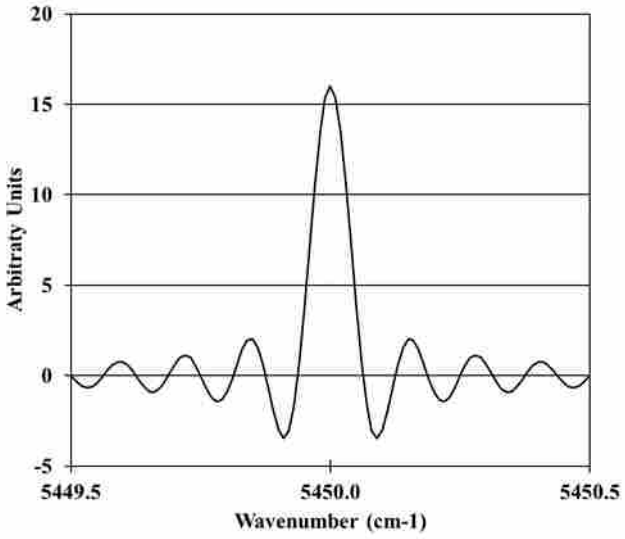

Figure 7-10: Example FT of a boxcar function centered about a given wavenumber.

In order to investigate this phenomenon as it applies to the data collected in this work, measurements were taken with the FTIR in front of a blackbody, as was done for calibration purposes and was described in Section 4.2. These measurements were collected at varying maximum path length differences. A typical absorption trough was compared between three data collections using the same FTIR as in the rest of this work. Each data set used a different L_{max} (8 cm, 4 cm, and 1 cm). This comparison is presented in Figure 7-11. As can be seen in the figure, there is little to no increase in peak broadening between an L_{max} of 8 cm and 4 cm. The expected effects are apparent at an L_{max} of 1 cm. This suggests that although this is a viable method of peak broadening, using an L_{max} of 8 cm should contain very little peak broadening of this sort. This is what was done in this work, as it also led to the highest resolution.

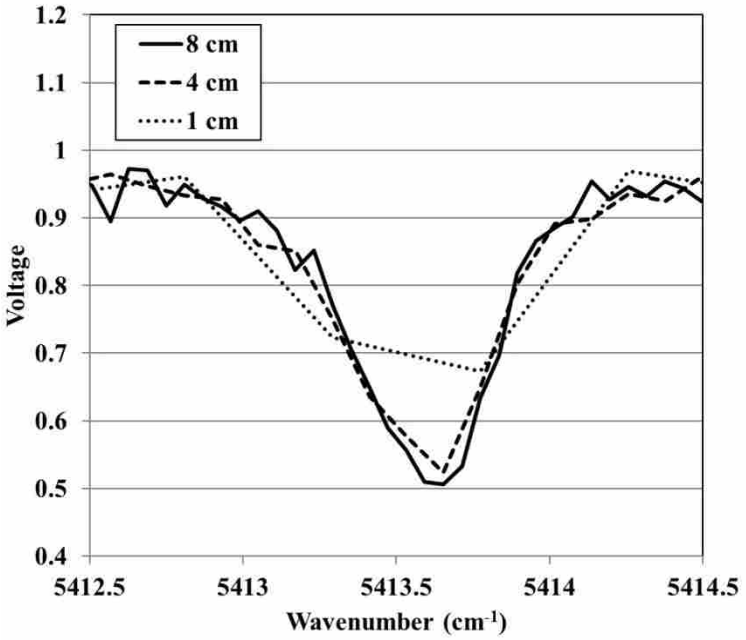

Figure 7-11: Comparison of FTIR spectra collected using decreasing values of L_{max}.

7.3 Likely Sources of Peak Broadening

Two sources of potential peak broadening were found to be likely sources of the broadening seen in this work. These sources are: 1) optical fiber chromatic dispersion; and 2) optical path dispersion. While it is highly probable that one or a combination of these mechanisms of peak broadening were responsible for the broadening, the equipment needed to test this hypothesis is no longer available.

7.3.1 Optical Fiber Chromatic Dispersion

Optical fibers are known to change the nature of the light being transmitted. According to Kartalopoulos [29], a fiber optic cable will spectrally "spread" light transmitted through it. This is known as chromatic dispersion, and is due to the difference between the index of refraction of

the cable core material, silica, and that of a true vacuum. The difference is augmented due to the changing index of refraction at different wavelengths. It is known that a nearly monochromatic light source can be broadened to the point of producing a full spectrum of light by passing it through a fiber optic, but this requires that the fiber optic cable be carefully designed to do so as in the work of Ranka et al. [30]. A very long fiber optic cable can also cause broadening [31]. Tateda et al. [31] demonstrated that it is possible to measure chromatic dispersion in a one meter long single mode fiber optic cable by using a Michelson interferometer. A similar comparison for a multi-mode fiber would be desirable for this work. The broadening seen in this work's measurements is on a very small spectral scale, indicating that perhaps this is a good explanation of the broadening and shortening of the peaks. This could potentially be verified by comparing measurements using fiber optic cables of varying lengths, but neither the fibers nor a spectral intensity source was available.

7.3.2 Optical Path Variation

Electromagnetic waves that are not perfectly collimated may lead to broadening due to photons of equal wavelength light travelling different path lengths through the interferometer. Photons exit a fiber in a cone shape traveling non-parallel trajectories. In this work, the exit cone passed through a collimator which improves collimation but is not perfect. The photons are then traveling dispersive paths. Figure 7-12 shows an example of two photons traveling through a Michelson interferometer, where the dashed and solid lines represent non-parallel paths. This is problematic, as the FTIR will produce interfering intensities for the same wavelengths at different mirror positions, which will be interpreted as different wavelengths. For example, one might consider an interferometer with a nominal path length of 4 cm between the beam splitter and a mirror and then the same 4 cm back to the beam splitter. Thus, the nominal path length for

this section of the interferometer would be 8 cm. A ray that is offset from the nominal path length by 0.5° upon entering the FTIR would travel a total path length of 8.003 cm along this path. For a spectrum of wavelengths a multitude of non-parallel rays would come from a non-collimated beam; this will translate to a general broadening of peaks.

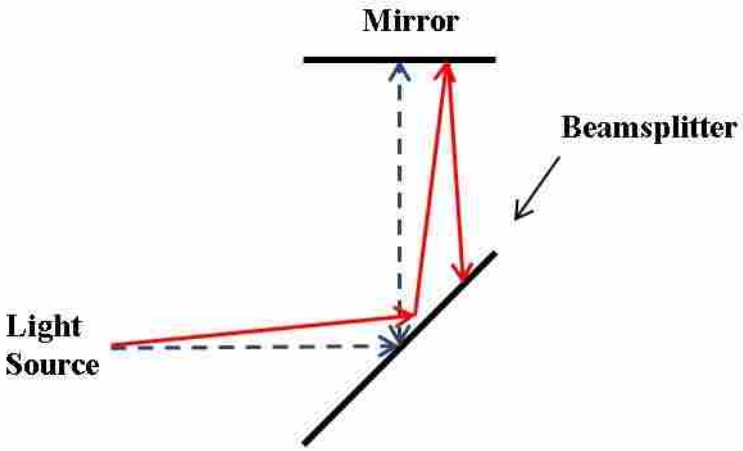

Figure 7-12: Example of un-collimated light source travelling different path lengths in a section of an FTIR's Michelson interferotmeter.

One method commonly used to reduce this peak broadening is to introduce an aperture at the focal point of the path through the FTIR. An aperture blocks dispersed rays and only allows parallel rays to the detector. An initial attempt was made to investigate this, but the results of this attempt were inconclusive. However, reduced peak broadening with the introduction of an aperture has been demonstrated by Thermo Fisher Scientific [32], the manufacturer of the FTIR used in this work. Their work demonstrated that an aperture can significantly reduce the peak breadth and increase the peak height. How close the peaks they measured were to true intensity is unclear.

Spectral emission from high temperature water vapor was not available at the time of aperture testing so spectral absorption of a 1373 K black body emission by atmospheric water vapor was used to evaluate the impact of an aperture on the width of absorption lines. This was done using the setup described for FTIR calibration in Section 4.2, but a 1.02 mm aperture was introduced into the light path at the FTIR's focal point located in the sample compartment. A temperature of 300 K was used for the H_2O temperature and weather station data were used to estimate humidity and water vapor concentrations.

A single absorption line for H_2O is shown with and without an aperture. It was necessary to look at the data at this level to investigate the minimal differences between peaks. The data show that the aperture attenuated the total intensity of the light but did not make the absorption line narrower or sharper. This would seem to indicate that the aperture neither reduced nor increased broadening appreciably. However, it is perhaps more important to note that the measured absorption data did not show any appreciable peak broadening even without an aperture. This result brings into question the hypotheses that the broadening is caused by fiber dispersion or optical dispersion. Unless some difference between the optics or interferogram processing can be found that applies to emission and not absorption, this result suggests that the emission is actually broadened compared to single temperature and concentration intensities. It remains unknown why peak broadening is observed in the emission measurements.

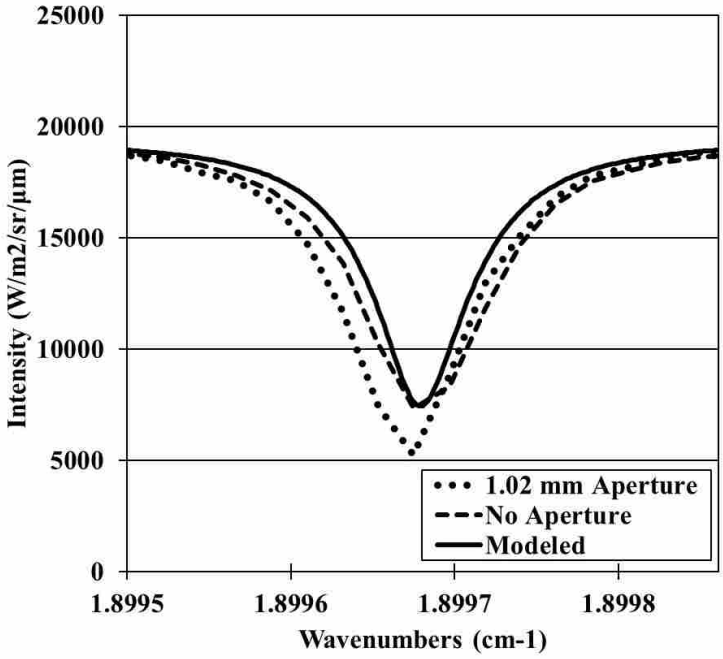

Figure 7-13: Comparison of the model to measurements taken with and without an aperture in front of the detector.

7.4 Resolving Differences Between Modeled and Measured Data

The shifted, broadened, and shortened measured peaks can be approximated in modeled data by applying a constant horizontal shift in the wavenumber domain, which was discussed in Section 7.1, and then performing a convolution, or moving weighted average in this case, on the modeled data.

The definition of the convolution of two functions, $f(x)$ and $g(x)$, is presented in Equation 7-4 [33].

$$f(x) * g(x) = \int_{-\infty}^{\infty} f(x)g(x-\tau)d\tau \tag{7-4}$$

The modeled spectral intensity function *g(x)* was convolved by a portion of Gaussian function *f(x)* represented by Equation 7-5. The resulting convoluted model intensity $g(\eta)_{conv}$ is given by

Equation 7-6. The denominator in Equation 7-5 is recognized as equal to the area of plus and minus one standard deviation of the Gaussian function which is 0.6827.

$$f(\eta) = \frac{\frac{1}{\sigma\sqrt{2\pi}}\exp\left(-\frac{(\eta-\mu)^2}{2\sigma^2}\right)}{\int_{-\sigma}^{+\sigma}\frac{1}{\sigma\sqrt{2\pi}}\exp\left(-\frac{(\eta-\mu)^2}{2\sigma^2}\right)} = \frac{\frac{1}{\sigma\sqrt{2\pi}}\exp\left(-\frac{(\eta-\mu)^2}{2\sigma^2}\right)}{0.6827} \tag{7-5}$$

$$g(\eta)_{conv} = \int_{-\infty}^{\infty} g(\eta) f(\eta - x) dx \tag{7-6}$$

The convolution was done by numerical integration. To do so, the integral is converted to a sum as show in Equation 7-7.

$$g(j)_{conv} = \sum_{i=-\infty}^{i=+\infty} g(j)\, f(j-i)\Delta x \tag{7-7}$$

The Gaussian function was defined with μ = 0, and it was decided to integrate between plus and minus one standard deviation resulting in Equation 7-8, where $\Delta\eta$ is the spacing between data points and N/2 is the number of points that represents one standard deviation. The number of points representing one standard deviation was varied until a visual best fit with the data was found to be 70 data points. This suggests the standard deviation of the Gaussian function that most correctly broadens the data is N/2 or 35 times the data spacing of 0.005 cm^{-1} or 0.175 cm^{-1}. The final width at half maximum for large emission peaks is on the order of 0.5 cm^{-1}.

$$g(j)_{conv} = \sum_{i=-N/2}^{i=N/2} 1.465 * g(j) \frac{1}{(N/2)\sqrt{2\pi}} \exp\left(-\frac{(i)^2}{N^2/2}\right)\Delta\eta \tag{7-8}$$

Figure 7-14 presents a comparison between an optical measurement, a corresponding spectral intensity model, and that same model after applying a horizontal shift and the convolution, i.e. the averaged model. The shifted, averaged model and the measurement are in good visual agreement with each other. Table 7-2 presents several comparisons of modeled intensity band integrals to the same integrals after the broadening has been applied. The data used for these measurements are the same that were previously investigated in Section 6.1.5 where it was established that the modeled and measured intensity band integrals showed good agreement. Here it can be seen that there is excellent agreement between band integrals of modeled and broadened modeled intensities, being less than 0.6% difference between the intensity integrals. This is expected because the convolution was normallized by the area of the convolution function. The convolved model intensity therfore contains the same integrated intensity as the original model and thereby represents the total radiative intensity accurately.

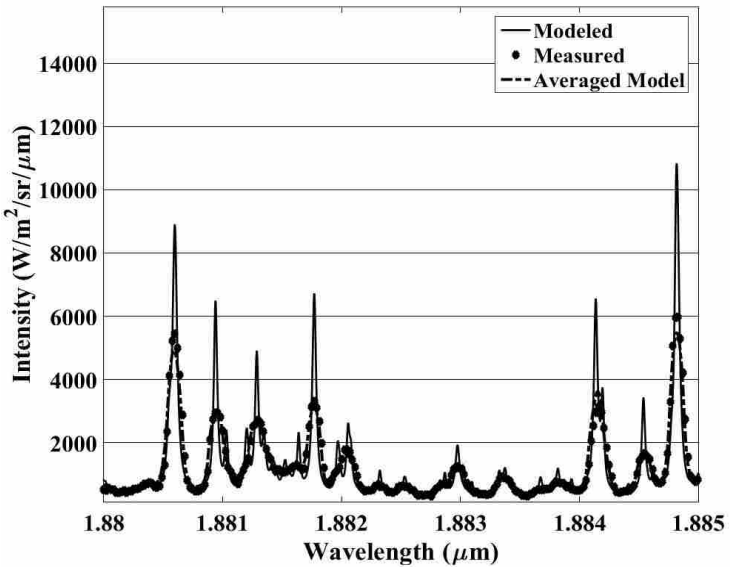

Figure 7-14: Comparison of a modeled intensity spectrum, before and after applying a weighted moving average, with a corresponding optical measurement.

Table 7-2: Selected comparisons of modeled and broadened intensity band integrals based on PFNG measurements.

	Band			
Path Length (m)	**A**	**B**	**C**	**E**
0.58	-0.4%	-0.1%	0.1%	0.0%
0.38	-0.5%	-0.1%	0.2%	0.1%
0.33	-0.5%	-0.2%	0.2%	0.1%
0.28	-0.5%	-0.2%	0.2%	0.1%
0.23	-0.6%	-0.2%	0.2%	0.1%
0.18	-0.6%	-0.2%	0.2%	0.1%
0.13	-0.6%	-0.2%	0.2%	0.1%
0.08	-0.6%	-0.2%	0.2%	0.1%
0.03	-0.6%	-0.3%	0.3%	0.1%

8 SUMMARY AND CONCLUSIONS

In summary, this work explored a method for determining the temperature, concentration, and spectral intensity of H_2O in combustion products with and without particles, extending the work previously performed by Ellis, et al [1]. Measurement methods were improved by introducing a cold target in the form of a cold cavity. An improved algorithm was determined and explored for removing background emission from single-media measurements. Five environments were studied with varying degrees of difficulty related to isolating the H_2O gas phase contribution to intensity. These included intensities measured along a line of sight for: Post-Flame Natural Gas (PFNG), Post-Flame Medium Wood (PFMW), Post-Flame Fine Wood (PFFW), In-Flame Natural Gas (IFNG), and In-Flame Fine Wood (IFFW). In order to extract only the water vapor intensity from measurements containing various combinations of background emission and participating media, the measured data were modeled by one of two simplifications to the radiative transfer equation that enabled an estimate from the measured data. For each condition, the impact of path length on measurement accuracy was investigated. A one-dimensional numerical spectral intensity model was also produced that allowed for specular reflection in order to compare modeled and measured intensity.

Data collection was limited to a four-month period between January and April 2016 with all data analysis to follow due to reactor availability. This limited experimental apparatus primarily to existing equipment and facilities with little time for modification.

The conclusions of this work are outlined in the rest of this chapter. The main categories of the conclusions have been listed as sections of the chapter.

8.1 Gas Temperature and Path length

For four of the five environments, the optical gas temperature was very accurate when path lengths were longer than 0.3 m. With more than 15 total measurements in four different environments (PFNG, PFMW, PFFW, and IFNG), all optical gas temperatures were within 2.4 % of the suction pyrometer temperatures. The error for IFNG for path lengths greater than 0.3 m was less than 1%. The exception to this observation was for IFFW, which produced optical gas temperatures between 5.4 and 11.4% above the suction pyrometer temperature. This environment also produced broadband temperatures suspected to come from particles that were higher than the suction pyrometer temperatures.

When path length decreased, the error in optical gas temperature increased. For measurements between 0.15 and 0.30 m, the mean error for all environments was -2.3%, and the standard deviation was 5.0%. from -7.3 to +4.6 %. Most of the optical temperatures were lower than the suction pyrometer temperatures. When path length decreased below 0.10 m, the temperature was very unreliable, having a mean of -4.4% but a standard deviation of 10%.

It can be concluded that in cases where 1) the cold target is aligned with the probe viewing angle, 2) the broadband intensity is less than the peaks in the gas intensity, and 3) the path length is above 0.3 m, the optical gas temperature will be measured correctly. This is true for both environments containing particles and soot.

8.2 Optically Measured Concentrations

The accuracy of optically measured concentrations was more difficult to evaluate because of the lack of measured H_2O data from which to compare. The accurate measure of H_2O concentration requires first an accurate measure of temperature. Therefore, the values of H_2O concentration at 0.3 m and longer path length are of greatest value in assessing this method.

- The optical concentrations for PFNG, IFNG, and PFMW were reasonable for longer path lengths with relative differences between optically measured concentration and reference values being -11.5 to 10% for PFNG, -20 to -6.1% for IFNG, and -1.7 to 14.2 % for PFMW.
- For IFFW and PFFW the optical concentrations were typically considerably higher than the reference value. IFFW optical concentrations ranged from 48 to -15% different and PFFW ranged from 26-85% higher than the reference value. The fact that in both cases the reference values are lower than the optical measurements suggests some error might exist in the determination of the reference value. Nevertheless, the spread of error is still large indicating inaccuracy of the method.

It can be concluded that the optical concentration method is less accurate than the temperature method. Assuming an error in the reference H_2O value for fine wood, the optical concentration measurement method is at best accurate to within 20%. The inaccuracy of the concentration method was likely due to the fact that it relied on magnitude-based measurements, and inaccuracy of the assumption that fuel particles do not scatter. Fuel particles are suspected to have caused back-scattering of gas intensity into the probe line of sight, causing higher magnitudes that appeared as higher concentrations of H_2O.

8.3 Spectral Intensity

A comparison of the measured intensity and a 1-D modeled spectral intensity using the measured temperature and concentration as inputs produced the following results.

- Every spectral peak in the model had a corresponding peak in the measured data.
- There was a noticeable, apparently consistent shift of approximately 0.167 cm-1, between the peaks in the model and the peaks in the measurement. It was concluded that this shift was the result of the uncertainty in the reference laser wavelength used by the manufacturer. A horizontal shift enabled the peaks to match but had no impact on temperature and concentration calculations.
- Measured peaks were shorter and broader than modeled peaks. Although numerous possible reasons were investigated, no definitive conclusion was drawn as to the cause.
- Differences in intensity peak shape between measurements and the model used could be approximated with a convolution based on a normal distribution.
- The spectral intensity integrated over the bands of interest in this work matched well between modeled and measured data, being within 3% for all but the least accurate measurements.

8.4 Particle Emissivity

An effective emissivity over the measured path length was calculated for particle-laden flows. For a path length of 0.55 m, the effective emissivity of the combine wood, char and soot was 0.17 – 0.18 and for IFNG containing soot, the emissivity was 0.023. This indicates that for

these particular flames at the location measured, fuel and char particles are for greater emitters and contribute more to radiative heat transfer than soot.

REFERENCES

[1] D. J. Ellis, V. P. Solovjov and D. R. Tree, "Temperature Measurements Using Infrared Spectral Band Emissions from H2O," *Journal of Energy Resources Technology,* 2015.

[2] A. D. Eisner and D. E. Rosner, "Experimental studies of soot particle thermophoresis in nonisothermal combustion gases using thermocouple response techniques," *Combustion and Flame,* vol. 61, no. 2, pp. 153-166, 1985.

[3] A. Ballantyne and J. B. Moss, "Fine wire thermocouple measurements of fluctuating temperature," *Combustion Science and Technology,* vol. 17, no. 1-2, pp. 63-72, 1977.

[4] J. S. Newman and P. A. Croce, "A simple aspirated thermocouple for use in fires," *Journal of Fire and Flammability,* vol. 10, pp. 326-336, 1979.

[5] A. Z'Graggen, H. Friess and A. Steinfeld, "Gas temperature measurement in themal radiating environments using a suction thermocouple apparatus," *Measurement Science and Technology,* vol. 18, pp. 3329-3334, 2007.

[6] S. Brohez, C. Delvosalle and G. Marlair, "A two-thermocouples probe for radiation correction of measured temperatures in compartment fires," *Fire Safety Journal,* vol. 39, pp. 399-411, 2004.

[7] S. Krishnan, B. M. Kumfer, W. Wu, J. Li, A. Nehorai and R. Axelbaum, "An approach to thermocouple measurements that reduces uncertainties in high-temperature environments," *Energy & Fuels,* vol. 29, pp. 3446-3455, 2015.

[8] H. Zhao and N. Ladommatos, "Optical diagnostics for soot and temperature measurement in diesel engines," *Progress Energy Combustion Science,* vol. 24, pp. 221-255, 1998.

[9] T. Draper, D. Zeltner, D. Tree, Y. Xue and R. Tsiava, "Two-dimensional flame temperature and emissivity measurements of pulverized oxy-coal flames," *Journal of Applied Energy,* vol. 95, pp. 38-44, 2012.

[10] R. L. Farrow, P. L. Mattern and L. A. Rahn, "Comparison between CARS and corrected thermocouple temperature measurements in a diffusion flame," *Applied Optics,* vol. 21, no. 17, pp. 3119-3125, 1982.

[11] M. G. Allen and W. J. Kessler, "Simultaneous water vapor concentration and temperature measurements using 1.31-micron diode lasers," *AIAA Journal,* vol. 34, no. 3, pp. 483-488, 1996.

[12] X. Zhou, L. Xiang, J. B. Jeffries and R. K. Hanson, "Development of a sensor for temperature and water concentration in combustion gases using a single tunable diode laser," *Measurement Science and Technology,* vol. 14, pp. 1459-1468, 2003.

[13] R. J. Anderson and P. R. Griffiths, "Determination of rotational temperatures of diatomic molecules from absorption spectra measured at moderate resolution," *Quantitative Spectroscopic Radiative Transfer,* vol. 17, pp. 393-401, 1977.

[14] L. A. Gross and P. R. Griffiths, "Temperature estimation of carbon dioxide by infrared absorption spectrometry at medium resolution," *Journal of Quantitative Spectroscopy and Radiative Transfer,* vol. 39, no. 2, pp. 131-138, 1988.

[15] P. R. Solomon, P. E. Best, R. M. Carangelo, J. R. Markham, P. Chien, R. J. Santoro and H. G. Semerjian, "FT-IR emission/transmission spectroscopy for in-situ combustion diagnostics," *21st Symposium on Combustion, The Combustion Institute,* pp. 1763-1771, 1986.

[16] D. Bäckström, R. Johansson, K. Andersson, F. Johnsson, S. Clausen and A. Fateev, "Gas temperature and radiative heat transferin oxy-fuel flames," in *37th International Technical Conference on Clean Coal & Fuel Systems*, Clearwater, 2012.

[17] T. M. M. F. F. A. C. S. Ren, "An inverse radiation model for optical determination of temperature and species concentration: Development and validation," *Journal of Quantitative Spectroscopy & Radiative Transfer,* vol. 151, pp. 198-209, 2015.

[18] J. T. Pearson, B. W. Webb, V. P. Solovjov and J. Ma, "Efficient representation of the absorption line blackbody distribution function for H2O, CO2, and CO at variable temperature, mole fraction, and total pressure," *Journal of Quantitative Spectroscopy & Radiative Transfer,* vol. 138, pp. 82-96, 2014.

[19] K. Andersson, R. Johansson and F. Johnsson, "Thermal radiation in oxy-fuel flames," *International Journal of Greenhouse Gas Control,* vol. 5, pp. S58-S65, 2011.

[20] L. C. Speitel, "Fourier Transform Infrared analysis of combustion gases," *Journal of Fire Sciences,* vol. 20, pp. 349-371, 2002.

[21] M. F. Modest, Radiative Heat Transfer, 3rd ed., New York: Academic Press, 2013.

[22] L. Mertz, Transformations in Optics, New York: John Wiley & Sons, Inc., 1965.

[23] P. R. Griffiths and J. A. de Haseth, Fourier Transform Infrared Spectrometry, Hoboken, New Jersey: John Wiley & Sons, Inc., 2007.

[24] V. Gopal, S. K. Singh and R. M. Mehra, "Analysis of dark current contributions in mercury cadmium telluride junction diodes," *Infrared Physics & Technology,* vol. 43, pp. 317-326, 2002.

[25] W. Hu, X. Chen, Z. Ye, J. Zhang, F. Yin, C. Lin, Z. Li and W. Lu, "Accurate simulation of temperature-dependent dark current in HgCdTe infrared detectors assisted by analytical modeling," *Journal of Electronic Materials,* vol. 39, no. 7, pp. 981-985, 2010.

[26] S. S. Andrews and S. G. Boxer, "Analysis of noise for rapid-scan and step-scan methods of FT-IR difference spectroscopy," *Applied Spectroscopy,* vol. 55, no. 9, pp. 1161-1165, 2001.

[27] Thermo Fisher Scientific Inc., Users Guide for the Nicolet 8700, Madison: Thermo Fisher Scientific Inc, 2007.

[28] R. S. Figliola and D. E. Beasley, Theory and Design for Mechanical Measurements, John Wiley & Sons, Inc, 2006.

[29] S. V. Kartalopoulos, Introduction to DWDM technology: Data in a rainbow, Bellingham, Washington: SPIE Press, 1999.

[30] J. K. Ranka, R. S. Windeler and A. J. Stentz, "Visible continuum generation in air-silica microstructure optical fibers with anomalous dispersion at 800 nm.," *Optics Letters,* vol. 25, no. 1, pp. 25-27, 2000.

[31] M. Tateda, N. Shibata and S. Seikai, "Interferometric method for chromatic dispersion measurement in a single-mode optical fiber," *IEEE Journal of Quantum Electronics,* Vols. QE-17, no. 3, pp. 404-407, 1981.

[32] Thermo Scientific, "Technical Note 52535: A Tutorial on Spectral Resolution for the Nicolet iS5 FT-IR Spectrometer," Thermo Fisher Scientific, 2013.

[33] R. N. Bracewell, The Fourier Transform and Its Applications, New York: McGraw-Hill Book Company, 1978.

[34] J. Roberts, Interviewee, [Interview]. 2016.

[35] I. H. Malitson, "Interspecimen Comparison of the Refractive Index of Fused Silica," *Journal of the Optical Society of America,* vol. 55, no. 10, pp. 1205-1209, 1965.

[36] T. R. R. L. W. Hunter, "Scrambling Properties of Optical Fibers and the Performance of a Double Scrambler," *Publications of the Astronomical Society of the Pacific,* vol. 104, pp. 1244-1251, 1992.

[37] R. S. B. T. B. Bretzlaff, "Apodization effects in Fourier transform infrared difference spectra," *Revue de Physique Appliquee,* vol. 21, no. 12, pp. 833-844, 1986.

[38] B. Fornberg and J. Zuev, "The Runge phenomenon and spatially variable shape parameters in RBF interpolation," *Computers & Mathematics with Applications,* vol. 54, no. 3, pp. 379-398, 2007.

[39] Y. Tan, E. Croiset, M. A. Douglas and K. V. Thambimuthu, "Combustion characteristics of coal in a mixture of oxygen and recycled flue gas," *Fuel,* vol. 85, no. 4, pp. 507-512, 2006.

[40] M. G. Allen and W. J. Kessler, "Somultaneous water vapor concentration and temperature measurements using 1.31-micron diode lasers," *AIAA Journal,* vol. 34, no. 3, pp. 483-488, 1996.

[41] W. Navidi, Statistics for Engineers and Scientists, New York: McGraw-Hill, 2006.

[42] R. S. Bretzlaff and T. B. Bahder, "Apodization effects in Fourier transform infrared difference spectra," *Revue de Physique Appliquee,* vol. 21, no. 12, pp. 833-844, 1986.

APPENDIX A. SIMPLIFICATION OF RTE FOR TEMPERATURE DETERMINATION IN PARTICLE-LADEN FLOWS

In Section 5.2, a simplification is made to the radiative transfer equations to enable the determination of gas temperature from measured spectral data containing both gas and particle emission. The simplification is based on the assumption that total absorption of radiation by the participating media was small. In order to understand why the simplification allows reasonable temperature results to be obtained and to understand the limitations of the approach, a numerical parametric study was performed to evaluate the errors of the assumption. The study involved producing simulated spectral signals using a line of sight spectral model of the complete radiative transfer equation. The simulated signal was then processed using the procedure outlined in Section 5.2 utilizing the simplified RTE. The temperature and intensity of the gas phase as calculated by the simplified method and integrated using trapezoidal integration were then compared to the model input temperature and the integrated intensity calculated from the model.

The numerical experiment included a variation of the input variables as shown in Table A-1 resulting in 70 independent conditions.

Figure A-1 shows the ratio of processed to actual or input gas temperature. The results show that when $\kappa_g \gg \kappa_p$, indicating weak particle participation, all three band ratios provided the correct gas temperature. However, when $\frac{\kappa_g}{\kappa_p} < 2.5$, the temperatures obtained from bands E/A were unreliable and in many instances were undefined (negative).

Table A-1: Properties used for numerical experiments.

	Values Used
T_{H2O} (K)	1200,1500, 1800
Y_{H2O}	0.05, 0.07, 0.15
$T_{part.}$ (K)	1200, 1700
κ_p	0.04, 0.1, 0.4, 1
L (m)	0.1, 0.5, 1

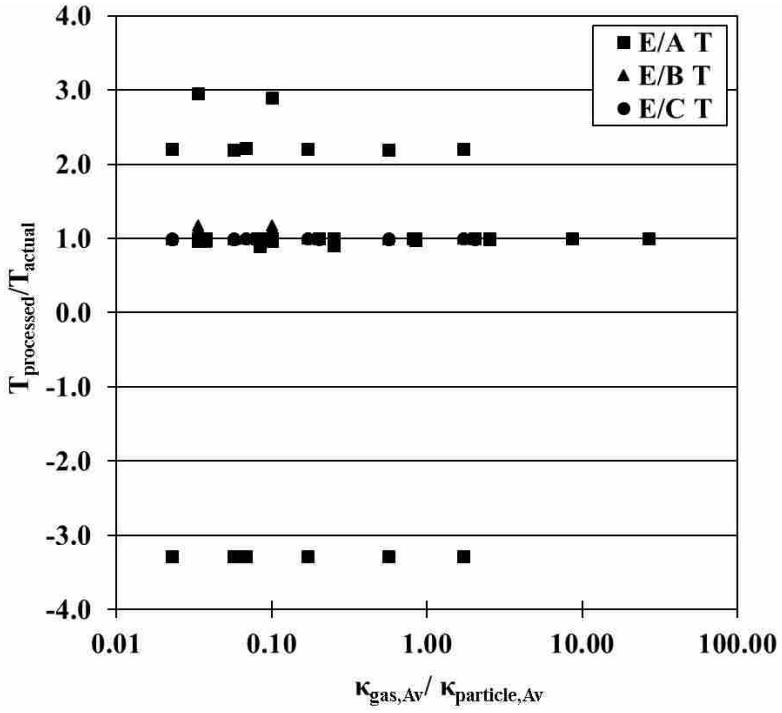

Figure A-1: $T_{gas,processed}/T_{gas,actual}$ plotted against $\kappa_{gas,Av}/\kappa_{particle,Av}$. Gas properties were averaged over bands A-E.

In order to more closely examine the results using the other band ratios, the temperatures calculated from the bands E/A were removed with results shown in Figure A-2. Now it becomes apparent that for all of the cases in the numerical experiment, the ratio of band E / C resulted in

gas temperatures that were very close to the actual gas temperature, specifically being within 6% of the actual gas temperature.

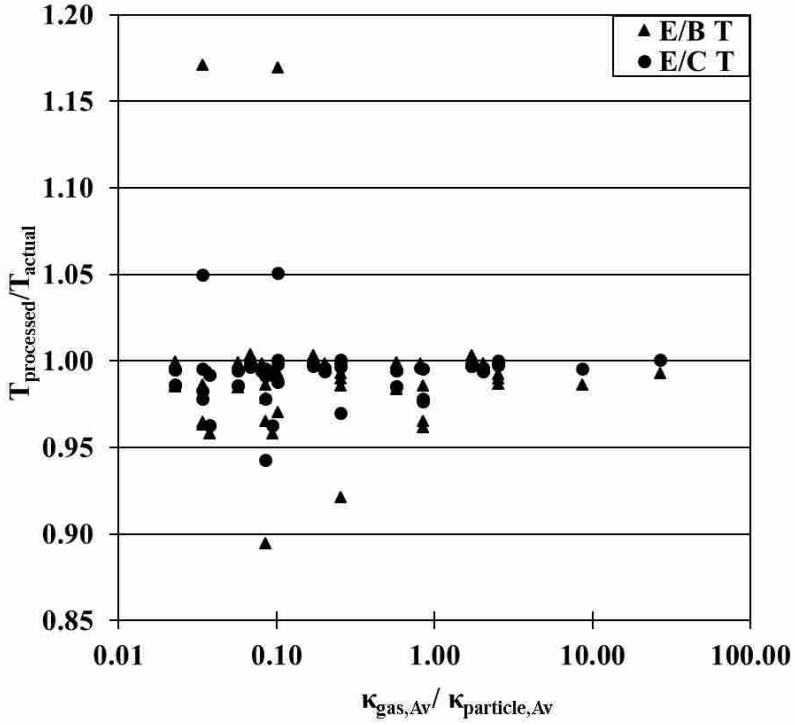

Figure A-2: Figure A-1 without E/A temperatures.

The reason for the more accurate results is shown in Figure A-3 where the intensity integrals for bands A, B, C, and E, obtained as outlined in Section 5.2, are divided by integrals of gas intensity for each band based on the input temperature, H_2O concentration, and pressure. For most of the cases, particularly those with large gas absorption relative to particle absorption, all four data points appear at the same location and are covered by the largest symbol, the square. There are however several data sets where the data are scattered. In these cases, the integrated areas of C and E are closest together. Because the temperature measurement technique utilizes the intensity ratio, an equal error on both bands cancels and the temperature is produced

accurately. Greater differences are seen between band E and bands A and B, which leads to higher differences in the temperature measurement calculations when using ratios with these bands. Accordingly, for this work the gas temperature from bands E and C was used when processing data from measurements where particles were in the line of sight of the measurement.

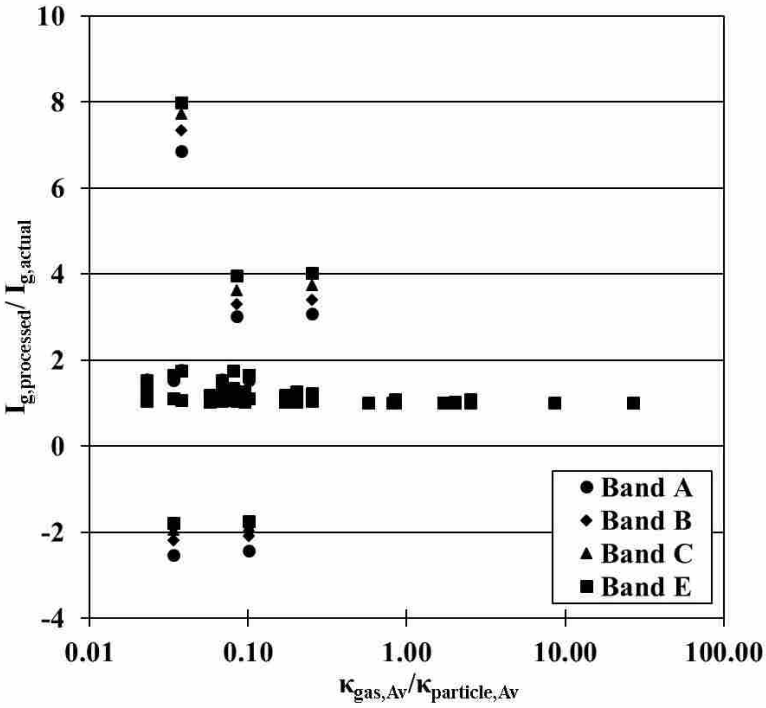

Figure A-3: Processed gas intensities integrated over bands A, B, C, and E divided by the actual gas intensity for each band. Comparisons are of intensities using the assumed processing method and actual gas-only spectra.

In summary, the implications to the RTE enables the resulting intensity to be used for particle laden gas concentrations as long as the ratio of $\frac{\kappa_g}{\kappa_p} > 2.5$ or the bands of C/E are used to calculate the integrated spectral intensities. The simplified RTE can be used for temperature

calculations only and cannot be used to find the H2O concentration, which depends on the total intensity and not on intensity ratios.